

Effect of polyelectrolyte backbone rigidity on bulk, surface and foam film properties

vorgelegt von
M. Sc.
Martin Uhlig
geboren in Berlin

von der Fakultät II - Mathematik und Naturwissenschaften
an der Technischen Universität Berlin
zur Erlangung des akademischen Grades

Doktor der Naturwissenschaften
(Dr. rer. nat.)

genehmigte Dissertation

Promotionsausschuss:

| | |
|-----------------|-------------------------------|
| Vorsitzender: | Prof. Dr. Reinhard Schomäcker |
| 1. Gutachterin: | Prof. Dr. Regine von Klitzing |
| 2. Gutachterin: | Dr. habil Cécile Monteux |

Tag der wissenschaftlichen Aussprache: 21.10.2016

Berlin 2016

Abstract

The polyelectrolyte backbone rigidity, quantified as the persistence length, is an important parameter governing the conformation of polyelectrolytes. The most thoroughly investigated *synthetic* polyelectrolytes as poly(styrene sulfonate) (PSS) are rather flexible. In contrast *natural* polyelectrolytes, as deoxyribonucleic acid (DNA) or xanthan, are rather rigid. Former comparisons of flexible and rigid polyelectrolytes were hampered by the fact that the available polyelectrolytes were very different, i.e. they did not only vary in backbone rigidity but also in chemical structure etc. By comparing the relatively novel rigid polyelectrolyte sulfonated poly(phenylene sulfone) (sPSO₂-220) and the chemically similar flexible polyelectrolyte PSS it is possible to narrow the varied polyelectrolytes parameters to the persistence length and the dissociation degree. The aim of this thesis is a better understanding of the influence of polyelectrolyte backbone rigidity on bulk, surface and foam film properties. The results might be generalized for rigid polyelectrolytes of importance in life science (e.g. DNA) or food technology (e.g. xanthan).

At first, mixtures of the rigid polyelectrolyte sPSO₂-220 and the oppositely charged surfactant tetradecyl trimethylammonium bromide (C₁₄TAB) were investigated with respect to their surface adsorption and foam film stability. sPSO₂-220/C₁₄TAB mixtures showed a much higher surface activity and foam film stability than PSS/C₁₄TAB mixtures.

Secondly, the surface composition and structure of the sPSO₂-220/C₁₄TAB mixtures were investigated and the results were correlated to the foam film stability. An extended framework to explain the foam film (de)stability was developed, which in addition to the repulsive interactions of surface charges, takes the structure of adsorbed polyelectrolyte/surfactant layer(s) into account.

Thirdly, the surface composition and foam film stability of PSS in mixtures with C₁₄TAB was investigated. In contrast to sPSO₂-220/C₁₄TAB mixtures, PSS/C₁₄TAB mixtures did not show increasing foam film stability with increasing polyelectrolyte concentration, which can be explained by preferred bulk complexation of this mixture.

In the second to last chapter, the focus turns from surface into bulk investigations. The influence of polyelectrolyte backbone rigidity on the structuring in aqueous solution with and without geometrical confinement was determined. In bulk and confinement the characteristic lengths were shorter for rigid sPSO₂-220 than for flexible PSS.

In the last part rigid rod-like nanoparticles were investigated instead of rigid polyelectrolytes. Different types of cellulose nanocrystals (CNC) were examined with respect to their size parameters and ordering. A lateral organization of the CNC into stable 2D aggregates and reversible liquid crystal like ordering was discovered.

Die Steifigkeit der Polyelektrolythauptkette (Persistenzlänge) ist ein wichtiger Parameter der für die Konformation des Polyelektrolyten entscheidend ist. Die am ausführlichsten untersuchten *synthetischen* Polyelektrolyte wie Polystyrolsulfonat (PSS) sind eher flexibel. *Natürliche* Polyelektrolyte wie Desoxyribonukleinsäure (DNA) oder Xanthan sind im Gegensatz dazu eher kettensteif. Frühere Vergleiche von flexiblen und steifen Polyelektrolyten wurden dadurch erschwert, dass die verfügbaren Polyelektrolyte sehr unterschiedlich waren, da sie sich nicht nur in der Steifigkeit sondern auch in chemischer Struktur usw. unterschieden. In dem man das neuartige steife Polyelektrolyt sulfoniertes Polyphenylsulfone (sPSO₂-220) mit dem chemisch sehr ähnlichen flexiblen Polyelektrolyt PSS vergleicht, ist es möglich die variierten Parameter auf Persistenzlänge und Dissoziationsgrad zu reduzieren. Das Ziel dieser Arbeit ist ein besseres Verständnis der Auswirkung der Steifigkeit der Polyelektrolythauptkette auf Polyelektrolyteigenschaften in der Volumenphase, an der Grenzfläche und in Schaumfilmen.

Zuerst wurden Mischungen des kettensteifen sPSO₂-220 mit dem entgegengesetzt geladenen Tensid Tetradecyltrimethylammoniumbromid (C₁₄TAB) in Hinblick auf die Adsorption an der Wasser/Luft Grenzfläche und Schaumfilmfestigkeit untersucht. sPSO₂-220/C₁₄TAB Mischungen zeigten dabei eine hohe Oberflächenaktivität und Schaumfilmfestigkeit.

Im folgenden Kapitel wurde die Oberflächenzusammensetzung und Struktur von sPSO₂-220/C₁₄TAB Mischungen untersucht. Die Ergebnisse wurden mit der Schaumfilmfestigkeit korreliert. Ein erweitertes Modell zur Erklärung der Schaumfilmfestigkeit wurde entwickelt, welches auch die Struktur der Polyelektrolyt/Tensid Schichten in Betracht zieht.

Im dritten Kapitel wurde die Oberflächenzusammensetzung und Schaumfilmfestigkeit von PSS/C₁₄TAB Mischungen untersucht. Im Gegensatz zu sPSO₂-220/C₁₄TAB Mischungen zeigten PSS/C₁₄TAB Mischungen keine höhere Schaumfestigkeit mit höherer Polyelektrolytkonzentration. Dies konnte mit der bevorzugten Aggregation in der Volumenphase erklärt werden.

Im vierten Kapitel wurde der Einfluss der Steifigkeit der Polyelektrolythauptkette auf die Strukturierung in wässriger Lösung ohne und mit räumlicher Beschränkung untersucht. Sowohl mit als auch ohne räumliche Beschränkung waren die charakteristischen Abstände kürzer für das kettensteife sPSO₂-220 als für das flexiblere PSS.

Im letzten Kapitel wurden nicht mehr steife Polyelektrolyte sondern steife Nanopartikel untersucht. Verschiedene Typen von Zellulosenanokristallen wurden in Hinblick auf Größe und Ordnungsverhalten untersucht. Eine laterale Ordnung in stabile 2D Aggregate und reversible Ordnung ähnlich der von Flüssigkristallen wurde gefunden.

Contents

| | |
|---|-----------|
| List of symbols and abbreviations | 3 |
| 1 Introduction | 7 |
| 2 Scientific background | 9 |
| 2.1 Adsorption at the air/water interface | 9 |
| 2.1.1 Adsorption from surfactant solutions | 9 |
| 2.1.2 Adsorption of oppositely charged polyelectrolyte/surfactant mixtures | 10 |
| 2.2 Foam films as building blocks of macroscopic foams | 12 |
| 2.2.1 Foam films formed by pure surfactant solutions | 13 |
| 2.2.2 Foam films formed by oppositely charged polyelectrolyte/surfactant mixtures | 13 |
| 2.2.3 Stratification in polyelectrolyte/surfactant foam films | 15 |
| 2.3 Cellulose nanocrystals | 16 |
| 3 Materials and sample preparation | 19 |
| 3.1 Surfactants | 19 |
| 3.2 Polyelectrolytes | 19 |
| 3.3 Cellulose nanocrystals | 22 |
| 4 Experimental techniques | 23 |
| 4.1 Characterization of surface adsorption | 23 |
| 4.2 Thin film pressure balance (TFPB) | 25 |
| 4.3 Neutron reflectometry (NR) | 29 |
| 4.4 Small angle neutron scattering (SANS) | 31 |
| 4.5 Additional experimental techniques | 32 |
| 5 Surface adsorption of sulfonated poly(phenylene sulfone)/C₁₄TAB mixtures and its correlation with foam film stability | 35 |
| 5.1 Introduction | 35 |
| 5.2 Results | 36 |
| 5.2.1 Determination of the intrinsic persistence length of sPSO ₂ -220 . . . | 36 |
| 5.2.2 Characterization of the air/water interface | 38 |
| 5.2.3 Properties of foam films - disjoining pressure isotherms | 41 |
| 5.3 Discussion | 44 |
| 5.3.1 Adsorption of sPSO ₂ -220/C ₁₄ TAB mixtures at the air/water interface | 44 |
| 5.3.2 Foam film properties of sPSO ₂ -220/C ₁₄ TAB mixtures | 48 |
| 5.4 Conclusion | 52 |

| | | |
|----------|--|-----------|
| 6 | Surface composition and the correlation to foam film stability of sPSO₂-220/C₁₄TAB mixtures | 53 |
| 6.1 | Introduction | 53 |
| 6.2 | Results | 55 |
| 6.2.1 | Bulk interaction of sPSO ₂ -220 and C ₁₄ TAB | 55 |
| 6.2.2 | Surface composition of sPSO ₂ -220/C ₁₄ TAB mixtures | 56 |
| 6.2.3 | Preliminary insight into the structure of sPSO ₂ -220/C ₁₄ TAB mixtures at the air/water interface | 58 |
| 6.3 | Discussion | 59 |
| 6.3.1 | Bulk interaction of sPSO ₂ -220 and C ₁₄ TAB | 59 |
| 6.3.2 | Surface composition of sPSO ₂ -220/C ₁₄ TAB mixtures | 59 |
| 6.3.3 | Preliminary insight into the structure of sPSO ₂ -220/C ₁₄ TAB mixtures at the air/water interface | 60 |
| 6.3.4 | Correlation of surface composition and foam film stability of sPSO ₂ -220/C ₁₄ TAB mixtures | 62 |
| 6.4 | Conclusion | 66 |
| 7 | Surface composition and foam film stability of PSS/C₁₄TAB mixtures | 67 |
| 7.1 | Introduction | 67 |
| 7.2 | Results | 68 |
| 7.2.1 | Bulk interaction of PSS and C ₁₄ TAB | 68 |
| 7.2.2 | Surface composition of PSS/C ₁₄ TAB mixtures | 70 |
| 7.2.3 | Foam film stability of PSS/C ₁₄ TAB mixtures | 72 |
| 7.3 | Discussion | 77 |
| 7.3.1 | Origins of the differences between former and current results for PSS/C ₁₄ TAB mixtures | 77 |
| 7.3.2 | Bulk interaction of PSS and C ₁₄ TAB | 78 |
| 7.3.3 | Surface composition of PSS/C ₁₄ TAB mixtures | 78 |
| 7.3.4 | Foam film stability of PSS/C ₁₄ TAB mixtures | 80 |
| 7.3.5 | Application of the extended framework for foam film (de)stability of polyelectrolyte/surfactant mixtures | 82 |
| 7.4 | Conclusion | 86 |
| 8 | Polyelectrolyte backbone rigidity and its influence on structuring in bulk and confinement | 87 |
| 8.1 | Introduction | 87 |

| | | |
|-----------|---|------------|
| 8.2 | Results | 88 |
| 8.2.1 | Viscosity measurements | 88 |
| 8.2.2 | sPSO ₂ -220 structuring in bulk | 89 |
| 8.2.3 | sPSO ₂ -220 structuring in confinement | 92 |
| 8.3 | Discussion | 93 |
| 8.3.1 | sPSO ₂ -220 structuring in bulk | 93 |
| 8.3.2 | Comparison of structuring in bulk and in confinement | 96 |
| 8.4 | Conclusion | 98 |
| 9 | Two-Dimensional aggregation and semi-dilute ordering in cellulose nanocrystals | 99 |
| 9.1 | Introduction | 99 |
| 9.2 | Results | 100 |
| 9.2.1 | TEM analysis of CNC | 100 |
| 9.2.2 | SANS from CNC | 102 |
| 9.2.3 | AFM analysis of CNC | 105 |
| 9.2.4 | Interactions between CNC aggregates | 106 |
| 9.2.5 | DLS analysis of CNC | 109 |
| 9.3 | Discussion | 110 |
| 9.3.1 | Shape of CNC aggregates | 110 |
| 9.3.2 | Interactions between CNC aggregates | 112 |
| 9.4 | Conclusion | 114 |
| 10 | Summary and outlook | 115 |
| 11 | Appendix | 119 |
| | Acknowledgments | 129 |
| | Bibliography | 130 |

List of symbols and abbreviations

Symbols and Abbreviations

| | |
|------------------------|--|
| DNA | deoxyribonucleic acid |
| NR | neutron reflectometry |
| BSMP | bulk stoichiometric mixing point |
| C ₁₂ TAB | dodecyl trimethylammonium bromide |
| C ₁₄ TAB | tetradecyl trimethylammonium bromide |
| dC ₁₄ TAB | deuterated tetradecyl trimethylammonium bromide |
| cmC ₁₄ TAB | air contrast matched tetradecyl trimethylammonium bromide |
| sPSO ₂ -220 | monosulfonated poly(phenylene sulfone) |
| PAMPS | poly(acrylamido methyl propanesulfonate) |
| PSS | poly(styrene sulfonate) |
| M _n | number average molecular weight |
| M _w | weight average molecular weight |
| l _p | total persistence length |
| l _e | electrostatic persistence length |
| l _i | intrinsic persistence length |
| c* | critical overlap concentration |
| cmc | critical micelle concentration |
| cac | critical aggregation concentration |
| γ | surface tension |
| TFPB | thin film pressure balance |
| Π | disjoining pressure |
| Π _{max} | maximum disjoining pressure before film rupture |
| h | film thickness |
| Δh | stratification step width |
| CBF | Common Black Film |
| NBF | Newton Black Film |
| κ ⁻¹ | Debye length |
| Ψ ₀ | surface potential |
| I _{exp} | experimentally determined ionic strength |
| I _{max diss} | maximum ionic strength (complete dissociation) |
| I _{complex} | complex ionic strength (complete dissociation and formation of 1:1 polyelectrolyte/surfactant complexes) |
| ACMW | air contrast matched water |
| Q | momentum transfer |
| ρ | scattering length density (SLD) |
| SL | scattering length |
| Γ | surface excess |
| SANS | small angle neutron scattering |
| ζ | zeta potential |
| SAXS | small angle x-ray scattering |
| AFM | atomic force microscopy |

Continued on next page...

*Non-essential and empirical parameters are not included

| | |
|-----------------------|---|
| CP-AFM | colloidal probe - atomic force microscopy |
| SLS | static light scattering |
| DLS | dynamic light scattering |
| TEM | transmission electron microscopy |
| d | inter-chain distance |
| Q_{max} | position of the SAXS/SANS scattering maximum |
| I_{max} | maximum scattering intensity |
| d_{SAXS} | inter-chain distance d extracted from SAXS data (bulk) |
| d_{TFPB} | inter-chain distance d extracted from TFPB data (confinement) |
| d_{AFM} | inter-chain distance d extracted from AFM data (confinement) |
| l_c | correlation length |
| η | viscosity |
| CNC | cellulose nanocrystals |
| CNF | cellulose nanofibers |
| CNC-COOH | carboxylated cellulose nanocrystals |
| CNC-SO ₃ H | sulfonated cellulose nanocrystals |
| D_h | relative hydrodynamic diameter |
| D_t | translational diffusion coefficient |
| μ | electrophoretic mobility |

Chapter 1

Introduction

Polyelectrolytes are important in a diverse range of applications as in water treatment, oil recovery, as thickeners or emulsifiers and in personal care products.¹⁻⁵ Therefore, their properties in bulk, confinement and in mixtures e.g. with surfactants, were extensively investigated. Most of these investigations focused on rather flexible synthetic polyelectrolytes.^{4,6-8} However, most natural occurring polyelectrolytes as xanthan, alginates, DNA or proteins are rather rigid polyelectrolytes.⁹⁻¹¹ Furthermore, rigid rod-like nanoparticles as cellulose nanocrystals or chitin nanocrystals share some properties with rigid polyelectrolytes.^{12,13} All these materials represent abundant, eco-friendly, regenerative resources, which are yet to be used for large scale applications. Insight into their ordering mechanism at the surface, in bulk or in confinement will help to enhance their use today and identify possible applications for the future. This is essential for the conversion from fossil to regenerative resources. Moreover, to achieve a better understanding of biological processes involving DNA or proteins it is crucial to better understand their polyelectrolyte properties. Thus, the investigation of rigid polyelectrolytes/nanoparticles can help to get a deeper insight into the processes in life science or strengthen the use of e.g. eco-friendly packing in food technology.

The present thesis addresses the following issues:

- The influence of polyelectrolyte backbone rigidity on adsorption behavior, surface composition and foam film stability of oppositely charged polyelectrolyte/surfactant mixtures;
- The origin of foam film (de)stability of PSS/C₁₄TAB mixtures reported in literature¹⁴ is identified by investigating the mixtures surface composition;
- The influence of polyelectrolyte backbone rigidity on structuring in bulk and confinement;
- The aggregation and structuring of rigid rod-like shaped cellulose nanocrystals;

The first part of this thesis, chapter 5, determines the surface adsorption and foam film stability of a rigid polyelectrolyte (sPSO₂-220)/surfactant (C₁₄TAB) mixture using surface tension measurements and the thin film pressure balance (TFPB). In order to understand the role of polyelectrolyte backbone rigidity in surface adsorption and foam film stabilization the results were compared to mixtures containing more flexible polyelectrolytes (PSS or PAMPS).^{14,15}

After the characterization of the fundamental adsorption behavior and foam film stability, the second part of this thesis, chapter 6, uses neutron reflectometry (NR) to investigate the exact surface composition of the sPSO₂-220/C₁₄TAB mixtures and correlates it to the foam film stability. This helps to understand the origin of foam film stability for rigid polyelectrolyte/surfactant mixtures.

The third part of this thesis, chapter 7, investigates PSS/C₁₄TAB mixtures. In the literature these mixtures were found to be unable to form foam films, while similar PSS/C₁₂TAB mixtures formed quite stable foam films.¹⁴ The exact surface composition of PSS/C₁₄TAB mixtures was identified with NR and the foam film stability was remeasured with the TFPB. The results were used to clarify the reasons for the observed foam film destabilization for this specific mixture.

In the fourth part of this thesis, chapter 8, the structuring of polyelectrolytes with respect to their backbone rigidity is discussed. The structuring of flexible polyelectrolytes in bulk and confinement is a well investigated phenomena.^{6,8,16} Only for some rigid polyelectrolytes structuring was found^{17,18}, while others did not show any structuring¹⁹. Therefore, in this chapter the influence of polyelectrolyte backbone rigidity (rigid sPSO₂-220 vs. flexible PSS¹⁶) on the structuring is investigated in aqueous solutions with and without geometrical confinement by using TFPB and small angle x-ray scattering (SAXS).

The final part, chapter 9 focuses on the aggregation and structuring of cellulose nanocrystals (CNC). CNCs are rigid rod-like shaped nanocrystals, extracted from cellulose producing plants. The high stiffness, high aspect ratio, dispersibility, biocompatibility and low cost make them interesting for a lot of applications e.g. in nanocomposites, food packaging or biomedicine.¹² Thus, controlling the surface and size parameters and hence the colloidal behavior of CNC suspensions is desirable. As the former investigated polyelectrolytes, CNCs are charged and hence exhibit electrostatic inter-particle interactions and show structuring at higher concentrations. The shape and structuring of different CNCs was investigated by scattering and imaging techniques and correlated to the respective preparation route.

Chapter 2

Scientific background

2.1 Adsorption at the air/water interface

Water on its own is not able to form foams. Molecules or particles have to be adsorbed at the air/water interface to make foaming possible.^{4,20}

2.1.1 Adsorption from surfactant solutions

Surfactants are an example for such molecules. They accumulate at the air/water interface and as a result influence the surface properties and induce foamability.^{20,21} Other examples would be (nano)particles or proteins.^{4,20} The reason for the surface activity of surfactants is their chemical structure. Surfactants contain both a hydrophilic and a hydrophobic part and hence have an amphiphilic character.²¹ The hydrophobic part is mostly an alkyl chain, which is also called hydrophobic tail. Whereas the hydrophilic part, known as the headgroup, is smaller and can be of different chemical compositions. The type of headgroup is the most common property to distinguish between different types of surfactants: anionic, cationic, amphiphilic and nonionic.²¹

In aqueous solution ionic surfactants dissociate into a charged surface active part and an oppositely charged inorganic counter ion. The surface active part adsorbs at the air/water interface. The surfactants hydrophilic headgroup is located in the water phase and the hydrophobic alkyl chain is exposed to the gas phase. Surfactants at the surface reduce the surface tension of the liquid.²¹ The reason for this is that the water surface (high surface tension) is displaced by a hydrocarbon surface (lower surface tension). With growing surfactant concentration this effect will increase and surface tension will decrease further. This process continues until a certain surfactant concentration, also called the critical micelle concentration (cmc), is reached.²¹ Independently from increasing surfactant concentration, the surface tension does not change anymore above this point. Additional surfactant molecules do no longer adsorb at the surface, they start to form aggregates (micelles) in the bulk phase.²¹

Measurements of parameters as surface tension or surface elasticity and the use of ellipsometry give valuable information about the adsorption of surfactants at air/water interfaces.²² However, for example in case of mixtures of surface active agents, no information about the composition of the layer(s) adsorbed at the air/water interface is accessible using

those techniques. Furthermore, also the structure of the adsorbed compounds (monolayer, double layer, extended layer etc.) is not accessible by investigating the surface tension and surface elasticity or by using ellipsometry. Neutron reflectometry (NR) can be used to get a deeper insight into the composition and structure of the adsorbed layers at the air/water interface by using isotropic contrast variation.^{22–24}

2.1.2 Adsorption of oppositely charged polyelectrolyte/surfactant mixtures

Polyelectrolytes are polymers with ionizable groups and hence dissociate in water into charged polymer chains (macroions) and counterions.^{25,26} The properties of polyelectrolytes in aqueous solution are governed by a wide range of parameters such as e.g. chemical composition, molecular weight, degree of charge, pH and ionic strength.^{25,26} The polyelectrolyte persistence length l_p (i.e. backbone rigidity) is another important parameter for the determination of polyelectrolyte properties.^{25,26} The higher the persistence length l_p the stiffer is the polyelectrolyte backbone. For polyelectrolytes the total persistence length l_p consists of the intrinsic persistence length l_i and the electrostatic persistence length l_e .²⁶ The electrostatic persistence length l_e describes the part of persistence length, due to the repulsion of the charges within the polyelectrolyte chain. It depends on external parameters as the polyelectrolyte concentration, the dissociation degree and additional ionic strength. The intrinsic persistent length l_i is a result of the pure polymer backbone rigidity and independent of external parameters. When the charges of a polyelectrolyte are screened and do not repulse each other anymore, the total persistence length l_p is equal to the intrinsic persistence length l_i . For polyelectrolytes the intrinsic persistence lengths are typically compared, since the electrostatic persistence length is easily influenced by external parameters.²⁶

Mixtures of oppositely charged polyelectrolytes and surfactants can form highly surface-active complexes due to electrostatic interactions.^{4,8,22,27,28} Hence, oppositely charged polyelectrolyte/surfactant mixtures play an important role in a wide range of applications as in cleaning agents, enhanced oil recovery, detergency, personal care and fire fighting.^{1–3,5,29,30} Mixtures of neutral surfactants and polyelectrolytes as well as mixtures of likewise charged surfactants and polyelectrolytes also show interesting adsorption properties.^{4,7,8,25,31–34} However, in this work only mixtures of oppositely charged surfactants and polyelectrolytes are investigated and discussed. Hence, in the following the term polyelectrolyte/surfactant mixtures always represents mixtures of *oppositely charged* polyelectrolytes and surfactants. Furthermore, in the literature (and in this work) mostly

mixtures of anionic polyelectrolytes and cationic surfactants are studied.^{8,14,15,35–38} Nevertheless, mixtures of cationic polyelectrolytes and anionic surfactants show very similar features.^{7,39–41}

Most polyelectrolytes do not adsorb on their own at the air/water interface as they miss the amphiphilic character of surfactants. The formation of polyelectrolyte/surfactant complexes is energetically favorable due to the decrease in electrostatic repulsion (between positively charged surfactant headgroups at the surface) and the increase in entropy due to the release of counterions.^{42,43} The resulting polyelectrolyte/surfactant complexes can decrease the surface tension far stronger than the single pure components.^{8,14,15} In general the surface tension and its investigation is far more complex for polyelectrolyte/surfactant mixtures than for pure surfactant solutions or for mixtures of surfactant with neutral polymers.^{7,22} For example, the adsorption process for polyelectrolyte/surfactant mixtures is significantly slower than for pure surfactants.^{44–47} Therefore, regarding the appropriate equilibration time is crucial. After all, aging (for example due to precipitation) in these mixtures also can be a problem and has to be taken into account.^{47,48}

Already the addition of a small amount of polyelectrolyte to a surfactant solution often leads to a strong decrease in surface tension,^{8,15,28,42} due to the strong synergistic interaction. However, the addition of more polyelectrolyte does not necessarily leads to a reduction of surface tension for all polyelectrolyte/surfactant ratios.^{8,15,28,48–50} At and slightly beyond the bulk 1:1 stoichiometric mixing point (BSMP) polyelectrolyte/surfactant mixtures typically show an increase in surface tension. This increase is characteristic for those mixtures and its origin was extensively discussed in the literature.^{8,48–50} Several explanations for this phenomena were found, such as the loss of surface activity of polyelectrolyte/surfactant complexes at chemical equilibrium^{49,51} or depletion of the surface due to precipitation of complexes in bulk^{50,52}. Beyond the BSMP the surface tension of polyelectrolyte/surfactant mixtures strongly varies, e.g depending on the hydrophilicity of the respective polyelectrolyte surfactant complexes. For example poly(styrene sulfonate)(PSS)/C₁₄TAB mixtures show a very strong depletion from the surface, which was explained by the formation of hydrophilic complexes in bulk.^{14,36,53} For poly(acrylamido methyl propanesulfonate) (PAMPS)/C₁₄TAB mixtures beyond the BSMP at first the surface tension increases with increasing polyelectrolyte concentration, then it decreases again.¹⁵ This can be explained by the formation of PAMPS/C₁₄TAB complexes in bulk up to a concentration of $5 \cdot 10^{-4}$ (mono)M PAMPS. Beyond this concentration the complexes adsorb again at the surface.¹⁵ It can be concluded that the surface tension of different polyelectrolyte/surfactant mixtures show some similarities, but also strongly depends on a

lot of parameters e.g. the polyelectrolyte type,²⁸ polyelectrolyte charge,⁵⁴ polyelectrolyte concentration,^{35,36,55} polyelectrolyte molecular weight,⁵⁶ surfactant chain length,^{36,54,55} and polyelectrolyte/surfactant charge ratio³⁷. The persistence length l_p also influences the adsorption of polyelectrolyte/surfactant mixtures at the air/water interface⁵⁷ and is discussed in chapter 2.2.2.

2.2 Foam films as building blocks of macroscopic foams

Foam properties are of interest for many applications such as enhanced oil recovery, fire fighting, advanced material synthesis and of course in personal care products. Foams and their properties are thus the subject of many investigations.^{4,20,58-61} In some processes e.g. fire fighting a foam is desired, while in others (e.g. in washing machines) foaming should be avoided. That shows the high importance of foam stability control.^{20,61} In order to understand properties as foam stability and foamability of a macroscopic foam, it is essential to understand the behavior of the single building blocks, so-called foam films. Foams contain both a continuous phase, which is usually an aqueous solution that separates the single air bubbles from each other and a dispersed phase consisting of the air bubbles. Foam films represent the continuous phase and can be understood as channels between the air bubbles, which are of significant importance for foam destabilizing processes as drainage, coalescence and coarsening.²⁰ Surface active molecules as surfactants or particles adsorb at the interface between the continuous (aqueous) and the dispersed (air) phase. For thin foam films (thinner than 100 nm) the interactions between the opposing surfaces become more and more important. Those interactions are known as the disjoining pressure (discussed in chapter 4.2) and depend strongly on the composition of the surfaces and on the structuring of the solutes in the film bulk (discussed in chapter 2.2.3). In general two types of foam films, depending on the respective stabilization mechanism, can be formed as the final state before film rupture. Common black films (CBF) have a thickness of about 10 to 100 nm and are mainly stabilized by electrostatic forces. Very thin films with a thickness below 10 nm are called Newton black films (NBF) and are mainly stabilized by steric forces.^{8,28} Inside a NBF there are no free water molecules, but only bound hydration water around the surfactants headgroups. Therefore, the film thickness is roughly twice the length of the surfactant molecule.⁶² Typically, the transition from a CBF to a NBF is discontinuous and appears as a step in the disjoining pressure isotherm (also discussed in chapter 2.2.3).^{63,64}

2.2.1 Foam films formed by pure surfactant solutions

As mentioned pure water is not able to form stable foam films. Surfactants have to be added to the system to stabilize foam films. Depending on the type and concentration of the surfactant and additional parameters as the ionic strength, pH etc., the properties of foam films can differ strongly.^{20,63}

For ionic surfactants, the charge of the film surface is determined by the surface coverage and the dissociation degree of the surfactant. On the one hand, with increasing surfactant concentration, the charge at the surface increases, leading to a higher repulsion between the two interfaces.⁶³ On the other hand, the dissociation of the surfactant molecules increases the ionic strength and thus the electrostatic screening, counteracting the above described effect.⁶³ Usually, the increase of the surfactant concentration leads to thinner and more stable films, indicating that the electrostatic screening dominates the interactions in the film.^{63,65} Ionic surfactants typically form CBFs as the repulsion between the interfaces prevents the transition to a NBF.^{58,65} However, if a high amount of salt is added, which significantly exceeds the surfactant concentration, the screening of the surface charges gives rise to a CBF-NBF transition.⁶⁵

Nonionic surfactants also form CBFs for lower concentrations, while above a certain surfactant concentration a transition to a NBF can be observed.⁶⁶ As mentioned a CBF requires electrostatic repulsion between the two interfaces, which can not be originated from the nonionic surfactant. Hence, the formation of a CBF indicates the presence of charges at the air/water interface. For higher nonionic surfactant concentrations these charges are replaced and a NBF can form.^{63,66} Different experimental and theoretical studies have investigated the type and source of charges of a pure water surface. Most of these studies indicate a negative charge at the air/water interface.^{63,67,68} The origin of the charge is still under debate, but an excess of OH^- molecules at the air/water interface is often given as a possible explanation.^{63,68} Foam films formed by pure surfactant solutions are especially stable, when the surface tension is low and the surface elasticity is high.^{58,69,70}

2.2.2 Foam films formed by oppositely charged polyelectrolyte/surfactant mixtures

As mentioned in chapter 2.1.2 by mixing polyelectrolytes and surfactants, highly surface-active complexes can form due to electrostatic interactions.^{8,22} These complexes can be used to produce very stable foam films and are important in a wide range of applications

discussed in chapter 2.1.2. However, polyelectrolyte/surfactant mixtures do not necessarily form a more stable foam film for all polyelectrolyte/surfactant ratios, in comparison to foam films formed by pure surfactants.^{8,14,15,28,33,37} The complexes and their influence on foam film stability have been extensively investigated in the last years.^{8,14,15,28,71} One finding was that it is difficult or even impossible to predict foam film stability only from the surface coverage, i.e. surface tension.^{8,14,28} Especially close to the BSMP surface tension and surface elasticity experiments can show a strong adsorption of surface active complexes, though it was not possible to form stable foams for these concentrations.^{15,72,73} It can be concluded that surface coverage alone is not crucial for foam film stability. Instead foam films are stable especially at concentrations where the surface tension is high and hence less polyelectrolyte/surfactant complexes adsorbed at the surface. In that case zeta potential measurements indicated strongly charged complexes in bulk.⁷¹ Therefore, besides surface coverage, also the total net charge in the system is governing foam film stability.^{15,71,72}

As mentioned, neutron reflectometry (NR) can be used to get a deeper insight into the composition of the adsorbed polyelectrolyte/surfactant layers at the air/water interface by using isotropic contrast variation.^{22,24} Only very recently the surface composition from these experiments was correlated to foam film stability experiments.⁷¹ The earlier assumption that the surface charge is not only a result of molecules directly adsorbed to the surface, but is also strongly influenced by polyelectrolyte complexes in bulk, was confirmed.^{15,71} After all, these NR experiments also showed that for some polyelectrolyte/surfactant ratios the surface charge is not the only decisive parameter for foam film stability. For PAMPS/C₁₄TAB the surface composition indicated a high surface charge close to the BSMP, while no stable foam film was found.⁷¹

For polyelectrolyte/surfactant mixtures the influence of different parameters such as polyelectrolyte/surfactant type,^{14,33} polyelectrolyte/surfactant ratio,¹⁵ polyelectrolyte/surfactant hydrophobicity,¹⁴ polyelectrolyte/surfactant charge ratio,³⁷ pH⁴¹ and surfactant head group⁴¹ on the adsorption at the air/water surface and foam film properties were extensively investigated. However, for most of the investigated polyelectrolyte/surfactant mixtures the polyelectrolyte backbone was quite flexible, as it is the case for example for PAMPS^{14,15,37} and poly(styrene sulfonate) (PSS)¹⁴. Both have an intrinsic persistence length l_p of 1 nm. The main difference between the two is that PSS is more hydrophobic while PAMPS is more hydrophilic, which leads to a significantly differing adsorption behavior of the resulting polyelectrolyte/surfactant complexes.^{14,15,36}

Only little work has been done to investigate the influence of a more rigid polyelectrolyte backbone on the surface adsorption and foam film properties of polyelectrolyte/surfactant

mixtures.⁵⁷ The adsorption of mixtures containing PAMPS, PSS, DNA or Xanthan (with l_p of 1 nm; 1 nm; 50 nm and 150 nm) with C₁₂TAB on the air/water interface was investigated.⁵⁷ Here, it was found that for more rigid polyelectrolytes denser films are formed at the air/water interface. Hence, to the author's knowledge no fundamental study examining the influence of polyelectrolyte backbone rigidity on both surface adsorption and foam film properties of polyelectrolyte/surfactant mixtures was conducted so far.

2.2.3 Stratification in polyelectrolyte/surfactant foam films

An important topic in the investigation of foam films containing polyelectrolyte, surfactants, nanoparticles or their mixtures is the stepwise thinning of a film, called stratification. Here, the film drains stepwise due to an oscillation of the disjoining pressure.^{8,17,31,64,74,75} This oscillation is induced by a transient network of polyelectrolyte chains in the film core, that is formed above the critical overlap concentration (c^*)^{43,76}, and/or by the layering of micelles, respectively⁶⁴. This phenomena is typically observed below the cac in the semidilute concentration regime of polyelectrolytes.⁷⁷ Stratification is an irreversible process. If the pressure is reduced again, the foam film will not be able to return to its initial thickness. The steps in thickness reduction Δh follow a power law that scales with $\Delta h \propto c^{-1/3}$ for spherical objects as silica nanoparticles⁷⁸⁻⁸⁰ and branched polyelectrolytes^{81,82}. In case of a linear polyelectrolyte, the thickness reduction Δh follows a power law that scales with $\Delta h \propto c^{-1/2}$.^{16,26,83} This thickness reduction corresponds to the mesh size of the polymer network that is formed in the bulk.^{31,63,83,84} Furthermore, for polyelectrolytes the power law also changes with the concentration of the polyelectrolyte. For dilute solutions the power law is $\Delta h \propto c^{-1/3}$ (corresponding to single polyelectrolyte coils with $c < c^*$), while for semidilute solution it is $\Delta h \propto c^{-1/2}$ (corresponding to a transient network with $c > c^*$).^{16,83}

The stratification process can be affected by different parameters such as salt concentration,^{43,85} polyelectrolyte concentration^{43,85} and polyelectrolyte charge^{32,85}. The type of surfactant, and hence the charge of the surface, and the surface elasticity have no influence on the structuring of the polyelectrolyte chains,³³ but on the stratification dynamics^{86,87}. Polyelectrolyte backbone rigidity also plays a major role in the stratification process.^{17,18} In ref. 17 the stratification behavior for mixtures of PSS ($l_p = 1$ nm) and Xanthan ($l_p = 150$ nm) with dodecyltrimethylammonium bromide (C₁₂TAB) was studied. Despite the large difference in the polyelectrolyte backbone rigidity the stratification behavior was very similar.¹⁷ In ref. 18 mixtures of PAMPS, Carboxymethyl-chitin, DNA or Xanthan

(with l_p of 1 nm; 5 nm; 50 nm and 150 nm) with nonionic surfactants were investigated. Stratification was found for flexible polyelectrolytes, while for rigid polyelectrolytes stratification was dependent on the viscosity of the system.¹⁸ For flexible polyelectrolytes the force oscillation can be observed as long as the velocity of the two approaching surfaces is not too fast.¹⁸ For rigid polyelectrolytes stratification was only found when the viscosity of the solution is large enough so that the network has time to adjust, otherwise it was not observed.¹⁸ However, when stratification appears the resulting stratification parameters as the step width Δh seem to be independent of the persistence length.¹⁷

Stratification in foam films is typically investigated with a thin film pressure balance (TFPB) (described in chapter 4.2).^{17,18,63,64,73,74,77} However, stratification does not only occur in foam films, but also between two closely approaching solid surfaces. Here, colloidal probe - atomic force microscopy (CP-AFM) can be used for investigation.^{6,16,64,74,88} For CP-AFM measurements more parameters (as the correlation length and correlation strength) compared to TFPB measurements are accessible.^{64,78,88} Furthermore, the addition of surfactant, which might influences stratification parameters, is not necessary.^{64,78} For CP-AFM measurements the approach velocity of the two surfaces can be adjusted and hence stratification kinetics are accessible.^{18,89} Typically, the parameters extracted under confinement with TFPB or CP-AFM are compared to the same parameters extracted in bulk.^{16,84} By applying small angle scattering (with neutrons or x-rays) a scattering curve in dependence of scattering angle and wavelength can be extracted.^{26,90} If the curve shows a peak the inter-chain distance, correlation length and correlation strength can be extracted with a Lorentzian fit (also discussed in chapter 8 and chapter 9).⁸⁴ In some studies no or only insignificant differences between confinement and bulk was found.^{17,31,32,84,91,92} In other studies for semidilute polyelectrolyte solutions a reduction of the mesh size under confinement of up to 20 % was observed.^{16,93,94}

2.3 Cellulose nanocrystals

Nanocellulose represents, alongside DNA, virus and protein based materials, an emerging class of biological nanomaterials.^{12,95} Over the last two decades detailed investigations have revealed the cellulose crystal structure⁹⁶ as well as nanocellulose organization and properties of macroscopic materials.^{97,98} So far, the mesoscopic length scale, bridging the internal cellulose chain organizations in the cellulose nanoparticles and the final cellulose configuration in materials, has not been fully elucidated. This leaves room for further

studies with the potential to create new material designs from self-assembly of cellulose nanoparticles on the mesoscale.

Cellulose nanocrystals (CNCs) extracted from natural sources, e.g. wood are a promising renewable building block material. Their high stiffness, high aspect ratio, dispersibility, biocompatibility and low cost^{12,99} make them interesting for a lot of applications e.g. in nanocomposites^{100,101}, food packaging^{102,103} or biomedicine^{104,105}. Thus, controlling the surface and size parameters and hence the colloidal behavior of CNC suspensions is desirable. This can be done by varying the raw material^{106,107} or by changing the preparation route^{108,109}. CNCs possess both similar and differing properties compared to the polyelectrolytes investigated in this thesis. A difference is that CNCs are rod-like particles consisting of many ordered cellulose macromolecules, while polyelectrolytes are single chain molecules, which show ordering only for higher concentrations. A similarity is that both are stabilized in aqueous solutions by the repulsive interactions of their charged groups. Hence, CNCs can be understood as rigid rod-like aggregates of polyelectrolytes. Their investigation continues and enhances the investigation of structuring for rigid polyelectrolytes which was conducted in chapter 8.

The most common type of CNC preparation is based on sulfuric acid hydrolysis of micrometer sized cellulose particles.^{110,111} This preparation route, has been very successful to prepare CNC based liquid crystals and nanomaterials. It has, however, some drawbacks in that the amount and alkaline stability of the sulfate ester charged groups is limited.^{109,112} An alternative preparation route is to combine hydrochloric/hydrobromic acid hydrolysis with oxidative carboxylation.^{109,113} This leads to carboxyl instead of sulfate groups on the CNC surface. The carboxyl groups are more stable under alkaline conditions than the sulfate ester groups, leading to a broader application range of CNC.^{109,112} The number density of carboxyl groups can be tuned by the oxidation conditions and a higher charge density can be reached, compared to the sulfuric acid preparation¹¹⁴, thus improving the particle's dispersion capability and colloidal stability. The different reaction conditions, compared to sulfuric acid hydrolysis, also lead to higher aspect ratios of the carboxylated CNC in comparison to sulfated CNC.¹⁰⁹ Moreover, the carboxylic groups, more amenable to surface modification than the hydroxyl group typically used to modify sulfuric hydrolyzed CNC, can be easily chemically modified to further change the properties of the CNC surface.^{100,112,113}

CNCs are known to self-assemble into chiral nematic liquid crystals above a threshold particle concentration¹¹⁰, forming locally well-ordered CNC arrangements. Physical templates¹¹⁵ or external fields^{111,116,117} can increase the scale of local organization from

the micrometer towards the centimeter length scale. However, to the author's knowledge, the mechanism behind the isotropic to chiral nematic transition is not fully understood yet.^{100,114} High resolution microscopy recently revealed detailed structural information about the right-handed chirality of individual cellulose fibrils.¹¹⁸ While this observation gives important structural information, it is clear that more data of CNC arrangements, on the length scale between a single cellulose particle and that of the inter-particle spacing in the liquid crystal state, is needed to understand the self-assembly of CNC.

Chapter 3

Materials and sample preparation

3.1 Surfactants

The surfactant tetradecyl trimethylammonium bromide (C_{14} TAB) was purchased from Sigma-Aldrich (Steinheim, Germany) and recrystallized three times in acetone with traces of ethanol. C_{14} TAB was chosen as a surfactant, as it is the shortest surfactant in the C_n TAB series that forms stable films on its own.⁵⁸ This makes it possible to investigate the whole concentration regime from films of pure surfactant solutions, over those which contain a low amount of polyelectrolyte to films with a high polyelectrolyte concentration. The purity of the surfactant was verified by surface tension measurements. All solutions were prepared with Milli-Q water (total organic content = 4 ppb; resistivity = 18 m Ω cm) with a surfactant concentration of 10^{-4} M. This concentration is well below the cmc of $3.7 \cdot 10^{-4}$ M for C_{14} TAB.⁶⁶ Its chemical structure is shown in Fig. 3.1.

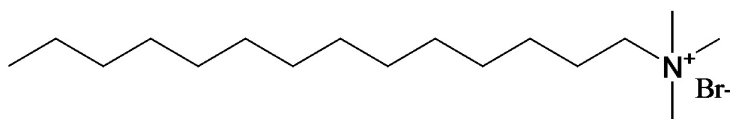


Figure 3.1: Chemical structure of C_{14} TAB

For neutron reflectometry (NR) experiments C_{14} TAB with a deuterated alkyl chain (dC_{14} TAB) was purchased from CDN Isotopes (Quebec, Canada) and used as received.

3.2 Polyelectrolytes

Monosulfonated poly(phenylene sulfone) (sPSO₂-220) was synthesized by the group of Klaus-Dieter Kreuer (Max Planck Institute for Solid State Research, Stuttgart) according to the guidelines in the literature.¹¹⁹ It has a molecular mass of 100000 g/mol with Li^+ as counterion. Its chemical structure is shown in Fig. 3.2.

sPSO₂-220 was diluted and centrifuged at 4000 rpm for 60 min. The supernatant was collected and the resulting solution pressed through a syringe filter of 0.2 μ m. Afterwards, the resulting solution was again centrifuged with 7500 rpm for 3 runs for 15 min against centrifugal filters (Amicon Ultra 10K, Merck Millipore, Germany). Between the runs the supernatant was diluted with deionized water. Therefore, small ion impurities from

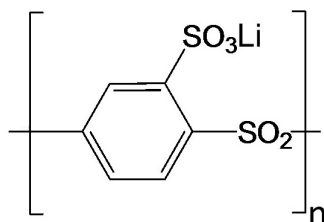


Figure 3.2: Chemical structure of sPSO₂-220

synthesis were removed. The supernatant sPSO₂-220 was then freeze dried and afterwards rediluted for experiments.

Sulfonated poly(phenylene sulfones) are a novel class of polyelectrolytes,^{119,120} which are of interest due to their high proton conductivity and their high thermal, thermo-oxidative and hydrolytic stabilities.^{120,121} These properties make sPSO₂-220 a promising material e.g. for fuel cells.¹²² Dissipative particle dynamics (DPD) simulations have shown that the sPSO₂-220's polyelectrolyte backbone is significantly stiffer as for example the polyethylene backbones of poly(acrylamido methyl propanesulfonate) (PAMPS) or poly(styrene sulfonate) (PSS).^{123,124} Using static light scattering (SLS) an intrinsic persistence length of 20 ± 2 nm was found.¹²⁵ Furthermore, sPSO₂-220's sulfonate group is strongly acidic due to the electron withdrawing sulfonyl group (-SO₂-). The comparatively high acidity leads to high dissociation degrees of 54 - 61 %, ^{126,127} in comparison to a dissociation degree of 33 - 38 % for PSS or PAMPS^{128,129}. sPSO₂-220 was chosen as it is chemically quite similar to PSS which is extensively used as a model system for polyelectrolyte/surfactant interactions.^{14,35,46,49,50,53,55,57,130} Hence, by using sPSO₂-220 the influence of backbone rigidity and the higher dissociation degree on the properties of polyelectrolyte/surfactant mixtures can be analyzed systematically.

For the NR and thin film pressure balance (TFPB) experiments in chapter 7 poly(styrene sulfonate) (PSS) (analytical standard, $M_w = 77400$ g/mol and $M_w/M_n=1.1$) was purchased from Sigma-Aldrich (Steinheim, Germany) and used as received. In chapter 5 the current results on sPSO₂-220 were compared to earlier experiments where a different PSS sample was used.¹⁴ This PSS had a M_w of 70000 g/mol and was purified in an ultrafiltration cell with a cut-off membrane of 20000 Da. It was assumed that the ultrafiltration cell was able to remove all small ion impurities and the 10 % difference in molecular weight has no significant influence on adsorption and foam film properties. The chemical structure of PSS is shown in Fig. 3.3

The flexible polyelectrolyte poly(acrylamido methyl propanesulfonate) (PAMPS) was not

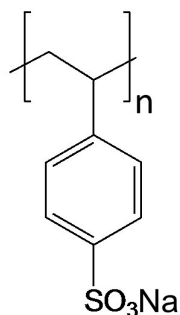


Figure 3.3: Chemical structure of PSS

used in any experiments of this thesis. However, it is used for comparison of the present results with the findings for a more flexible and hydrophilic polyelectrolyte. PAMPS had a molecular mass of 100000 g/mol.⁷¹ All the results shown here are either extracted from the PhD theses of Nora Kristen-Hochrein¹³¹ or Heiko Fauser¹³². The chemical structure of PAMPS is shown in Fig. 3.4.

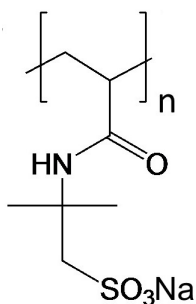


Figure 3.4: Chemical structure of PAMPS

The sample solutions were prepared by combining equal volumes of polyelectrolyte and C_{14}TAB stock solutions with twice the desired concentration of the respective substance. All glassware (except the foam film holder for TFPB experiments) was cleaned with the basic detergent mixture Q9 (Ferak Berlin GmbH) and rinsed thoroughly with water before use. In chapters 5 - 7 the polyelectrolyte concentration was adjusted below its critical overlap concentration c^* and the surfactant concentration below its critical micelle concentration (cmc), in order to avoid stratification (discussed in chapter 2.2.3). In chapter 8 the aim was to investigate the influence of backbone rigidity on stratification and bulk ordering. Thus, higher polyelectrolyte concentrations were used.

3.3 Cellulose nanocrystals

In chapter 9 the shape and interaction properties of carboxylated cellulose nanocrystals (CNC-COOH) and sulfonated cellulose nanocrystals (CNC-SO₃H) are compared. The preparation of both types of CNCs is described in the literature.^{112,133,134}

Chapter 4

Experimental techniques

4.1 Characterization of surface adsorption

Surface tension

Surface tension measurements have been performed to get information about the strength of adsorption of polyelectrolyte/surfactant complexes at the air/water interface. The surface tension of liquids is a result of differences in the energy state between the molecules at the liquid surface and those in the liquid bulk. Molecules located at the surface are only partly surrounded by other molecules and thus possess less attractive interactions to neighboring molecules than molecules located in the bulk phase. For this reason, it is energetically not favored for molecules to be exposed on the surface. As follows, the energy difference pulls molecules from the surface into the bulk phase. Therefore, liquids have a surface as small as possible and a work w has to be done to increase their surface area A .^{21,135}

$$w = \int_0^A \gamma dA = \gamma A \quad (4.1)$$

The surface tension γ is the constant of proportionality.¹³⁵ The surface tension was measured with a K11 tensiometer (Kruess, Germany) using the du Noüy ring technique. A metal ring made of a thin Pt/Ir wire (with radius R), is immersed into the sample solution and slowly pulled out. The surface tension is then obtained from the force that is necessary to detach the ring from the surface of the liquid.^{21,135}

$$\gamma = \frac{F}{4\pi R} \quad (4.2)$$

Each sample solution was prepared one day beforehand. Prior to each measurement the sample solutions (with twice the desired concentrations) were mixed in a Teflon vessel (diameter 5 cm) and equilibrated for 2 h. The surface tension was measured at 25 °C until a constant value was recorded over more than 20 min. When assuming that the changes in surface composition, occurring during the approach of the two air/water interfaces upon film formation, are only minor, the results of surface tension measurements can also be

transferred to film surfaces and to thin film pressure balance (TFPB) experiments (see Chapter 4.2).¹³⁶

Surface Elasticity

As rheological parameters of the adsorbed layer at the air/water interface are very important for foam film stability,^{58,70} surface elasticity measurements with the oscillating drop technique were performed. This technique examines the response of the surface tension to the dilational deformation of the adsorbed layer (expansion and contraction of the surface). Therefore, the surface area of a drop is changed by generating harmonic oscillations while simultaneously the surface tension is recorded.^{137,138} The basics of the underlying pendent drop technique can be found in the literature.^{21,139,140}

In the oscillating drop technique the variation of the surface area δA of the pendent drop causes a change of the surface concentration of the adsorbed surfactants. Surface expansion leads to a decrease in the surfactant surface concentration and thus to an increase in the surface tension γ . Vice versa the contraction of the surface results in a decrease of γ . Furthermore, molecular exchange with adjacent bulk molecules can take place. At a given area variation the change in surface tension is a measure of the dilatational elastic modulus ϵ .^{137,138} The dilatational elastic modulus ϵ was calculated according to the following equation:

$$\epsilon(\omega) = \epsilon_r + i\epsilon_i = \frac{\delta\gamma}{\delta \ln A} \quad (4.3)$$

The surface elastic modulus was calculated from the amplitude ratio of the oscillating surface tension and surface area, whereas the phase shift between the two determines the dilatational surface viscosity.¹³⁸ The exact calculation routine can be found in the literature.¹³⁷

The elastic modulus of the polyelectrolyte/surfactant mixtures surface were measured at room temperature using a PAT1 (Sinterface Technologies, Berlin, Germany). The device created a pendant drop of the mixture at the tip of a capillary. This capillary was placed in a closed cuvette containing a small reservoir of sample solution to prevent evaporation. The drop was equilibrated for 2 h prior to each measurement. To determine the elastic modulus, harmonic oscillations of the drop surface were induced by a computer-controlled dosing system. Surface area A and surface tension γ were calculated as a function of time

via drop shape analysis. The oscillation frequencies are varied between 0.005 and 0.2 Hz with at least four full oscillation cycles per frequency. For this technique, the generated harmonic oscillations must not exceed 1 Hz, because only at low frequencies the drop keeps its Laplacian shape.^{138,141}

4.2 Thin film pressure balance (TFPB)

Basic Principles and Setup

Disjoining pressure isotherms were measured with porous glass discs and the thin film pressure balance (TFPB) technique.^{62,142} With this method free-standing horizontal liquid foam films can be investigated. Thus, information about interaction forces, thicknesses, drainage and stabilities of thin foam films are accessible. A full description of the setup can be found elsewhere.⁶³ In principle, the TFPB setup consists of a stainless steel measuring cell that is equipped with a quartz glass window to monitor the film. The porous glass disc (with a hole of 1 mm in diameter) is placed in the sealed cell and connected to the ambient reference pressure. A reservoir of the sample solution is located in the cell to provide a saturated vapor atmosphere during the measurement. The applied pressure is adjusted via a motor-driven syringe pump and controlled by a computer. The increase of the gas pressure in the chamber leads to a flow of the excess liquid from the glass disc hole through its pores, and a symmetric foam film is formed inside the hole. At equilibrium, the difference between the inner and the outer pressure is balanced by disjoining pressure Π .^{62,142} The film is observed with an optical microscope (Nikon, Düsseldorf, Germany) and illuminated by cold filtered white light to avoid additional energy input in the system. The reflected light beam is split into two parts: one part is used to monitor the film with a CCD video camera (Pulnix Deutschland GmbH, Alzenau, Germany), while the other part is sent through a narrow band-pass filter ($\lambda = 550$ nm) and amplified by a photomultiplier. From the measured intensity of the reflected light, the film thickness is calculated.⁶³ A sketch of the apparatus is shown in Fig. 4.1.

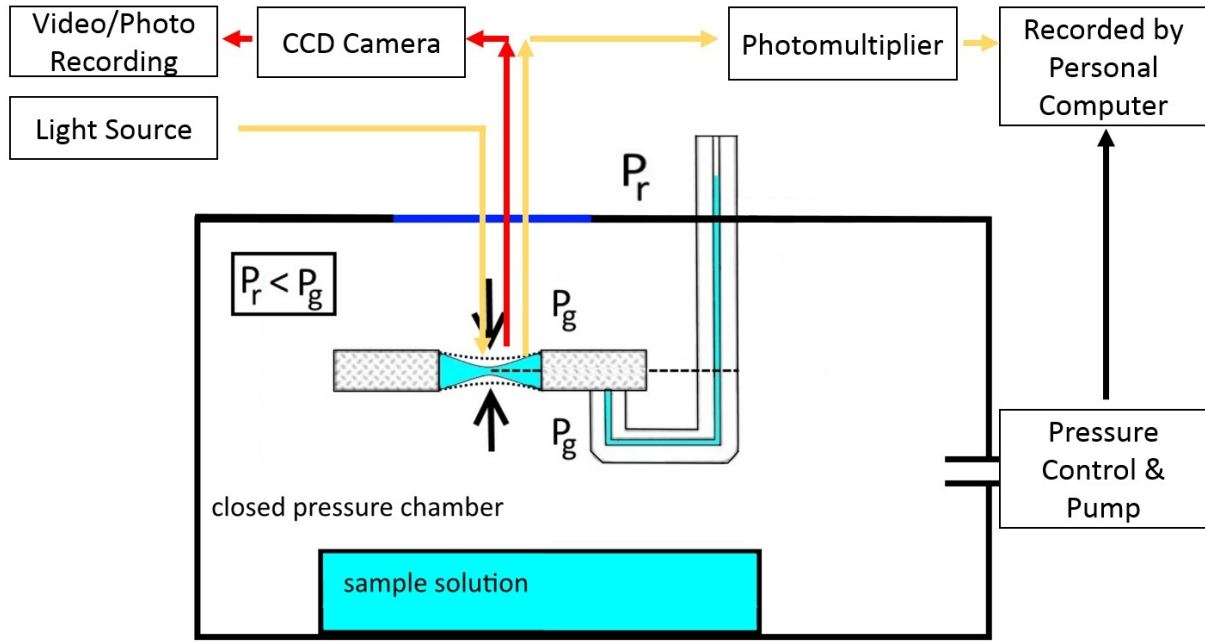


Figure 4.1: Sketch of a thin film pressure balance (TFPB) setup.

Disjoining pressure Π

The disjoining pressure Π stabilizes foam films. It is a result of interacting forces between the two interfaces of the foam films. It consists of the sum of long-range repulsive electrostatic (Π_{elec}), short-range attractive van der Waals (Π_{vdW}) and short-range repulsive steric (Π_{steric}) pressures.^{62,63}

$$\Pi = \Pi_{elec} + \Pi_{vdW} + \Pi_{steric} \quad (4.4)$$

In equilibrium the disjoining pressure Π can be calculated according to:⁶²

$$\Pi = P_g - P_l = P_g - P_r + 2\sigma/r - \Delta\rho gh_c \quad (4.5)$$

with P_l and P_r are the liquid and the external reference pressures (i.e. atmospheric pressure), respectively, σ is the surface tension of the sample solution, r is the radius of the glass tube, $\Delta\rho$ the density difference between the sample solution and air, g is earths gravitational acceleration (9.81 ms^{-2}) and h_c is the height of solution in the glass tube beyond the height level of the film.⁶³

Measuring procedure

Each porous glass disc must only be used for one sample mixture as charged molecules adsorb irreversibly to the glass surface. Before the experiment the porous glass disc was flushed with ethanol and water for several times. Furthermore, the porous glass disc was boiled for 4 h in water. Afterwards, it was dried in a nitrogen stream, rinsed 5 times with the respective sample solution and immersed for at least 2 h in the sample solution for equilibration. Then, it was pulled out and left for surface equilibration for 2 h. All measurements were performed at 25 °C.

Determination of foam film thickness

The disjoining pressure isotherms were obtained by varying the pressure applied to the foam film, while interferometrically measuring its thickness h .^{63,143} The film is illuminated with white light and the intensity of the reflected light is recorded. The light is reflected at the upper and the lower film interface and the two waves interfere with a phase difference that can be correlated to the film thickness. This interferometric method¹⁴³ scales the intensity of the interfered light with the interference minimum $I_{int\ min}$ and maximum $I_{int\ max}$. Hence, the film thickness h is calculated according to the following equation:

$$h = \frac{\lambda}{2\pi\eta_s} \arcsin \sqrt{\frac{\Delta}{1 + (4R(1 - \Delta)/(1 - R)^2)}} \quad (4.6)$$

with

$$\Delta = \frac{I - I_{int\ min}}{I_{int\ max} - I_{int\ min}} \quad (4.7)$$

and

$$R = \frac{(n_s - 1)^2}{(n_s + 1)^2} \quad (4.8)$$

where λ is the wave length of the used interference filter ($\lambda = 550$ nm), n_s the refractive index of the sample solution ($n_s = 1.33$) and I the measured current light intensity. $I_{int\ max}$ and $I_{int\ min}$ are determined during film formation and after film rupture, respectively. At the brightest intensity $I_{int\ max}$, the foam film has a thickness of around 103 nm. With

decreasing film thickness, the film gets darker due to the increasing destructive interference between the two reflected light waves. The equilibrium foam film thickness was measured after the intensity of the reflected light was constant for 10 min. All disjoining pressure isotherms shown within this study were averaged from at least three single measurements.

Simulation of the disjoining pressure isotherms

The measured disjoining pressure isotherms were fitted with a first order exponential decay function. From this fit, the Debye length and the corresponding ionic strength were calculated.⁶³ The results were used as a starting point for model calculations of the non-linear Poisson-Boltzmann (PB) equation. These calculations were performed and compared to the measured isotherms in order to determine the surface potential Ψ_0 . The Poisson-Boltzmann equation describes the ion distribution in an electrolyte solution outside a charged interface:

$$\epsilon_r \epsilon_0 \nabla^2 \Psi = -e \sum_i z_i c_i \quad (4.9)$$

with

$$c_i = c_{i,bulk} \exp(-e z_i \Psi / kT) \quad (4.10)$$

where ϵ_r is the dielectric constant of water, ϵ_0 vacuums dielectric constant, ∇ the Laplace operator, Ψ_0 the surface potential and z_i the ion valency. The PB-software by Per Linse¹⁴⁴ is able to simulate the non-linear Poisson-Boltzmann (PB) equation.^{144,145} It determines the ion profile between two planar surfaces for 50 different distances in a regime between 0 and 100 nm under the assumption of constant potential. The numerical approach in the program considers two planar surfaces having a surface potential Ψ_0 which are separated by the distance D . The intervening liquid is in equilibrium with a bulk electrolyte solution. The software simplifies the system to a half box model, as the film is symmetric. To obtain a unique solution, two boundary conditions need to be fulfilled. At first the electrical field has to vanish at the mid plane of the foam film.

$$\left. \frac{d\Psi(z)}{dz} \right|_{z=b} = 0 \quad (4.11)$$

Secondly electroneutrality must have been established. Therefore, the total charge of the counterions between the two surfaces must equal the charge at the surface.

$$\left. \frac{d\Psi(z)}{dz} \right|_{z=0} = -\frac{\sigma}{\epsilon_0\epsilon_r} \quad (4.12)$$

4.3 Neutron reflectometry (NR)

Basic principles and setup

Neutron reflectometry (NR) measurements were performed on the neutron reflectometer FIGARO at the Institut Laue-Langevin (Grenoble, France).¹⁴⁶ FIGARO is an acronym for **F**luid **I**nterfaces **G**racing **A**ngles **R**eflect**O**meter. Here, isotopic contrast variation is used to determine the structure and composition of surface layers, which consisted of polyelectrolyte/surfactant mixtures in the current thesis. This time-of-flight instrument was used with a chopper pair giving neutron pulses with 4.0 % $d\lambda/\lambda$ in the wavelength range $\lambda = 2 - 30 \text{ \AA}$. Data acquisitions were carried out at incident angles of $\theta = 0.62$ and 3.8° . Samples were equilibrated until they reached steady state prior to each measurement. Specular neutron reflectivity profiles comprise the intensity ratio of neutrons in the specular reflection to those in the incident beam with respect to the momentum transfer Q , defined by

$$Q = \frac{4\pi \sin\theta}{\lambda} \quad (4.13)$$

here θ is the incident angle.²³ To resolve the surface composition and thus the surface excess Γ of polyelectrolytes and surfactants, NR experiments of two different isotopic contrasts of the polyelectrolyte/surfactant mixtures were performed: polyelectrolyte/dC₁₄TAB in air contrast matched water (ACMW) and polyelectrolyte/air-contrast-matched surfactant (cmC₁₄TAB) in ACMW. The reflectivity profiles were fitted with the Motofit software.¹⁴⁷ The calculations are based on the interaction of neutrons with a stratified layer model on the basis of the Abeles matrix method.

Sample preparation and measurement procedure

Mixtures of C_{14} TAB with sPSO₂-220 (chapter 6) or PSS (chapter 7) were investigated with NR. The results were compared to former measurements of PAMPS/ C_{14} TAB mixtures.⁷¹ The samples were made in the isotopic contrasts polyelectrolyte/cm C_{14} TAB/ACMW and polyelectrolyte/d C_{14} TAB/ACMW.^{50,52,71}

Air contrast matched water (ACMW) contains 8.9 % D₂O in 9.1 % H₂O and has a scattering length density (SLD) of 0 corresponding to the SLD of air. Both samples with d C_{14} TAB and air contrast matched surfactant (cm C_{14} TAB) were prepared. For the samples with cm C_{14} TAB, h C_{14} TAB was mixed with d C_{14} TAB in a 95.6 : 4.4 ratio, giving a scattering length density also matched to air. Recently, additional experiments with two more contrasts were prepared and performed: polyelectrolyte/d C_{14} TAB/D₂O and polyelectrolyte/h C_{14} TAB/D₂O. All prepared samples showed no turbidity or precipitation and remained stable for several weeks.

Data evaluation of neutron reflectometry experiments

Firstly, mixtures of the respective polyelectrolyte with deuterated C_{14} TAB in ACMW are measured. Here, the contribution of the solvent to the specular reflection is negligible and the signal arises mainly from scattering by the deuterated C_{14} TAB in the surface monolayer. Adsorbed polyelectrolyte also contributes to the reflected signal. However, in comparison to the signal of d C_{14} TAB, its contribution is rather small. This small contribution is due the rather lower scattering length density of the polyelectrolytes in comparison to the deuterated surfactant. Secondly, for direct investigation of polyelectrolyte adsorption at the air/water interface, NR measurements are carried out with mixtures of the polyelectrolyte and air-contrast-matched surfactant (cm C_{14} TAB) in ACMW. This approach exploits the high flux at the natural low incidence angle of the FIGARO reflectometer to separate the signal from adsorbed hydrogenous polymer from the background.^{50,52,146} To conclude, the signal in the polyelectrolyte/cm C_{14} TAB/ACMW contrast is sensitive only to adsorbed polyelectrolyte, while the signal in the polyelectrolyte/d C_{14} TAB/ACMW contrast is sensitive both to the polyelectrolyte (small contribution to the signal) and d C_{14} TAB (large contribution to the signal).^{50,52,71} As shown in equation 4.14 and 4.15 by subtracting the measured signal of the polyelectrolyte/cm C_{14} TAB/ACMW contrast from the polyelectrolyte/d C_{14} TAB/ACMW contrast one can extract the contribution exclusively caused by surfactant adsorption.

$$(\rho d)_1 = N_A b_{polyelectrolyte} \Gamma_{polyelectrolyte} \quad (4.14)$$

$$(\rho d)_2 = N_A (b_{polyelectrolyte} \Gamma_{polyelectrolyte} + b_{dC_{14}TAB} \Gamma_{dC_{14}TAB}) \quad (4.15)$$

Thus, $\Gamma_{C_{14}TAB}$ corresponds to the surface excess of *C₁₄TAB molecules* and $\Gamma_{polyelectrolyte}$ corresponds to the surface excess of *polyelectrolyte monomer units*. The background, which was determined from a pure ACMW measurements, was subtracted from the reflectivity profiles before analysis. Hence, any enhanced scattering from the measurements of the polyelectrolyte/*C₁₄TAB* mixtures could be attributed to the adsorption of polyelectrolyte and/or *C₁₄TAB*. The SLDs used in the evaluation of the NR data are calculated with the SLD calculator of the Motofit software.¹⁴⁷ The scattering length (SL) and SLD of *C₁₄TAB*, sPSO₂-220 and PSS can be found in table 4.1.

| | SL [10^{-3} Å] | SLD [10^{-6} Å ⁻²] |
|-----------------------------------|-------------------|-----------------------------------|
| d <i>C₁₄TAB</i> | 2.88 | 5.14 |
| d <i>C₁₄TAB</i> -chain | 2.86 | 7.16 |
| h <i>C₁₄TAB</i> -chain | -0.2 | -0.5 |
| TAB-headgroup | 0.024 | 0.18 |
| sPSO ₂ -220 | 0.62 | 1.7 |
| PSS | 0.51 | 1.098 |

Table 4.1: Scattering length (SL) and scattering length density (SLD) for the data evaluation.

The contrasts polyelectrolyte/d*C₁₄TAB*/D₂O and polyelectrolyte/h*C₁₄TAB*/D₂O are useful for the investigation of the structure of the adsorbed polyelectrolyte/surfactant layer(s).^{23,71} These very recent experiments were not fully evaluated in the framework of the present thesis. However, some conclusions on the structure of the adsorbed sPSO₂-220/*C₁₄TAB* layers are shown in chapter 6.

4.4 Small angle neutron scattering (SANS)

Small angle neutron scattering (SANS) is an accurate and non-destructive analytical method to determine the shape and the structure of particles in the nm-range. SANS measurements on cellulose nanocrystals (CNC) were carried out at the V4 instrument at the Helmholtz-Zentrum-Berlin (Germany).¹⁴⁸ Samples were placed in quartz cuvettes

(Hellma, Germany) of 2 mm neutron pathway and studied at three detector distances (1.35, 6 and 15.75 m with collimation at 2, 8 and 16 m, respectively). For short and intermediate distances a wavelength of 4 Å was used, while for the long distance a wavelength of 8 Å was used. This configuration of the instrument provides a Q-range of $0.03 \text{ nm}^{-1} \leq Q \leq 6.4 \text{ nm}^{-1}$. The scattering of water was used to correct for the detector efficiency and as a secondary standard bringing the data to absolute scale. To provide a bulk contrast of the samples, H₂O was exchanged against D₂O through a membrane (Slide-A-Lyzer dialysis cassettes 10k MWCO). The residual volume fraction of light water was determined by comparing the incoherent backgrounds of samples to those of D₂O/H₂O mixtures with known composition. The resulting solvent SLD was calculated accordingly for each sample and can be found in the literature.¹³³ Data reduction and fitting of the data was performed with the BerSANS¹⁴⁹ and SASfit software¹⁵⁰, respectively.

4.5 Additional experimental techniques

Furthermore, several additional experimental techniques were used to a minor degree. More information can be found in the respective publications.

Zeta potential

In chapter 6 and 7 a Malvern Zetasizer NanoZ (Malvern Instruments, Germany) instrument was used to measure the zeta potential ζ . The device measures the electrophoretic mobility by performing Laser Doppler Electrophoresis. The zeta potential ζ is related to the electrophoretic mobility and can be calculated by applying the Henry equation.

$$U_E = \frac{2\epsilon\zeta f(ka)}{3\eta} \quad (4.16)$$

ζ is the zeta potential, U_E is the electrophoretic mobility, ϵ is the dielectric constant, η is the viscosity and $f(ka)$ is the Henry function.¹⁵¹ $f(ka)$ is mainly dependent on the polarity of the used solvent. In the present thesis all measurements were performed in aqueous solutions and hence $f(ka)$ was assumed to be 1.5 (according to the Smoluchowski approximation).¹⁵²

Small angle x-Ray scattering (SAXS)

SAXS measurements were performed using a SAXSess mc² system (Anton Paar KG, Graz, Austria), operated at 40 kV and 50 mA, producing Cu K_α radiation with a wavelength of 0.154 nm. The SAXSquant 3.5 (Anton Paar, Austria) software was used to subtract the background and to desmear the data against the beam length profile of the source. The samples were measured in a 1 mm quartz capillary at 25 °C. The peak position Q_{max} , the full width at half maximum δQ and the maximum intensity of the scattering curves I_{max} were determined by using a Lorentz fit as described in the literature.^{16,84}

Static Light Scattering (SLS)

Static light scattering (SLS) measurements were performed on a compact ALV/CGS-3 instrument equipped with a He-Ne laser with a wavelength of $\lambda = 632.8$ nm.^{125,153} Absolute intensities were obtained by subtracting the scattering intensity of the solvent and cuvette from that of the complex solutions. Calibration was performed using toluene as a standard with a Rayleigh ratio of $1.340 \cdot 10^{-5} \text{ cm}^{-1}$ for 25 °C and 632.8 nm.¹⁵⁴ Sample transmissions were measured using a Varian Cary 50 UV-vis spectrophotometer. The molecular weight M_w and radius of gyration R_g were extracted as described in the literature.¹⁵³

Viscosity measurements

In chapter 8 the viscosity of sPSO₂-220 solutions was measured with the commercial Processor Viscosity System PVS1 (Lauda, Germany) using two Micro-Ostwald glass capillary viscometer (Schott, Germany) with a viscometer constant of 0.03 and 0.1 mm²s² respectively. The flow time was detected by two infrared sensors, and the recorded data was analyzed with the respective Lauda software. The experiment was done at 25 °C.

UV-vis spectroscopy

The turbidity of polyelectrolyte/C₁₄TAB solutions was measured with a Varian Cary 50 UV-vis spectrophotometer. The optical density of the samples was determined at 400 nm (OD₄₀₀). Measurements were carried out 5 min after mixing. Since neither the polyelectrolytes nor C₁₄TAB have an adsorption band above 350 nm, increasing OD₄₀₀ values would indicate the presence of larger polyelectrolyte/surfactant aggregates.

Chapter 5

Surface adsorption of sulfonated poly(phenylene sulfone)/C₁₄TAB mixtures and its correlation with foam film stability*

Abstract

Polyelectrolyte/surfactant mixtures of rigid monosulfonated poly(phenylene sulfone) (sPSO₂-220) and tetradecyl trimethylammonium bromide (C₁₄TAB) were investigated by surface tension, surface elasticity and foam film stability measurements. The results were compared to former measurements of polyelectrolyte/surfactant mixtures containing more flexible polyelectrolytes (PAMPS or PSS and C₁₄TAB). This data, for measurements of mixtures containing PAMPS and PSS, was taken from the PhD thesis of Nora Kristen-Hochrein.¹³¹ For all polyelectrolyte/surfactant mixtures an increased surface adsorption in comparison to the pure surfactant was detected. Moreover, sPSO₂-220/C₁₄TAB mixtures showed a much higher surface activity and foam film stability than mixtures with more flexible polyelectrolytes. The results presented give insight into the surface adsorption and foam film formation of rigid polyelectrolyte/surfactant mixtures. Therefore, this study helps to understand the role of polyelectrolyte backbone rigidity in the formation and stabilization of foam films made from polyelectrolyte/surfactant mixtures.

5.1 Introduction

As discussed in chapter 2.2.2 polyelectrolyte/surfactant mixtures are important for a wide range of applications and were hence extensively investigated.^{1-3,5,29,30} Furthermore, the influence of a wide range of parameters on adsorption and foam film stability were systematically examined.^{14,15,33,41} However, for most of the investigated polyelectrolyte/surfactant mixtures the polyelectrolyte backbones were quite flexible, e.g. poly(acrylamido methyl propanesulfonate) (PAMPS)¹⁵ and poly(styrene sulfonate) (PSS)¹⁴. Both have an intrinsic persistence length l_i of 1 nm. The difference between the two is that PSS is more hydrophobic while PAMPS is more hydrophilic, which leads to significantly differing adsorption behavior of the resulting polyelectrolyte/surfactant complexes.^{14,15,36}

*Similar content was presented in M. Uhlig, R. Miller, and R. von Klitzing, *PCCP*, **2016**, *18*, 18414 - 18423.

Only very little work has been done to investigate the influence of a more rigid polyelectrolyte backbone on the surface adsorption and foam film properties of polyelectrolyte/surfactant mixtures (as discussed in chapter 2.2.2 and 2.2.3).^{17,18,57} To the author's knowledge no study investigated the influence of polyelectrolyte backbone rigidity on both surface adsorption and foam film properties of polyelectrolyte/surfactant mixtures fundamentally so far.

To overcome this shortcoming, here a monosulfonated poly(phenylene sulfone)(sPSO₂-220) was chosen as it is a stiffer polyelectrolyte. Dissipative particle dynamics (DPD) simulations have shown that the sPSO₂-220's polyelectrolyte backbone is significantly stiffer as for example the polyethylene backbones of PAMPS or PSS^{123,124}. Furthermore, due to the electron withdrawing sulfonyl group (-SO₂-) the sulfonate group is especially acidic for sPSO₂-220, which leads to high dissociation degrees of 54 - 61 %^{126,127}, in comparison to a dissociation degree of 33 - 38 % for PSS or PAMPS^{128,129}.

The aim of this work is to study the influence of the backbone rigidity of the polyelectrolyte in a polyelectrolyte/surfactant mixture on its surface adsorption and foam film properties. The system has been investigated by means of surface tension, surface elasticity and foam film stability measurements. The results are compared with former measurements of more flexible polyelectrolytes mixed with the same surfactant (PAMPS and PSS, experiments conducted by Nora Kristen-Hochrein and shown in her PhD thesis).¹³¹ The three polyelectrolytes sPSO₂-220, PAMPS and PSS have the same charged group. The difference between the two flexible polyelectrolytes, PAMPS and PSS, is that PAMPS is more hydrophilic, while PSS is more hydrophobic.¹⁴ By the comparison of the chosen rigid and flexible polyelectrolytes it is possible to clarify the influence of the polyelectrolyte backbone rigidity.

5.2 Results

5.2.1 Determination of the intrinsic persistence length of sPSO₂-220

Static light scattering (SLS) was used to extract the intrinsic persistence length of sPSO₂-220. Samples at different sPSO₂-220 concentrations in water were analyzed and the extracted M_w and R_g values were used for analysis. Data analysis was performed according to Gettinger et al.¹⁵⁵ using the Kratky-Porod model¹⁵⁶. It treats a polymer as a Gaussian

distribution of statistical Kuhn lengths. In this model, the radius of gyration R_g is expressed as:

$$R_g^2 = \frac{n_k b_k^2}{6} \quad (5.1)$$

where n_k is the number of Kuhn segments and b_k is the length of the Kuhn segment. The persistence length l_p is defined as half the Kuhn length and was calculated by the relation:

$$l_p = \frac{3R_g^2}{L} = \frac{3R_g^2 M_0}{l_0 M} \quad (5.2)$$

here L is the contour length of the polymer, M_0 is the monomer molecular weight, l_0 is the monomer length, and M is the molecular weight of the polymer. The length l_0 of a sPSO₂-220 monomer was estimated to be 0.64 nm. The so calculated total persistence length l_p is the sum of the intrinsic persistence length l_i (resulting from the intrinsic stiffness of the polymer) and the electrostatic persistence length l_e (resulting from the electrostatic repulsion of the polyelectrolyte charges, which stiffen the chain).

$$l_p = l_i + l_e \quad (5.3)$$

The intrinsic persistence length can then be extracted from the total persistence length by using a linear plot on the variation of the total persistence length with $c_{\text{sPSO}_2\text{-220}}^{-0.5}$, as shown in Fig. 5.1.^{157,158}

The extracted intrinsic persistence length l_i of sPSO₂-220 is 20 ± 2 nm, which is significantly higher than the intrinsic persistence length of 1 nm found for PAMPS and PSS.⁵⁷

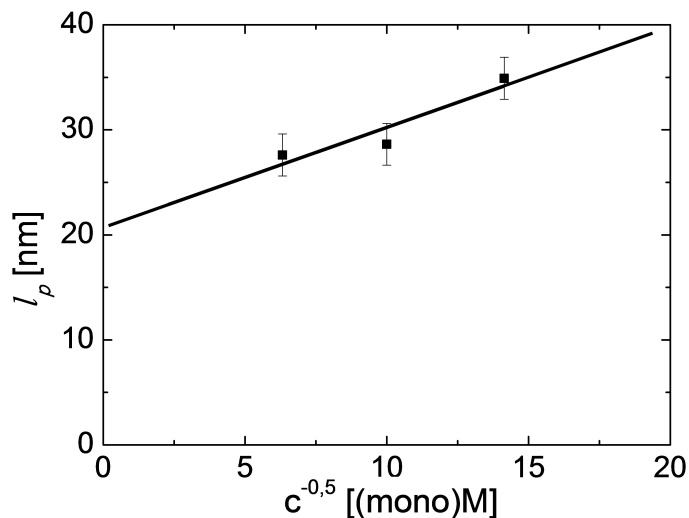


Figure 5.1: Variation of the total persistence length l_p , with $c_{\text{sPSO}_2\text{-220}}^{-0.5}$. The extrapolation of the curve to $c_{\text{sPSO}_2\text{-220}}^{-0.5} \rightarrow 0$ yields the intrinsic persistence length $l_i = 20 \pm 2$ nm.

5.2.2 Characterization of the air/water interface

The focus of this chapter is to investigate the influence of the polyelectrolyte backbone rigidity on the adsorption behavior and foam film stability of oppositely charged polyelectrolyte/surfactant mixtures. Therefore, a mixture of the rigid polyelectrolyte sPSO₂-220 and C₁₄TAB was investigated with different techniques and the results were compared with former measurements using more flexible polyelectrolytes (PAMPS and PSS).^{14,15} At first, the results on the adsorption of sPSO₂-220/C₁₄TAB complexes at the air/water interface are presented. Secondly, the results on foam film stability are shown. In all experiments, the polyelectrolyte concentrations were varied between 10⁻⁵ (mono)M and 3 · 10⁻³ (mono)M, whereas the C₁₄TAB concentration was fixed at 10⁻⁴ M. No turbidity and no precipitation of aggregates was detected, so homogeneous solutions are assumed for all mixtures. All experiments were performed after at least 2 h equilibration time. Longer equilibration time did not affect the adsorption or foam film properties. Hence, it is assumed that the surface coverage is in equilibrium for all measurements.

Surface tension measurements

Fig. 5.2 compares the surface tensions measured for mixtures of C₁₄TAB (at a concentration of 10⁻⁴ M) with different polyelectrolytes (sPSO₂-220, PAMPS¹⁵ and PSS¹⁴, respectively).

With increasing polyelectrolyte concentrations the surface tension isotherms can be divided into three distinctive regimes for all mixtures: polyelectrolyte concentrations below the bulk

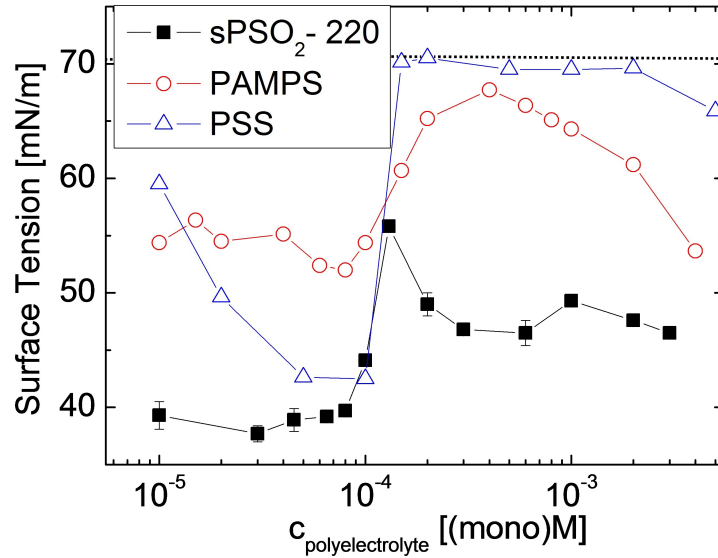


Figure 5.2: Surface tension of sPSO₂-220/C₁₄TAB solutions with fixed C₁₄TAB concentration (10⁻⁴ M) and variable sPSO₂-220 concentration. For comparison the surface tension of the respective PAMPS/C₁₄TAB (from ref. 15) and PSS/C₁₄TAB (from ref. 14) mixtures is added. In this and the following figures the present measurements are plotted with closed symbols, while the former measurements are plotted with open symbols. The dotted line corresponds to the surface tension of pure C₁₄TAB at 10⁻⁴ M.

stoichiometric mixing point (BSMP), around the BSMP (at a polyelectrolyte concentration of 10⁻⁴ (mono)M) and beyond the BSMP. The BSMP is the concentration at which, when assuming complete dissociation, the amount of positive charges from C₁₄TAB and negative charges from sPSO₂-220 is equal in bulk.

At lower polyelectrolyte concentrations, sPSO₂-220/C₁₄TAB mixtures already show a strong decrease in surface tension (around 39 mN/m) in comparison to the pure surfactant (71 mN/m). With increasing sPSO₂-220 concentration the surface tension does not change significantly until the BSMP. In comparison, for PAMPS/C₁₄TAB mixtures the surface tension is constant with increasing polyelectrolyte concentration, with surface tension values of around 55 mN/m.¹⁵ For PSS/C₁₄TAB mixtures the surface tension decreases to around 42.5 mN/m with increasing polyelectrolyte concentration.¹⁴ At and slightly beyond the BSMP the surface tension for sPSO₂-220/C₁₄TAB mixtures increases to slightly higher values (56 mN/m). For PAMPS/C₁₄TAB mixtures a strong increase to the value of pure surfactant was detected, while for PSS/C₁₄TAB mixtures a very steep increase close to the pure surfactant value was found. At polyelectrolyte concentrations beyond the BSMP the surface tension of sPSO₂-220/C₁₄TAB mixtures stays constant around 47.5 mN/m. For PAMPS/C₁₄TAB mixtures the surface tension slightly decreases and for PSS/C₁₄TAB mixtures it stays constant at values close to the pure surfactant value.

Surface elasticity

Investigations of the surface elasticity are useful for this research since they can be used to explain contradictions from surface tension and foam film stability results^{58,70} as discussed in section 5.3.2. The surface elasticities of the three polyelectrolyte/surfactant mixtures are shown in Fig. 5.3.

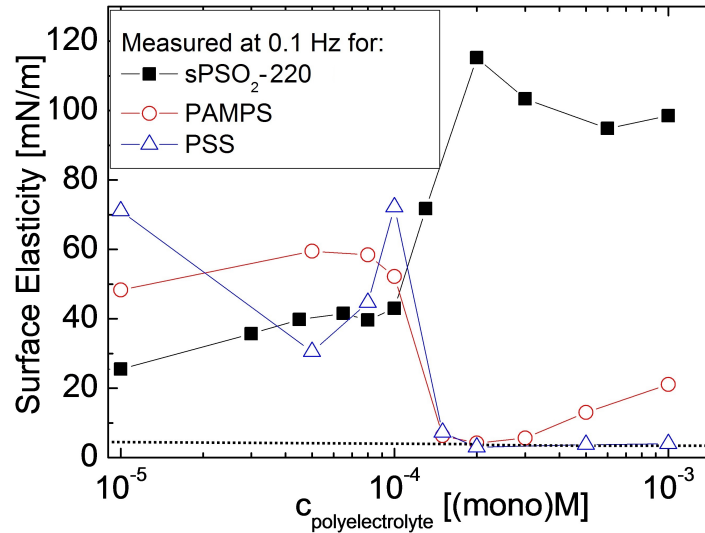


Figure 5.3: Surface elasticity of the sPSO₂-220/C₁₄TAB mixtures in comparison to PAMPS/C₁₄TAB (taken from ref. 15) and PSS/C₁₄TAB mixtures (taken from ref. 14). The colored lines are guidelines to the eyes only. The dotted line corresponds to the surface elasticity of pure C₁₄TAB at 10⁻⁴ M.^{15,69} The error bars of the surface elasticity correspond to the size of the symbols.

The surface elasticity of pure C₁₄TAB is 4 mN/m at the concentration of 10⁻⁴ M^{15,69}. For sPSO₂-220/C₁₄TAB mixtures below the BSMP the surface elasticity rises slowly with increasing sPSO₂-220 concentration. Close to the BSMP a plateau value at around 40 mN/m is reached. At sPSO₂-220 concentrations beyond the BSMP a strong increase in surface elasticity up to 115 mN/m can be observed. At even higher polyelectrolyte concentrations the surface elasticity slightly drops and stays constant at 95 mN/m with increasing concentration. For PAMPS/C₁₄TAB mixtures the surface elasticity is roughly constant around 55 mN/m at polyelectrolyte concentrations lower than the BSMP. Beyond the BSMP it drops to very low surface elasticity values around 5 mN/m. Beyond a PAMPS concentration of $3 \cdot 10^{-4}$ (mono)M the surface elasticity linearly increases with increasing polyelectrolyte concentration.¹⁵ For PSS/C₁₄TAB mixtures the surface elasticity is very discontinuous at polyelectrolyte concentrations below the BSMP. Even at a low polyelectrolyte concentration of 10⁻⁵ (mono)M, the surface is very elastic (around 50 mN/m). With increasing polyelectrolyte concentration the surface elasticity drops to 30 mN/m.

At 10^{-4} (mono)M PSS, which corresponds to the BSMP, the surface elasticity is at its maximum of 72 mN/m. With further increasing PSS concentrations the surface elasticity drops down to very low values of around 3 mN/m and remains constant with increasing PSS concentration.¹⁴

At polyelectrolyte concentrations below the BSMP, sPSO₂-220/C₁₄TAB mixtures show a lower dilatational surface elasticity than the PAMPS/C₁₄TAB and PSS/C₁₄TAB mixtures. At polyelectrolyte concentrations slightly beyond the BSMP the dilatational surface elasticity of the mixtures varies strongly. While for sPSO₂-220/C₁₄TAB mixtures the dilatational surface elasticity increases at concentrations beyond the BSMP, for PAMPS/C₁₄TAB and PSS/C₁₄TAB mixtures it drops to the value of pure C₁₄TAB.

5.2.3 Properties of foam films - disjoining pressure isotherms

TFPB measurements give information about single foam film stabilities, being useful for understanding properties of macroscopic foams. Fig. 5.4 shows disjoining pressure isotherms of sPSO₂-220/C₁₄TAB at different sPSO₂-220 concentrations and fixed C₁₄TAB concentrations (10^{-4} M).

Below the BSMP no stable films but only single values below 300 Pa of the disjoining pressures could be recorded for a certain concentration. With increasing sPSO₂-220 concentration foam film stability decreases and at a concentration around $7 \cdot 10^{-5}$ (mono)M sPSO₂-220 a point of destabilization is reached, where no stable foam film can be recorded at all. At the BSMP and beyond disjoining pressure isotherms could be measured. With increasing sPSO₂-220 concentration both the foam film stability and the steepness of the slope of the disjoining pressure isotherms increases. The steeper slope with increasing sPSO₂-220 concentration is in accordance with increasing ionic strength.

From the slope of the isotherms the Debye length κ^{-1}_{exp} and ionic strength I_{exp} were extracted (Table 5.1).⁶³ The experimentally determined ionic strength I_{exp} is compared in Table 5.1 to the maximum ionic strength $I_{max\ diss}$ and the complex ionic strength $I_{complex}$. $I_{max\ diss}$ is the ionic strength of the system when one assumes complete dissociation, while $I_{complex}$ is the ionic strength of the system assuming complete dissociation and 1:1 binding between polyelectrolytes and surfactants. If the experimental ionic strength I_{exp} value is below the complex ionic strength $I_{complex}$ value dissociation is assumed to be incomplete. If the experimental ionic strength I_{exp} is higher than the complex ionic strength $I_{complex}$ this indicates no 1:1 complexation. To extract further information from the disjoining

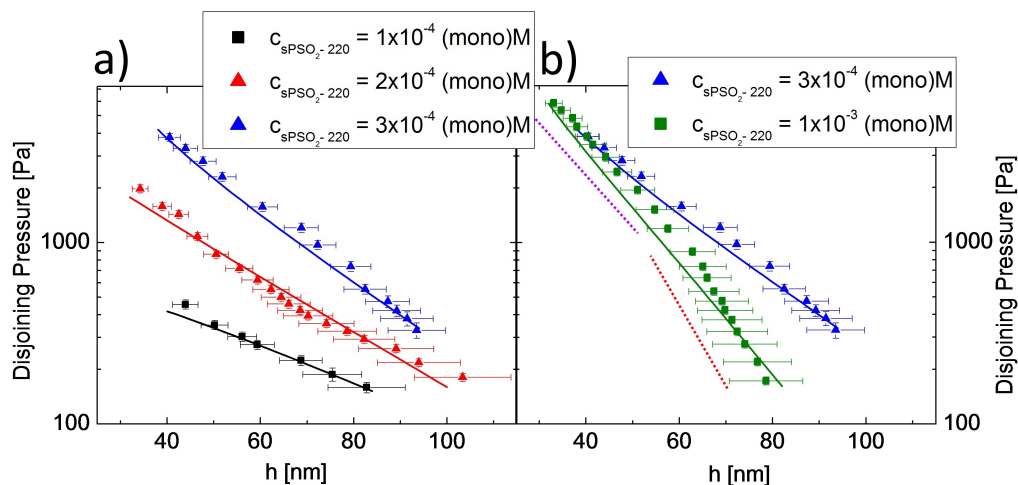


Figure 5.4: Disjoining pressure isotherms of sPSO₂-220/C₁₄TAB solutions with fixed C₁₄TAB concentration (10⁻⁴ M) and variable sPSO₂-220 concentration. The solid lines correspond to simulations at constant potential. In Fig. 5.4a) three isotherms with lower sPSO₂-220 concentrations and a continuous slope are shown. In Fig. 5.4b) a kink occurs in the isotherm which has the highest sPSO₂-220 concentration (10⁻³ (mono)M). Here the solid green line correspond to the simulations over the whole height range of the curve. The dotted lines correspond to the two different slopes of the curve and are shown offset from the data to enhance visibility. For comparison in Fig. 5.4b) an isotherm from Fig. 5.4a) is shown.

pressure isotherms they are simulated with the help of the nonlinear Poisson-Boltzmann equation at constant potential with the PB program version 2.2.1.^{144,145} The results of this simulation and the comparison to former results from PAMPS/C₁₄TAB mixtures¹⁵ are listed in Table 5.1.

For all sPSO₂-220/C₁₄TAB mixtures I_{exp} is smaller than $I_{max\ diss}$ and $I_{complex}$, which shows that the dissociation is not complete. I_{exp} values for sPSO₂-220/C₁₄TAB mixtures are higher than I_{exp} values for PAMPS/C₁₄TAB mixtures, affirming the higher degree of dissociation of sPSO₂-220 in comparison to PAMPS.¹²⁷ In comparison to pure C₁₄TAB, sPSO₂-220/C₁₄TAB mixture shows a reduced surface potential Ψ_0 at polyelectrolyte concentration of $1 \cdot 10^{-4}$ (mono)M (44 vs. 70 mV). For higher sPSO₂-220 concentrations the surface potentials of the sPSO₂-220/C₁₄TAB mixtures increase beyond the surface potential of pure C₁₄TAB and reach values up to 180 mV. In comparison to PAMPS/C₁₄TAB, sPSO₂-220/C₁₄TAB mixtures have a higher surface potential of roughly a factor of 2 at similar polyelectrolyte concentrations.

Interestingly, as shown in Fig. 5.4b), the disjoining pressure isotherm for a sPSO₂-220 concentration of $1 \cdot 10^{-3}$ (mono)M shows a kink. To the author's knowledge such a kink

| c sPSO ₂ -220 [(mono)M] | $ \Psi_0 $ [mV] | κ^{-1}_{exp} [nm] | I_{exp} [M] | $I_{max\ diss}$ [M] | $I_{complex}$ [M] |
|------------------------------------|-----------------|--------------------------|---------------------|---------------------|-------------------|
| $1 \cdot 10^{-4}$ | 44 | 35.9 | $7.2 \cdot 10^{-5}$ | $2 \cdot 10^{-4}$ | $1 \cdot 10^{-4}$ |
| $2 \cdot 10^{-4}$ | 70 | 26.9 | $1.3 \cdot 10^{-4}$ | $3 \cdot 10^{-4}$ | $2 \cdot 10^{-4}$ |
| $3 \cdot 10^{-4}$ | 155 | 22.8 | $1.8 \cdot 10^{-4}$ | $4 \cdot 10^{-4}$ | $3 \cdot 10^{-4}$ |
| $1 \cdot 10^{-3}$ (upper part) | 168 | 15.1 | $4.1 \cdot 10^{-4}$ | $1.1 \cdot 10^{-3}$ | $1 \cdot 10^{-3}$ |
| $1 \cdot 10^{-3}$ (whole isotherm) | 182 | 13.6 | $5.0 \cdot 10^{-4}$ | $1.1 \cdot 10^{-3}$ | $1 \cdot 10^{-3}$ |
| c PAMPS [(mono)M] | $ \Psi_0 $ [mV] | κ^{-1} [nm] | I_{exp} [M] | $I_{max\ diss}$ [M] | $I_{complex}$ [M] |
| $1 \cdot 10^{-5}$ | 52 | 29 | $1.1 \cdot 10^{-4}$ | $1.1 \cdot 10^{-4}$ | $1 \cdot 10^{-4}$ |
| $5 \cdot 10^{-4}$ | 75 | 21.8 | $1.7 \cdot 10^{-4}$ | $6 \cdot 10^{-4}$ | $5 \cdot 10^{-4}$ |
| $1 \cdot 10^{-3}$ | 83 | 15.9 | $3.7 \cdot 10^{-4}$ | $1.1 \cdot 10^{-3}$ | $1 \cdot 10^{-3}$ |
| pure C ₁₄ TAB [M] | $ \Psi_0 $ [mV] | κ^{-1} [nm] | I_{exp} [M] | $I_{max\ diss}$ [M] | $I_{complex}$ [M] |
| $1 \cdot 10^{-4}$ | 70 | 29.3 | $1 \cdot 10^{-4}$ | $1 \cdot 10^{-4}$ | $1 \cdot 10^{-4}$ |

Table 5.1: Summary of the Poisson-Boltzmann simulations of the disjoining pressure isotherms of sPSO₂-220/C₁₄TAB films: surface potentials Ψ_0 , the Debye length κ^{-1} and the ionic strength I_{exp} (extracted by a exponential fit to the data). For comparison the maximum ionic strength $I_{max\ diss}$ (complete dissociation) and the complex ionic strength $I_{complex}$ (complete dissociation and polyelectrolyte/surfactant complex formation in a 1:1 ratio) are shown. Due to the experimental error of the TFPB an average error of $\pm 10\%$ can be assumed for all parameters. The former results for PAMPS/C₁₄TAB and pure C₁₄TAB are also added.¹⁵

in a disjoining pressure isotherm was only observed once before, for pure C₁₄TAB close to the cmc.⁶⁶ For this isotherm with a sPSO₂-220 concentration of $1 \cdot 10^{-3}$ (mono)M, both the whole isotherm and the upper part of the isotherm were simulated. The steeper lower part of the isotherm could not be simulated, since its slope was beyond the accessible simulation range of the used software.

The disjoining pressure isotherms of PAMPS/C₁₄TAB mixtures can be found in the literature.¹⁵ Note that PSS/C₁₄TAB mixtures did not show any stable foam films¹⁴, which can be contributed to a special destabilizing interaction of the aliphatic chain of longer trimethylammonium bromide surfactants and the benzene ring of PSS.³⁶ For the comparison of the absolute foam film stabilities of both mixtures, their maximum disjoining pressures Π_{max} before foam film rupture are plotted in Fig. 5.5 against the concentration of sPSO₂-220 and PAMPS¹⁵, respectively.

Qualitatively, both curves show a similar trend. Below the point of destabilization (slightly below the BSMP) the films are very unstable and show a decreasing stability with increasing polyelectrolyte concentration. However, for sPSO₂-220/C₁₄TAB mixtures it was only possible to measure stable disjoining pressure isotherms beyond a polyelectrolyte concentration of 10^{-4} (mono)M, while PAMPS/C₁₄TAB mixtures showed a stable foam film

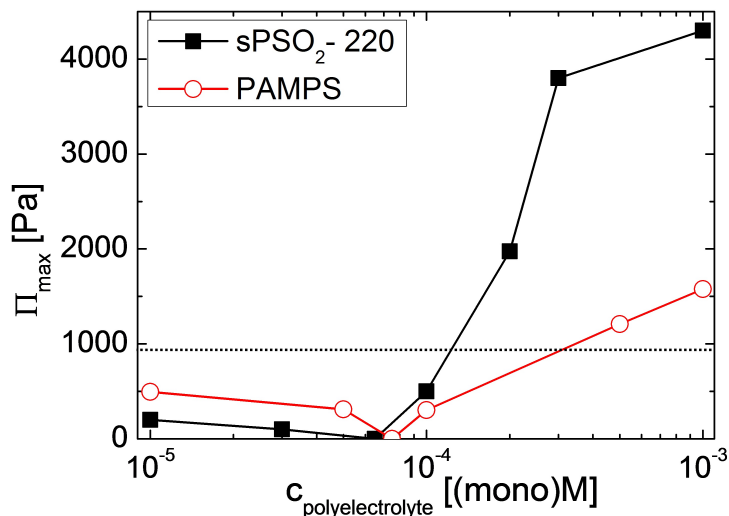


Figure 5.5: The maximum disjoining pressure Π_{max} before film rupture versus respective polyelectrolyte concentration for sPSO₂-220/C₁₄TAB films in comparison to PAMPS/C₁₄TAB films (taken from ref. 15). The error bars correspond to the size of the symbols. The dashed line corresponds to the stability of a pure C₁₄TAB film at 10⁻⁴ M.

already at a polyelectrolyte concentration of 10⁻⁵ (mono)M. At the point of destabilization (around 8 · 10⁻⁵ (mono)M for both sPSO₂-220 and PAMPS) for both mixtures no stable foam film could be formed ($\Pi_{max} = 0$). At and beyond the BSMP stable films can be formed and the film stability increases with increasing polyelectrolyte concentration and rises beyond the stability of pure C₁₄TAB films (around 900 Pa) at higher concentrations of both polyelectrolytes. The PAMPS/C₁₄TAB films are slightly more stable below the point of destabilization, while beyond this point the sPSO₂-220/C₁₄TAB films are significantly more stable.

5.3 Discussion

5.3.1 Adsorption of sPSO₂-220/C₁₄TAB mixtures at the air/water interface

Below the BSMP:

In the studied concentration regime the surface tension is already drastically reduced down to 39 mN/m. With increasing sPSO₂-220 concentration the surface tension stays constant up to the BSMP. In comparison to pure C₁₄TAB (surface tension around 71 mN/m) the sPSO₂-220/C₁₄TAB mixture shows a strongly reduced surface tension. This indicates that additional polyelectrolyte forms species in bulk or remains uncomplexed in the bulk phase.

The synergistic lowering of the surface tension by sPSO₂-220/C₁₄TAB mixtures can be explained by the formation of surface active polyelectrolyte/surfactant complexes.^{8,14,15} The formation of polyelectrolyte/surfactant complexes is energetically favorable due to the decrease in electrostatic repulsion (between positively charged surfactant headgroups at the surface) and the increase in entropy due to the release of counterions.^{42,43}

The surface tension of sPSO₂-220/C₁₄TAB mixtures at sPSO₂-220 concentrations below the BSMP is significantly lower than for PAMPS/C₁₄TAB (55 mN/m) and PSS/C₁₄TAB (60 mN/m) mixtures with similar added amounts of the respective polyelectrolyte. Different reasons could be used to explain this differences in adsorption. The more flexible polyelectrolytes (PAMPS or PSS) might not reduce the surface tension as strongly, as they might coil and thus adsorb less on the surface, forming less dense films.^{14,15} The formation of an especially dense film in case of a rigid polyelectrolyte was also observed in an earlier work.⁵⁷ Here, Stubenrauch et al. compared the surface tension and x-ray reflectivity of PAMPS/C₁₂TAB and PSS/C₁₂TAB mixtures to Xanthan/C₁₂TAB and DNA/C₁₂TAB mixtures with a persistence length of 150 nm and 50 nm, respectively. The Xanthan/C₁₂TAB and DNA/C₁₂TAB mixtures formed a very dense film (strong adsorption at the surface), while PAMPS/C₁₂TAB and PSS/C₁₂TAB mixtures formed a less dense film (weaker adsorption at the surface). Furthermore, earlier publications have shown that the degree of dissociation of sPSO₂-220 is 54 - 61 %¹²⁷ (depending on the measurement technique), which is higher than the degree of dissociation for flexible polyelectrolytes as PAMPS and PSS (around 33 %)^{128,129}. Thus, there are more binding sites for C₁₄TAB at sPSO₂-220 than at PAMPS or at PSS. That leads to a stronger binding of C₁₄TAB to sPSO₂-220 and in turn to more surface active polyelectrolyte/surfactant complexes. Moreover, the charged groups in sPSO₂-220 might be sterically easier accessible. For sPSO₂-220 the charged group is in the polymer backbone, while for PAMPS and PSS it is in the polymer side chain. Due to their backbone flexibility PAMPS and PSS might coil, which would sterically block the charged group and hinder the binding of polyelectrolyte and surfactant. For sPSO₂-220 the charged group is easily accessible due to its position in the polyelectrolyte backbone and due to the backbone rigidity which hinders coiling. A schematic representation of the differences in adsorption of rigid/flexible polyelectrolytes with C₁₄TAB independence of polyelectrolyte concentration is shown in Fig. 5.6.

In the polyelectrolyte concentration regime below the BSMP the surface elasticity of sPSO₂-220/C₁₄TAB mixtures increases from 20 mN/m to 40 mN/m with increasing sPSO₂-220 concentration. Mixtures of PAMPS/C₁₄TAB and PSS/C₁₄TAB show a higher surface elasticity in this concentration regime (50 - 60 mN/m and 30 - 70 mN/m, respectively).

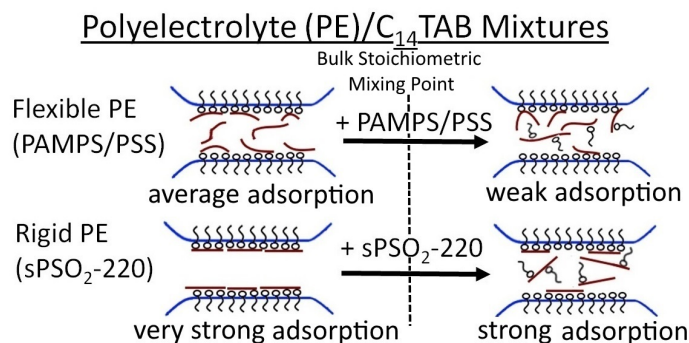


Figure 5.6: Schematic representation of the differences in adsorption of rigid/flexible polyelectrolytes with C₁₄TAB.

As shown in the experimental part the surface elasticity describes how the surface tension reacts on the change of surface area. When surface active compounds move easily from the bulk phase to the surface this results in a low surface elasticity, which results in less stable foam films. When the exchange between the surface and the bulk phase is slow, this results in a high surface elasticity, which in turn results in higher foam stability.^{58,70}

It is surprising that the surface elasticity for the sPSO₂-220/C₁₄TAB mixtures is lower than for PAMPS/C₁₄TAB and PSS/C₁₄TAB mixtures at low polyelectrolyte concentrations. This is in contrast to the lower surface tension for sPSO₂-220/C₁₄TAB in comparison to PAMPS/C₁₄TAB and PSS/C₁₄TAB mixtures in this concentration regime and no simple explanation was found. On the one hand one explanation might be the difference in rotation time for the different polyelectrolytes. When the surface area is changed the polyelectrolytes need time to move and rotate accordingly. In ref. 18 it was shown that the rotation time of a polymer strongly depends on its persistence length. Hence, for flexible polyelectrolytes the system can react faster on the change in area, while for sPSO₂-220 the slow rotation time might slow the reorientation and should thus increase surface elasticity. On the other hand sPSO₂-220/C₁₄TAB adsorbs stronger due to the stronger interaction as discussed earlier, the drag to the surface is stronger, hence resulting in faster exchange and lower surface elasticity values. As the surface elasticity for sPSO₂-220/C₁₄TAB mixtures is lower than for more flexible polyelectrolytes, the stronger interaction seems to be crucial.

At the BSMP:

At and slightly beyond the BSMP sPSO₂-220/C₁₄TAB mixtures show an increase in surface tension. This increase is characteristic for polyelectrolyte/surfactant mixtures and its origin was discussed extensively elsewhere.^{8,48-50} Different explanations can be found in literature explaining this phenomena: the complexes loss of surface activity at chemical

equilibrium^{49,51} and depletion of the surface due to precipitation of complexes in bulk^{50,52}. As mentioned, no precipitation was observed here for sPSO₂-220/C₁₄TAB mixtures. Thus, the latter explanation can be excluded.

An increase in surface tension was also observed for PAMPS/C₁₄TAB and PSS/C₁₄TAB mixtures at and slightly beyond the BSMP.^{14,15} The increase in surface tension is the weakest for sPSO₂-220/C₁₄TAB mixtures, more pronounced for PAMPS/C₁₄TAB mixtures and even stronger for PSS/C₁₄TAB mixtures. The desorption of PSS/C₁₄TAB complexes at PSS concentrations beyond the BSMP can be explained by an increasing hydrophilicity of the complex, since the aliphatic chain of C₁₄TAB may interact with the benzene ring.^{36,55,56} However, sPSO₂-220 has a benzene ring as well and no surface depletion is observed. An explanation might be that due to the higher dissociation degree of sPSO₂-220 more charged binding sites are available for C₁₄TAB, which makes it more attractive for C₁₄TAB to interact via the head group. Furthermore, for PSS the accessibility of the charge for C₁₄TAB might be hindered as discussed earlier. This might lead to a preferred interaction with the benzene ring. The charge in sPSO₂-220 might be easier accessible for C₁₄TAB due to its position in the backbone of the polyelectrolyte.

At the BSMP the surface elasticity of sPSO₂-220/C₁₄TAB mixtures strongly increases. This can be contributed to the fact that sPSO₂-220 is now available in abundance in bulk, while less C₁₄TAB is bound to each sPSO₂-220 chain. That reduces sPSO₂-220's drag to the surface. Thus, as more sPSO₂-220 chains with less drag to the surface collect in bulk, the surface tension increases, while the replacement of chains on the surface is slowed down, leading to a higher surface elasticity. At the BSMP for PAMPS/C₁₄TAB and PSS/C₁₄TAB mixtures the surface elasticity strongly decreases, reaching the value of pure C₁₄TAB. This is in accordance to surface tension measurements which show a strong increase in surface tension in this concentration regime.

Beyond the BSMP:

Beyond the BSMP for sPSO₂-220/C₁₄TAB mixtures the surface tension remains constant at around 47.5 mN/m. Additional sPSO₂-220 does not further reduce the surface tension. This indicates that additional polyelectrolyte does not form surface active species. For PAMPS/C₁₄TAB mixtures at first the surface tension increases with increasing polyelectrolyte concentration, then it decreases again. This is explained by the formation of PAMPS/C₁₄TAB complexes in bulk up to a concentration of $5 \cdot 10^{-4}$ (mono)M PAMPS. Beyond this concentration the PAMPS adsorbs again at the surface.¹⁵ For PSS/C₁₄TAB

mixtures the surface tension stays close to the water value with increasing PSS concentration, which is due to the formation of hydrophilic PSS/C₁₄TAB complexes as mentioned earlier. All isotherms with polyelectrolyte concentrations above 10⁻³ (mono)M show an already low or decreasing surface tension. This can be explained by the strong increase in ionic strength for such high polyelectrolyte concentrations. The high ionic strength leads to a screening of charges at the surface, which in turn leads to a stronger adsorption of both surfactant and polyelectrolyte.⁷¹

At sPSO₂-220 concentrations beyond the BSMP the surface elasticity stays constant at high values with further increasing sPSO₂-220 concentration. This is in accordance with constant surface tension values in this concentration regime. The high surface elasticity shows that in this concentration regime complexes are present both at the surface and in bulk. Beyond the BSMP PAMPS/C₁₄TAB mixtures show a slight increase in surface elasticity which can be explained by the increased amount of adsorbed complexes. This is in accordance to a small decrease in surface tension in this concentration regime. PSS/C₁₄TAB mixtures show a constant surface elasticity close to the value of pure C₁₄TAB beyond the BSMP. This is in accordance to the surface tension measurements, which show little surface adsorption. Both high surface tension and low surface elasticity values can be explained by hydrophilic PSS/C₁₄TAB complexes.

5.3.2 Foam film properties of sPSO₂-220/C₁₄TAB mixtures

Below the BSMP:

At polyelectrolyte concentrations below the BSMP the foam films of sPSO₂-220/C₁₄TAB mixtures are unstable. With increasing sPSO₂-220 concentration foam film stability decreases further and at a concentration around 7 · 10⁻⁵ (mono)M sPSO₂-220 a point of destabilization is reached, where no stable foam film can be recorded at all. In contrast, for all PSS concentrations no stable foam film can be recorded for PSS/C₁₄TAB mixtures.¹⁴ The surface tension and surface elasticity values of PSS/C₁₄TAB mixtures beyond the BSMP indicates that there is almost no adsorption of PSS/C₁₄TAB complexes at the surface. Thus, in this section only results for sPSO₂-220/C₁₄TAB and PAMPS/C₁₄TAB¹⁵ mixtures are discussed. For PAMPS/C₁₄TAB mixtures foam films could be formed which showed a similar trend as sPSO₂-220/C₁₄TAB films: unstable films at low polyelectrolyte concentrations and a point of destabilization slightly below the BSMP.

For low polyelectrolyte concentrations PAMPS/C₁₄TAB mixtures show more stable foam films than sPSO₂-220/C₁₄TAB mixtures. This is counterintuitive to the results of surface tension measurements, which indicate that the adsorption at the air/water interface is stronger for sPSO₂-220/C₁₄TAB than for PAMPS/C₁₄TAB mixtures. On the other hand the surface elasticity of sPSO₂-220/C₁₄TAB is lower than the surface elasticity of PAMPS/C₁₄TAB mixtures. It is known for other systems that the foam film stability increases with increasing surface elasticity.^{58,70}

It is counterintuitive that slightly below the BSMP no stable foam films can be formed for both mixtures, as in both cases surface tension and surface elasticity indicate a strong adsorption at the surface. This can be explained by the fact that for CBFs the film stabilization is not governed by the total adsorbed amount of polyelectrolyte/surfactant complexes, but by the net charge of the surface (as discussed extensively in earlier publications.)^{14,15,71} Thus, for a surface charge close to zero the foam film stability is the lowest. If one assumes that the foam film stability is governed by surface charge one would normally suppose that the point of destabilization is at the BSMP. Different reasons might lead to the shift of the point of destabilization from the BSMP to polyelectrolyte concentrations slightly lower than the BSMP. Firstly, the dissociation degree of C₁₄TAB might be below 100 % in both mixtures, which would shift the BSMP to lower polyelectrolyte concentrations.^{8,15} Secondly, the polyelectrolyte/surfactant mixing ratio at the surface might be different from that in the bulk, leading to a shift of the BSMP.⁸ Thirdly, the pure air/water interface was found to be slightly negatively charged.^{63,67,68} Thus, a part of the positive charges of the surfactant is needed to compensate these charges. Hence, not all surfactant molecules are available to screen the charge of the polyelectrolyte molecules, which leads to shift of the point of destabilization to values slightly lower than the BSMP. At the BSMP sPSO₂-220/C₁₄TAB and PAMPS/C₁₄TAB mixtures form stable foam films.

Beyond the BSMP:

Beyond the BSMP foam film stability of sPSO₂-220/C₁₄TAB mixtures increases strongly with additional sPSO₂-220. PAMPS/C₁₄TAB mixtures beyond the BSMP also show stable foam films. For polyelectrolyte concentrations beyond the BSMP surface tension measurements indicate that less complexes are at the surfaces for both mixtures, than for polyelectrolyte concentrations below the BSMP. This contradiction of increasing foam film stability and increasing surface tension can be contributed to the polyelectrolyte excess in bulk. Earlier publications have shown that not only the polyelectrolyte at the surface, but also that in the film bulk contribute to the stabilization, by increasing the total net charge of the system.^{14,15,71} Hence, increasing polyelectrolyte concentrations lead to increasing

total net charge, which leads in turn to more stable foam films. The influence of the net charge of the system on the surface potential is also discussed later in this section.

While beyond the BSMP the foam film stability of both mixtures increases, foam films of sPSO₂-220/C₁₄TAB mixtures are significantly more stable than their PAMPS/C₁₄TAB counterparts. This stronger increase in foam film stability is in accordance with surface tension measurements. Here, a stronger adsorption of sPSO₂-220/C₁₄TAB than for PAMPS/C₁₄TAB mixtures is observed, which is contributed to the flat and effective adsorption at the air/water interface. Additionally, at concentrations beyond the BSMP, the higher surface elasticity of sPSO₂-220/C₁₄TAB mixtures helps to explain the significantly higher foam film stability of sPSO₂-220/C₁₄TAB in comparison to PAMPS/C₁₄TAB mixtures, since high surface elasticities are known to increase foam film stability.^{58,70}

The Debye length κ^{-1} of sPSO₂-220/C₁₄TAB mixtures was extracted. With increasing sPSO₂-220 concentration the Debye length κ^{-1} decreases as the ionic strength increases. For sPSO₂-220/C₁₄TAB the experimental ionic strength I_{exp} is below the complex ionic strength $I_{complex}$, which shows that the dissociation degree is not 100 %. Former measurements on PAMPS/C₁₄TAB mixture also show a decrease of κ^{-1} with increasing polyelectrolyte concentration.¹⁵ The decrease in Debye length κ^{-1} is stronger for sPSO₂-220/C₁₄TAB than for PAMPS/C₁₄TAB mixtures, as the dissociation degree of sPSO₂-220 is higher.

It is surprising that (as shown in Table 5.1) for a concentration $1 \cdot 10^{-3}$ (mono)M the sPSO₂-220/C₁₄TAB (upper part of the isotherm) and PAMPS/C₁₄TAB mixtures show a similar ionic strength I_{exp} ($4.1 \cdot 10^{-3}$ M vs. $3.7 \cdot 10^{-3}$ M). Due to the higher dissociation degree of sPSO₂-220 one would also expect a higher I_{exp} for that mixture. One possible origin is that the kink in the isotherm (shown in Fig. 5.4 b)) distorts the measurement and the evaluation, resulting in lower values of I_{exp} . Indeed when the whole isotherm is simulated a higher I_{exp} is found (as shown in Table 5.1).

Furthermore, the isotherms were compared to Poisson-Boltzmann model calculations to extract the surface potential Ψ_0 . In comparison to pure C₁₄TAB (at 10^{-4} M) the sPSO₂-220/C₁₄TAB mixture has a reduced surface potential at the BSMP (44 vs. 70 mV). The reason is the reduction of free charges due to binding of C₁₄TAB to sPSO₂-220. However, the surface potential is only reduced by a factor of 1.6 for the sPSO₂-220/C₁₄TAB mixture. That is in accordance with earlier assumptions that the surfactants degree of dissociation is not 100 %, so that the lowest surface potential is reached at a polyelectrolyte concentration

below 10^{-4} (mono)M.^{14,15} With increasing sPSO₂-220 concentration the surface potential Ψ_0 increases, as the ionic strength and polyelectrolyte surface adsorption increases as well. Former measurements also showed an increasing surface potential Ψ_0 with increasing polyelectrolyte for PAMPS/C₁₄TAB mixtures.¹⁵ However, the surface potentials Ψ_0 are roughly a factor two higher for sPSO₂-220/C₁₄TAB than for PAMPS/C₁₄TAB mixtures. This difference between sPSO₂-220 and PAMPS might be due to two reasons: Firstly, sPSO₂-220 shows a stronger decrease in surface tension than PAMPS, hence either sPSO₂-220 or C₁₄TAB adsorbs stronger at the air/water interface than for a PAMPS/C₁₄TAB mixture. Thus, for sPSO₂-220/C₁₄TAB mixtures more polyelectrolyte and hence more charges might be adsorbed at the air/water interface as for PAMPS/C₁₄TAB mixtures. However, surface composition can not be investigated with the techniques used here. Therefore, the composition, the homogeneity and the structure of the film is investigated in a chapter 6 using neutron reflectometry (NR). Secondly, the higher dissociation degree of sPSO₂-220 as of PAMPS¹²⁷, leads to higher ionic strength, which in turn leads to higher surface potentials. The difference in surface potential Ψ_0 also helps to explain the higher foam film stability of sPSO₂-220/C₁₄TAB mixtures in comparison to PAMPS/C₁₄TAB mixtures, as higher surface potential leads to more stable foam films.^{14,15,71}

For a sPSO₂-220 concentration of 10^{-3} (mono)M a kink in the disjoining pressure isotherm was recorded (as shown in Fig. 5.4). This is a rather unusual feature of a disjoining pressure isotherm. To the authors knowledge this was only observed in one other publication, where this phenomena was however not discussed.⁶⁶ Here, pure C₁₄TAB was investigated at a concentration of $3.5 \cdot 10^{-3}$ M. Both the isotherm found here and the one from the literature share that the total ionic strength of the system is relatively large (concentrations beyond 10^{-3} M) and that the kink in the isotherm is close to 1000 Pa. This kink might be a result of charge regulation. This phenomena describes the variation of the surface charge with the separation distance for overlapping double layers.¹⁵⁹ In this work the decrease of separation distance could lead to an expulsion of ions from the bulk phase to the film surface. This would result in a lower ionic strength and a longer Debye length κ^{-1} in bulk and a lower surface potential Ψ_0 at the surface. For the evaluation of this isotherm with a kink both the complete isotherm and just the upper part of the isotherm was used. The difference between both results is rather small. An increase in Debye length κ^{-1} is observed as the slope of the upper part of the isotherm is less steep. Furthermore, the surface potential Ψ_0 does only marginally increase from a sPSO₂-220 concentration of $3 \cdot 10^{-4}$ (mono)M to a concentration of 10^{-3} (mono)M. Hence, the isotherms confirm that charge regulations play a major role in this system. For PAMPS/C₁₄TAB mixtures at a polyelectrolyte concentration of 10^{-3} (mono)M no kink was observed.¹⁵ This can be

explained by the higher ionic strength of sPSO₂-220/C₁₄TAB than of PAMPS/C₁₄TAB mixtures, as a certain amount of charges are needed for the occurrence of the charge regulation phenomena. Charge regulation was extensively investigated with atomic force microscopy (AFM)^{159–161}, but to the authors knowledge not yet with TFPB. The kink in the disjoining pressure isotherm and the prerequisites for its appearance merits further investigations.

5.4 Conclusion

The surface tension experiments in this chapter show that sPSO₂-220/C₁₄TAB mixtures adsorb stronger at the air-water interface than mixtures of more flexible polyelectrolytes (PAMPS or PSS with C₁₄TAB). sPSO₂-220/C₁₄TAB mixtures show a lower surface tension below and beyond the BSMP in comparison to mixtures of PAMPS or PSS with C₁₄TAB. The stronger adsorption is explained by the increase in polyelectrolyte backbone rigidity for sPSO₂-220, which can lead to flat and effective adsorption at the surface. Furthermore, the higher dissociation degree of sPSO₂-220 in comparison to PAMPS or PSS increases binding with the surfactant, and thus enhances surface adsorption. Hence, more complexes adsorb in a denser film at the surface in comparison to more flexible polyelectrolytes as PAMPS or PSS, which can form loops when adsorbing at the surface.

However, the stronger adsorption does not lead to more stable foam films below the BSMP. On the contrary, more stable foam films are recorded for PAMPS/C₁₄TAB than for sPSO₂-220/C₁₄TAB mixtures below the BSMP. This can be contributed to the comparatively low surface elasticity of sPSO₂-220/C₁₄TAB in comparison to PAMPS/C₁₄TAB mixtures. Beyond the BSMP, strong adsorption of sPSO₂-220/C₁₄TAB complexes lead to significantly more stable foam films than for PAMPS/C₁₄TAB mixtures. This can be explained by the lower surface tension and the higher surface elasticity for sPSO₂-220/C₁₄TAB mixtures in comparison to PAMPS/C₁₄TAB mixtures. Furthermore, surface potentials, which are decisive for stabilization of CBFs, are higher by a factor of 2 for sPSO₂-220/C₁₄TAB than for PAMPS/C₁₄TAB mixtures. That confirms a high degree of dissociation for sPSO₂-220 and leads to the high foam film stability and smaller Debye lengths of sPSO₂-220/C₁₄TAB mixtures.

Chapter 6

Surface composition and the correlation to foam film stability of sPSO₂-220/C₁₄TAB mixtures

Abstract

In chapter 5 sPSO₂-220/C₁₄TAB mixtures have shown a strong synergistic surface adsorption, which lead to more stable foam films than for PAMPS/C₁₄TAB mixtures. However, the exact surface composition and its relation to foam film stability is still unclear. In this chapter neutron reflectometry (NR) was used to investigate the composition of the adsorbed sPSO₂-220/C₁₄TAB layer(s). The results are correlated to the corresponding foam film stabilities for varying polyelectrolyte/surfactant ratios. It is shown that a high surface excess does not lead to stable foam films, while for intermediate surface excesses and high ionic strength very stable foam films form. Thus, a new framework for foam film stability in terms of the interfacial composition *and* structure is presented. On the one hand foam films are very *stable* for intermediate surface excesses, at 1:1 polyelectrolyte/surfactant ratios and when highly charged complexes form in the subsurface/bulk. These complexes may not only influence the surface charge, but also induce electrostatic repulsion between the respective subsurface regions. On the other hand, foam films are very *unstable* when they contain thick and extended multilayers, which might attract each other and hence destabilize the foam film.

6.1 Introduction

As mentioned oppositely charged polyelectrolyte/surfactant mixtures are common in a wide range of applications.^{1,3,30} The surfactant adsorbs at the interface due the hydrophobic effect and the polyelectrolyte binds to the surfactant via electrostatic interactions and because of the gain in entropy due to counterion release.^{42,43} The adsorption of polyelectrolyte/surfactant mixtures at the air water interface is typically investigated by surface tension measurements.^{22,27} The synergistic nature of the interaction results in the fact that less material is needed to create a low surface tension than with ordinary surfactant mixtures.^{7,22} One reason for the synergistically enhanced adsorption of the mixture is the screening of electrostatic repulsion between the surfactant molecules due to the presence of polyelectrolytes.^{22,42}

To understand the correlation of surface adsorption and foam film stability of polyelectrolyte/surfactant mixtures, PAMPS/ C_{14} TAB mixtures were investigated.¹⁵ Within that work no simple relationship between surface adsorption and foam film stability was found for this system. Especially close to the bulk stoichiometric mixing point (BSMP) surface tension and surface elasticity experiments showed a strong adsorption of surface active complexes, though it was not possible to form stable foams at this concentration.^{14,15} The foam film stability for this system was explained by the repulsions of the foam films surface charges. It was assumed that a high surface charge leads to high repulsion and hence stable films, while a low amount or zero surface charge leads to foam film instability. As close to the BSMP the amount of negative and positive charges is similar, the resulting surface charge was assumed to be small, leading to foam film instability.⁸

One problem is that with the thin film pressure balance (TFPB) technique the surface charge is only accessible when a stable foam film can be formed. Hence, this assumption could not be verified yet, as also polyelectrolyte/surfactant ratios which do not form stable foams may have a high surface charge. For a deeper insight into the PAMPS/ C_{14} TAB mixture the interfacial composition was investigated with NR using isotropic contrast variation.⁷¹ Compositional information help to elucidate the adsorption mechanisms of polyelectrolyte/surfactant mixtures^{22,24,71} and are useful to understand and verify models of surfactant mixing¹⁶². For PAMPS/ C_{14} TAB mixtures it was shown that the most stable foam film forms for enhanced synergistic adsorption of both components.⁷¹ Furthermore, it was shown that polyelectrolyte/surfactant complexes in bulk play a decisive role in foam film stabilization, as they can influence the charge of the foam films surface.⁷¹ Still, it was not possible to explain foam film stability for all PAMPS/ C_{14} TAB ratios and it was not clear if the findings for this particular mixture can be generalized for all polyelectrolyte/surfactant mixtures.

The purpose of the present chapter is to relate the foam film stability to the interfacial composition and structure for sPSO₂-220/ C_{14} TAB mixtures. This mixture was chosen because it forms very stable foam films for certain polyelectrolyte/surfactant ratios (as shown in chapter 5).¹²⁵ The strong surface adsorption and the formation of especially stable foam films of this mixture were explained by the rigid conformation and high dissociation degree of sPSO₂-220.¹²⁵

6.2 Results

6.2.1 Bulk interaction of sPSO₂-220 and C₁₄TAB

All sPSO₂-220/C₁₄TAB mixtures investigated are transparent to the naked eye. For the highest sPSO₂-220 concentration the solutions become very slightly brownish, as sPSO₂-220 has a brownish color. The fact that no particles large enough to scatter light were observed by eye, implies that the complexes present in solution have sufficient charge to retain colloidal stability. To examine the charge on the sPSO₂-220/C₁₄TAB complexes, zeta potential measurements were performed. For comparison with former data,^{71,125} the surfactant concentration is fixed at 10⁻⁴ M, while the sPSO₂-220 concentration is varied between 10⁻⁵ and 3 · 10⁻³ (mono)M. Furthermore, turbidity measurements were performed with an UV-Vis spectrophotometer. The optical density of the samples was determined at 400 nm (OD₄₀₀). Since neither sPSO₂-220 nor C₁₄TAB have an adsorption band above 350 nm, increasing OD₄₀₀ values would indicate the presence of larger polyelectrolyte/surfactant aggregates. The results of both measurements is shown in Fig. 6.1.

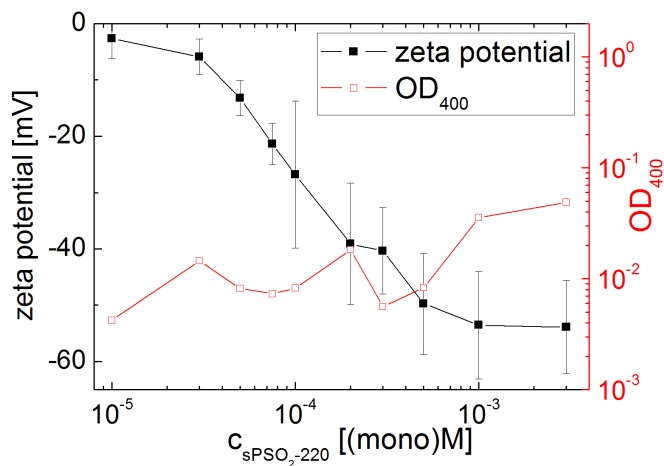


Figure 6.1: Zeta potential ζ and OD₄₀₀ values of the investigated sPSO₂-220/C₁₄TAB mixtures. The C₁₄TAB concentration is fixed at 10⁻⁴ M, while the sPSO₂-220 concentration is varied. The error bars for the zeta potential values correspond to the intrinsic experimental error of the instrument. The error for the OD₄₀₀ values is within the size of the symbols.

No charge reversal from positive to negative can be observed as the bulk sPSO₂-220 concentration is increased. Instead, a decrease in ζ with increasing sPSO₂-220 concentration is observed. No increase in OD₄₀₀ (turbidity) values was recorded. The slight increase in

OD₄₀₀ values for high sPSO₂-220 concentrations can be contributed to the adsorption due to the increasingly brownish color of the polyelectrolyte solution.

6.2.2 Surface composition of sPSO₂-220/C₁₄TAB mixtures

NR measurements were carried out, to reveal trends in the surface coverage and composition of sPSO₂-220/C₁₄TAB mixtures with respect to the bulk sPSO₂-220 concentration, and to examine the origin of their exceptional foam film stability. Firstly, mixtures of sPSO₂-220 with deuterated surfactant (dC₁₄TAB) in ACMW were measured. Here, the specular reflectivity signal is dominated by scattering from the deuterated surfactant present at the interface. Adsorbed sPSO₂-220 also contributes to the reflected signal but, because it is hydrogenous, it has a relatively low scattering length density and hence its contribution is small. Furthermore, the contribution of the solvent to the specular reflection is negligible. Secondly, NR measurements were carried out with mixtures of sPSO₂-220 and air-contrast-matched surfactant (cmC₁₄TAB) in ACMW. This approach exploits the high flux at the natural low incidence angle of the FIGARO reflectometer to separate the weak signal from adsorbed hydrogenous polymer from the background.^{38,50,52,71} Fig. 6.2 a) and 6.2 b) show examples of neutron reflectivity profiles for sPSO₂-220/dC₁₄TAB mixtures in ACMW with varying polyelectrolyte concentrations together with the model fits, while Fig. 6.2 c) and 6.2 d) show equivalent plots for the sPSO₂-220/cmC₁₄TAB solutions.

The highest reflectivities in both isotopic contrasts (implying maximum surface excesses of both components) are observed at intermediate bulk sPSO₂-220 concentrations close to the BSMP. For lower and higher sPSO₂-220 concentrations lower reflectivities in both isotopic contrasts were recorded. To comment in detail on the trends, the two measured scattering excesses for each equivalent sample were converted into the surface excess of each component using the method described in the experimental section 4.3 and in the literature.^{50,52,71} Hence, in this chapter and in chapter 7, $\Gamma_{C_{14}TAB}$ corresponds to the surface excess of *C₁₄TAB molecules* and $\Gamma_{polyelectrolyte}$ corresponds to the surface excess of *polyelectrolyte monomer units*.

Fig. 6.3 shows the surface excesses of the two components and the resulting surface excess of charges $\Gamma_{+/-}$ with respect to the bulk sPSO₂-220 concentration. $\Gamma_{+/-}$ is calculated as follows:

$$|\Gamma_{+/-}| = \Gamma_{C_{14}TAB} - \Gamma_{sPSO_2-220} \quad (6.1)$$

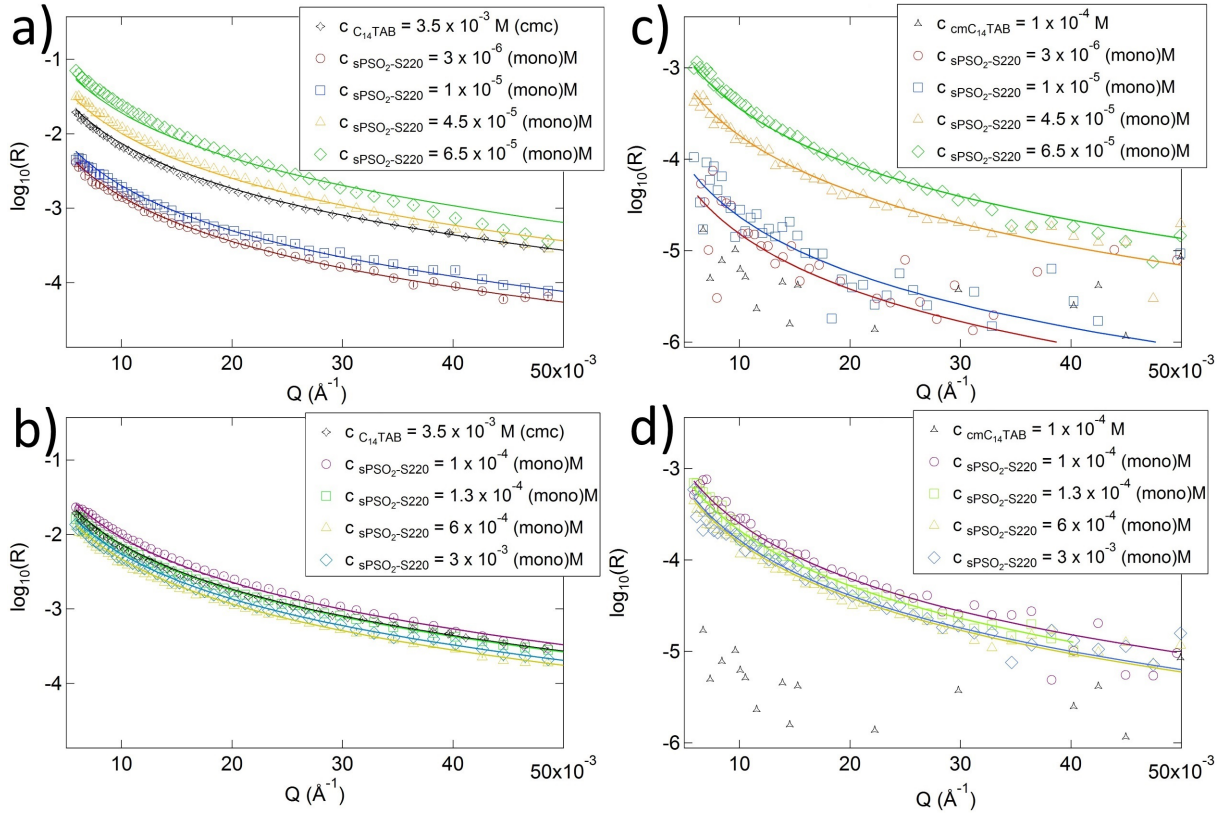


Figure 6.2: Neutron reflectivity profiles for solutions prepared in ACMW from sPSO₂-220/dC₁₄TAB mixtures (a) and (b) and sPSO₂-220/cmC₁₄TAB mixtures (c) and (d). The sPSO₂-220 concentration is varied, while the bulk surfactant concentration is fixed at 10^{-4} M . The solid lines correspond to model fits. For comparison in (a) and (b) a reflectivity profile for dC₁₄TAB at the critical micelle concentration (cmc) is shown and in (c) and (d) the reflectivity profile for cmC₁₄TAB at 10^{-4} M is shown.^{71,163} For enhanced clarity, not all recorded NR profiles are shown. Additional NR profiles can be found in the Appendix (Fig. 11.1 and 11.2).

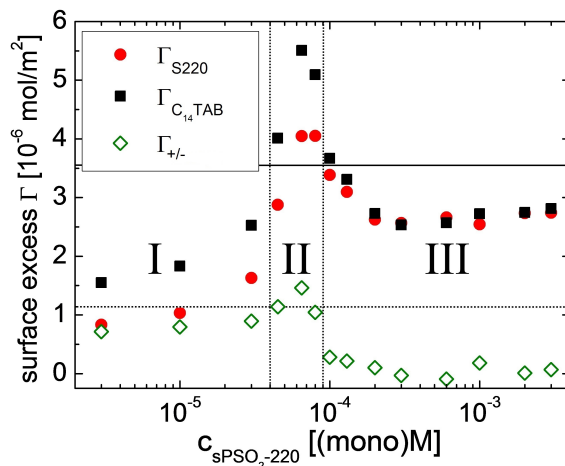


Figure 6.3: Surface excesses of sPSO₂-220 ($\Gamma_{\text{sPSO}_2\text{-220}}$) and C₁₄TAB ($\Gamma_{\text{C}_{14}\text{TAB}}$) in their mixtures in dependence of sPSO₂-220 concentration derived from the NR measurements. Furthermore, the surface excess of charges $\Gamma_{+/-}$ was added. For all mixtures the concentration of C₁₄TAB is fixed at 10⁻⁴ M. The error bars correspond to the size of the symbols. The dotted line corresponds to the surface excess of a pure C₁₄TAB solution at a concentration of 10⁻⁴ M.⁷¹ The solid black line corresponds to the surface excess of a pure C₁₄TAB solution at the cmc ($3.5 \cdot 10^{-3}$ M).¹⁶³ The vertical dotted line correspond to three distinctive concentration regimes.

When complete dissociation is assumed $\Gamma_{+/-}$ is proportional to the surface charge and can hence be used as a measure of the surface charges induced by the surface composition. Similar trends are observed for both the polyelectrolyte and surfactant. Already at the lowest measured bulk sPSO₂-220 concentration, there is an enhanced surface adsorption of C₁₄TAB in the mixture compared to the pure surfactant solution (in the absence of polyelectrolyte).⁸ Furthermore, adsorbed sPSO₂-220 is also detected. With increasing sPSO₂-220 concentration, the amount of both components at the interface increases, with maximum values found at bulk sPSO₂-220 concentrations in the range $6.5 \cdot 10^{-5}$ - $8 \cdot 10^{-5}$ (mono)M. Still at higher bulk sPSO₂-220 concentrations, the surface excesses decrease until they become approximately constant above bulk sPSO₂-220 concentrations of $2 \cdot 10^{-4}$ (mono)M.

6.2.3 Preliminary insight into the structure of sPSO₂-220/C₁₄TAB mixtures at the air/water interface

As mentioned in the experimental section 4.3, in addition to the contrasts in ACMW, also two contrasts in D₂O were measured for the extended Q range of 0.25 Å⁻¹: sPSO₂-

220/dC₁₄TAB/D₂O and sPSO₂-220/hC₁₄TAB/D₂O. By fitting simultaneously these contrasts in D₂O together with the contrast sPSO₂-220/dC₁₄TAB/ACMW it is possible to extract information about the structure of the adsorbed layer(s). This information may include: type, number and sequence of layers, solvent penetration etc. A preliminary evaluation of these data sets for three distinctive sPSO₂-220 concentrations can be found in the appendix (Fig. 11.3 - 11.5). These sPSO₂-220 concentrations ($1 \cdot 10^{-5}$ (mono)M, $8 \cdot 10^{-5}$ (mono)M and $3 \cdot 10^{-3}$ (mono)M) correspond to the three different sPSO₂-220 concentration regimes shown in Fig. 6.5.

6.3 Discussion

6.3.1 Bulk interaction of sPSO₂-220 and C₁₄TAB

A decrease in ζ for sPSO₂-220/C₁₄TAB mixtures with increasing sPSO₂-220 concentration is observed (shown in Fig. 6.1), indicating the formation of more and more negatively charged sPSO₂-220/C₁₄TAB complexes in bulk. This means that even at the lowest measured bulk sPSO₂-220 concentration, the chemical potential of the bulk C₁₄TAB is insufficient to neutralize the bulk complexes. Since no increase in OD₄₀₀ (turbidity) values was recorded (shown in Fig. 6.1) aggregation to macroscopic particles can be ruled out. The data support the empirical observation that the samples investigated in this chapter are all present in the equilibrium one phase region.

6.3.2 Surface composition of sPSO₂-220/C₁₄TAB mixtures

For all investigated samples the surface excess of C₁₄TAB ($\Gamma_{\text{C}_{14}\text{TAB}}$) in the mixture is higher than that of pure C₁₄TAB at the same concentration in the absence of polyelectrolyte (dotted line in Fig. 6.3).⁷¹ This demonstrates the strong synergistic binding of sPSO₂-220 with C₁₄TAB at the interface.⁴² $\Gamma_{\text{C}_{14}\text{TAB}}$ starts at $1.6 \cdot 10^{-6}$ mol/m² at the lowest bulk sPSO₂-220 concentration measured, and with increasing bulk sPSO₂-220 concentration the value reaches a maximum of $5.7 \cdot 10^{-6}$ mol/m² at a value of $6.5 \cdot 10^{-5}$ (mono)M. Note that in the concentration range from $4.5 \cdot 10^{-5}$ to $1 \cdot 10^{-4}$ (mono)M sPSO₂-220, $\Gamma_{\text{C}_{14}\text{TAB}}$ is even higher than the equivalent value at the cmc in absence of polyelectrolyte (solid line in Fig. 6.3).¹⁶³ This finding, that in this concentration range more C₁₄TAB molecules adsorb than C₁₄TAB molecules would adsorb for the cmc, implies the presence of an interfacial structure that is considerably more extended than a surfactant monolayer

with polyelectrolyte bound to the head groups. A similar extended interfacial structure was previously found for poly(sodium styrene sulfonate)/dodecyltrimethylammonium bromide mixtures.^{55,130} The increase in $\Gamma_{C_{14}TAB}$ and Γ_{sPSO_2-220} is due to increasing sPSO₂-220 concentration. The more sPSO₂-220 is in the mixture the more polyelectrolytes and surfactants can synergistically adsorb at the surface. Above a bulk sPSO₂-220 concentration of $8 \cdot 10^{-5}$ (mono)M, $\Gamma_{C_{14}TAB}$ decreases to a value of $2.5 \cdot 10^{-6}$ mol/m² at $2 \cdot 10^{-4}$ (mono)M, where it remains approximately constant until the highest measured bulk sPSO₂-220 concentration.

The polyelectrolyte sPSO₂-220 is not surface active on its own but it shows a strong synergistic adsorption in mixtures with C₁₄TAB. The surface excess of sPSO₂-220 in the mixture (Γ_{sPSO_2-220}) is comparatively low at the lowest measured bulk sPSO₂-220 concentration with $0.6 \cdot 10^{-6}$ mol/m². Γ_{sPSO_2-220} increases with increasing sPSO₂-220 concentration until a maximum of $4.0 \cdot 10^{-6}$ mol/m² is reached at bulk sPSO₂-220 concentrations of $6.5 \cdot 10^{-5}$ and $8 \cdot 10^{-5}$ (mono)M. At higher bulk sPSO₂-220 concentrations, Γ_{sPSO_2-220} decreases until it also reaches $2.5 \cdot 10^{-6}$ mol/m² at $2 \cdot 10^{-4}$ (mono)M and further addition of sPSO₂-220 does not change Γ_{sPSO_2-220} significantly. The depletion of sPSO₂-220/C₁₄TAB complexes from the surface can be contributed to a reduction in surface activity of the polyelectrolyte/surfactant complexes. The results are in accordance with surface tension measurements from chapter 5, which also show a strong synergistic adsorption of sPSO₂-220/C₁₄TAB complexes.¹²⁵ Below the BSMP the surface tension showed low values, indicating a strong adsorption. Beyond the BSMP the surface tension increased, indicating less adsorption.¹²⁵

The findings about the surface composition shown here contain no direct insight on the structure of the adsorbed layers at the surface. However, from the adsorbed amount of the compounds one can draw preliminary conclusions on the structure of the layers. Since for example in concentration regime from $4.5 \cdot 10^{-5}$ to $1 \cdot 10^{-4}$ (mono)M sPSO₂-220 the adsorbed amount of C₁₄TAB is higher than for its cmc¹⁶³ one can conclude that either a very dense layer forms or a multilayer adsorption takes place indicating a very thick or extended layer.

6.3.3 Preliminary insight into the structure of sPSO₂-220/C₁₄TAB mixtures at the air/water interface

By comparing the recorded data in Fig. 11.3 - 11.5 it can be easily seen that the neutron reflectivity profiles in Fig. 11.4 (sPSO₂-220 concentration of $8.5 \cdot 10^{-5}$ (mono)M) show

fringes, while the other profiles do not show fringes. Fringes are an indication for relatively thick and extended single layers or multilayered structures. This is in accordance with the surface composition, which show that for this concentration range a maximum in polyelectrolyte and surfactant adsorption is reached (as shown in Fig. 6.3). Furthermore, a preliminary simultaneous fit of the three isotopic contrasts for each of the three sPSO₂-220 concentrations, corresponding to three distinctive concentration regimes, is conducted.

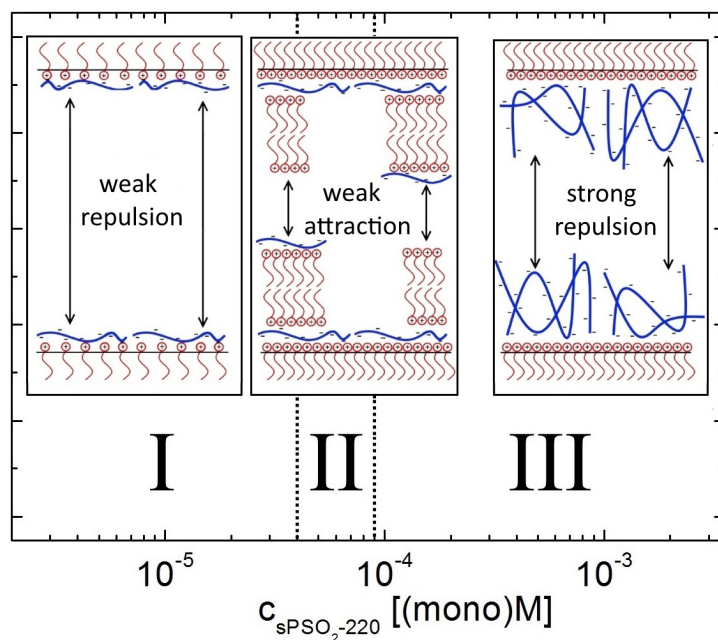


Figure 6.4: Schematic representation of the possible structures of the adsorbed sPSO₂-220/C₁₄TAB layers, according to preliminary fits shown in Fig. 11.3 - 11.5. For all mixtures the concentration of C₁₄TAB is fixed at 10⁻⁴ M. The horizontal dotted lines divide the plots into three concentration regimes corresponding to the regimes in Fig. 6.5. The sketches are shown in the air/water/air arrangement, so that they can be easily correlated to foam film stability discussed in the next section.

For the relatively low sPSO₂-220 concentration of $1 \cdot 10^{-5}$ (mono)M (Fig. 11.3, corresponding to regime **I**) a surfactant layer with a dense (26 % solvent penetration) and small (around 6 Å) polyelectrolyte layer underneath can be found. For the intermediate sPSO₂-220 concentration of $8 \cdot 10^{-5}$ (mono)M (Fig. 11.4, corresponding to regime **II**) a complex structure is detected, which is not completely resolved yet. A surfactant layer with a polyelectrolyte layer underneath can be found (similar to the polyelectrolyte layer in regime **I**). However, beneath this layer patches of a surfactant bilayer can be found. This bilayer has a coverage of 10 - 25 % , while the remaining part is not covered with the bilayer. Furthermore, below this bilayer a thin additional polyelectrolyte layer might be found. For the highest sPSO₂-220 concentration of $3 \cdot 10^{-3}$ (mono)M (Fig. 11.5, corresponding to

regime **III**) a surfactant layer with a very open, solvent rich (92.5 % solvent penetration) but extended (around 79 Å) polyelectrolyte layer underneath is found. As a result from the preliminary fits and the surface composition data (Fig. 6.3) a suggestion for 3 possible structure of adsorbed layers, corresponding to three concentration regimes, is shown in Fig. 6.4.

6.3.4 Correlation of surface composition and foam film stability of sPSO₂-220/C₁₄TAB mixtures

As mentioned in chapter 5, within the investigated sPSO₂-220 concentration range, foam films from sPSO₂-220/C₁₄TAB mixtures were rather thick (30 - 100 nm), homogeneous and discontinuous thinning (stratification) was not observed. Hence, it is assumed that the formed complexes remain in the film bulk and contribute to the film stability.¹²⁵ As also mentioned in section 5.2.3 the maximum disjoining pressure Π_{max} can be taken as a measure of foam stability. The surface potential $|\Psi_0|$ is related to the amount of charges on the surface and hence presumed to be the origin of foam film stabilization. The zeta potential $|\zeta|$ is related to the amount of charges on polyelectrolyte/surfactant complexes in bulk. Γ_{abs} is the sum of $\Gamma_{C_{14}TAB}$ and Γ_{sPSO_2-220} and gives information about the absolute amount of adsorbed material at the surface. To correlate findings from the bulk phase, the air/water interface and foam films, all the mentioned parameters were normed to their respective maximum value and are shown in dependence of sPSO₂-220 concentration in Fig. 6.5.

Furthermore, to facilitate the analysis of the relationship between the surface excesses of both components and the bulk sPSO₂-220 concentration, the interfacial ratio of $\Gamma_{C_{14}TAB}/\Gamma_{sPSO_2-220}$ is also plotted in Fig. 6.5. The interfacial ratio starts at around 2:1 for low bulk sPSO₂-220 concentrations. With increasing bulk sPSO₂-220 concentration the ratio decreases. Close to the BSMP the ratio reaches 1:1. At even higher bulk sPSO₂-220 concentrations, $\Gamma_{C_{14}TAB}/\Gamma_{sPSO_2-220}$ remains constant at a 1:1 ratio. If complete dissociation is assumed a 1:1 ratio of surfactant and polyelectrolyte indicates an uncharged or only slightly (as discussed in section 2.2.1) charged surface. Since $\Gamma_{C_{14}TAB}/\Gamma_{sPSO_2-220}$ remains constant at a 1:1 ratio for higher bulk sPSO₂-220 concentrations excess surfactant at the interface is only present when there is excess surfactant in the bulk. There is no excess polyelectrolyte at the interface in any of the measured samples. For low sPSO₂-220 concentrations an abundance of surfactant molecules are available for interaction with the

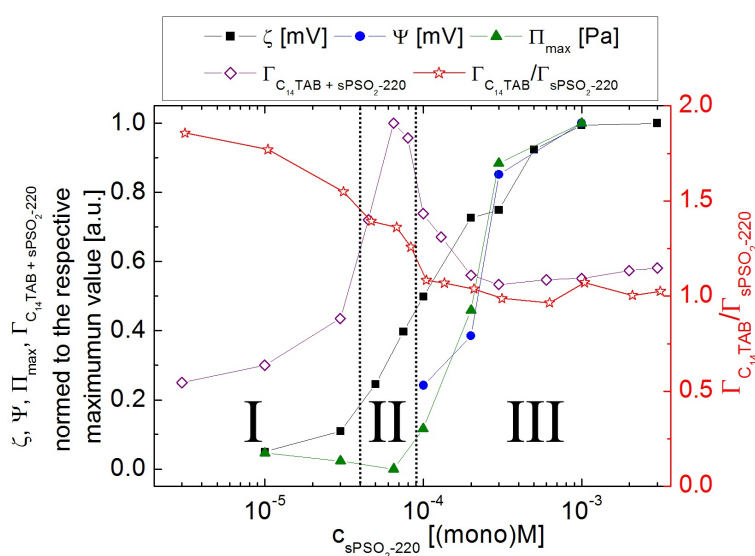


Figure 6.5: $|\zeta|$, $|\Psi_0|$, Π_{max} and Γ_{abs} are shown in dependence of sPSO₂-220 concentration. Furthermore, the surface excess ratio $\Gamma_{C_{14}TAB}/\Gamma_{sPSO_2-220}$ is also shown in dependence of sPSO₂-220 concentration. To show the correlation between $|\zeta|$, $|\Psi_0|$ and Π_{max} these parameters are shown with full symbols, while the data from NR experiments are shown with open symbols. For all mixtures the concentration of C₁₄TAB is fixed at 10⁻⁴ M. For enhanced clarity the error bars of the data is not shown. The horizontal dotted lines divide the plots into three concentration regimes. Π_{max} and $|\Psi_0|$ data shown in the graph are taken from chapter 5.¹²⁵

polyelectrolyte. With increasing polyelectrolyte concentration the abundance of surfactant molecules is reduced, which is reflected in the decreasing surfactant/polyelectrolyte ratio.

As discussed in section 6.1, the foam film (de)stability of polyelectrolyte/surfactant mixtures was so far explained by the total net charge of the surface. Higher net charges were expected to result in more stable foam films.⁸ The foam film stability and surface composition show three different regimes with increasing sPSO₂-220 concentration, which are separately discussed.

In the first regime **I** (sPSO₂-220 concentrations below the BSMP), there is a substantial amount of adsorbed polyelectrolyte and surfactant at the air/water interface. Both surface excesses further increase with increasing sPSO₂-220 concentration. $\Gamma_{C_{14}TAB}$ is higher for the mixture than it is for pure C₁₄TAB. Although surface charges could not be detected via TFPB experiments (due to foam film instability) the surface might be positively charged, as there is excess surfactant at the interface (shown in Fig. 6.3) indicating a positive surface charge. The preliminary structural investigation found a thin but dense polyelectrolyte layer below the surfactant layer (shown in Fig. 6.4). These conditions do not result in stable foam films, as the stability of the mixtures foam films formed for this concentration regime is lower than that of a pure C₁₄TAB foam film at 10⁻⁴ M.^{15,125} With increasing sPSO₂-220 concentration the foam film stability further decreases. In this regime the low foam film stability can be contributed to the decreasing surface charge. As mentioned, due to the excess of C₁₄TAB the surface is presumably positively charged, but due to the increasing adsorption of negatively charged sPSO₂-220 molecules at the surface this charge is reduced, leading to less stable foam films than for pure C₁₄TAB.

In the second regime **II** (sPSO₂-220 concentrations close and slightly below the BSMP) the surface excesses of polyelectrolyte, surfactant and $\Gamma_{+/-}$ reach a maximum around $6.5 \cdot 10^{-5}$ (mono)M sPSO₂-220. Beyond this concentration all surface excesses decrease. Foam film formation is not possible in this concentration regime. This is surprising as $\Gamma_{+/-}$ indicates an increase of surface charge in comparison to lower sPSO₂-220 concentrations. The structural investigation indicates a complex layered structure in this concentration range. As shown in Fig 6.4 and discussed in section 6.3.3, this structure may result in attractive interactions between the adsorbed layers on the two foam film surfaces. It can be concluded that the foam film destabilization is due to attractive interaction caused by the formation of the thick and extended multilayer structures. An additional explanation for the low foam film stability in regime **I** and **II** could be the relatively low surface elasticity in this concentration range (as shown in Fig. 5.3 and discussed in section 5.3.1).^{58,70}

Finally, in the regime **III** (sPSO₂-220 concentrations beyond the BSMP) sPSO₂-220 NR experiments show that the surface excess of the polyelectrolyte, the surfactant and $\Gamma_{+/-}$ are constant beyond $2 \cdot 10^{-4}$ (mono)M sPSO₂-220 (Fig. 6.3). The surface excess ratio is 1:1 (Fig. 6.5), as mentioned this indicates surface charge neutrality, and also surface tension and elasticity remain constant.¹²⁵ However, in this concentration range foam film formation is again possible. The foam film stability and the surface potential of the sPSO₂-220/C₁₄TAB mixtures strongly increase (Fig. 6.5) with increasing sPSO₂-220 concentration.¹²⁵ The increase in surface potential is inconsistent with the constant surface excess ratio of 1:1 from NR measurements. An explanation could be that charged bulk complexes located in the subsurface region are the origin of the increasing surface potential, and hence the increasing foam film stability. This assumption is supported by the decrease of the zeta potential ζ with increasing polyelectrolyte concentration, indicating more and more negatively charged bulk complexes (shown in Fig. 6.1).¹²⁵ The surface is presumably now negatively charged, as the bulk complexes are more and more negatively charged and the surface excess of C₁₄TAB (the only possible source of positive charges) remains constant. For PAMPS/C₁₄TAB mixtures a similar influence of charged bulk complexes on the surface charges was found.⁷¹ The structural investigation indicates a thick but very open and solvent rich polyelectrolyte layer below a dense surfactant layer. As shown in Fig. 6.4 the repulsion of these polyelectrolyte coils could contribute to the foam film stability. It can be concluded that the strong increase in foam film stability and surface potential can be contributed to the increase in the amount of negatively charged complexes in the subsurface region. These complexes may stabilize the foam film by two different mechanisms. At first by directly influencing the surface charge and hence increasing the surface potential. The second stabilization mechanism would be the repulsion of the complexes towards each other in the film bulk, as shown in Fig. 6.4.

The present correlation of surface composition and foam film stability for sPSO₂-220/C₁₄TAB mixtures shows that the explanation of foam film stability purely by surface charges is not sufficient to describe the findings for all polyelectrolyte/surfactant mixing ratios. Hence, a new framework for assessing the foam film stability of polyelectrolyte/surfactant mixtures is proposed, taking not only the surface charges into account, but also the structure and thickness of the adsorbed layer. On the one hand, it can be stated that foam films containing extended multilayer structures are especially unstable, as the forces between the adsorbed layers may become attractive (corresponding to regime **II**). On the other hand, foam films containing 1:1 monolayers of polyelectrolyte and surfactants are especially stable (corresponding to regime **III**). Two possible foam film stabilizing mechanisms of the bulk/subsurface complexes are presented: by inducing a negative surface charge and

by inducing a negative subsurface charge. With increasing bulk complex charge both mechanisms may become stronger, further enhancing foam film stability.

6.4 Conclusion

In this chapter the surface composition and structure of sPSO₂-220/C₁₄TAB mixtures were investigated by NR and related to the foam film stability of the mixtures. For concentrations close to the BSMP a strong adsorption of surfactant and polyelectrolyte, resulting in multilayer formation, was found. This led to very unstable foam films, despite indications of a high surface charge. With increasing sPSO₂-220 concentration a transition in the adsorbed structure from multilayers to a 1:1 monolayer, indicating surface charge neutrality, was found. However, very stable foam films were found for this concentration range, indicating that charged bulk complexes can induce surface charges.⁷¹

The former framework explained foam film stability by the repulsion of surface charges of the opposite foam film surfaces. The present data shows that this stabilization mechanism is not applicable to all polyelectrolyte/surfactant ratios. Therefore, an extended framework to rationalize foam film stability is suggested, which also takes into account the structure and thickness of the adsorbed layer(s). It was shown that electrostatic repulsion between polyelectrolyte complexes in the subsurface layer can further stabilize foam films, while attractive interactions between adsorbed extended multilayers can decrease foam film stability.

Thereby, it was possible to explain the observed dependence of foam film stability on polyelectrolyte concentration in sPSO₂-220/C₁₄TAB mixtures. However, for further validation of the framework, more work on other systems is required to check if this new framework condition can be generally applied to different polyelectrolyte/surfactant mixtures or if additional factors are important. In section 7.3.5 a similar analysis is done for PSS/C₁₄TAB mixtures and discussed together with former results on PAMPS/C₁₄TAB mixtures^{15,71} and the present results on sPSO₂-220/C₁₄TAB mixtures.

Chapter 7

Surface composition and foam film stability of PSS/C₁₄TAB mixtures

Abstract

In this chapter the surface composition and foam film stability of PSS/C₁₄TAB mixtures is analyzed with neutron reflectometry (NR) and thin film pressure balance (TFPB). Hence, it is possible to compare the surface adsorption and foam film stability of PSS/C₁₄TAB mixtures to PAMPS/C₁₄TAB or sPSO₂-220/C₁₄TAB mixtures.^{15,71,125} PSS and sPSO₂-220 are chemically quite similar as they both contain a benzene ring and the same charged group. Thereby, the influence of their differences in persistence length and dissociation degree can be systematically elucidated. PAMPS completes the picture since it has a dissociation degree and persistence length similar to PSS, while it is more hydrophilic as it contains no benzene ring. NR shows a relatively strong adsorption of PSS and C₁₄TAB below the BSMP, while beyond the BSMP both compounds are depleted from the surface. Foam film formation is possible for all PSS/C₁₄TAB ratios, though the films are rather unstable in comparison to PAMPS/C₁₄TAB and sPSO₂-220/C₁₄TAB mixtures. By correlating the current findings, regarding foam film stability and surface excess, and the results from chapter 5, 6 and the literature,^{15,71} this chapter clarifies why PAMPS/C₁₄TAB and sPSO₂-220/C₁₄TAB mixtures can form more stable foam films than PSS/C₁₄TAB mixtures.

7.1 Introduction

Earlier publications have shown that for polyelectrolyte/surfactant mixtures foamability and foam stability depend on various parameters as polyelectrolyte/surfactant ratio,¹⁵ polyelectrolyte/surfactant type,³³ polyelectrolyte charge,⁵⁴ polyelectrolyte/surfactant hydrophobicity^{14,54} and pH⁴¹. It was shown that mixtures of poly(acrylamido methyl propane-sulfonate) (PAMPS) and C₁₄TAB¹⁵ and mixtures of monosulfonated poly(phenylene sulfone) (sPSO₂-220) and C₁₄TAB¹²⁵(as discussed in chapter 5) can form stable foam films. These mixtures were further investigated with neutron reflectometry (NR) to get a better insight into their surface composition in order to understand the adsorption behavior and foam film stability (as shown in chapter 6).⁷¹

While mixtures from poly(styrene sulfonate) (PSS) and C_X TAB are extensively investigated with respect to surface tension and adsorption behavior at the air/water interface,^{14,35,36,38,46,49,50,52,53,55-57,130,164} their foam film stability was only scarcely studied.¹⁴ These measurements showed that PSS/ C_{14} TAB mixtures are unable to form stable foam films. However, mixtures of PSS and C_{12} TAB, which is very similar to C_{14} TAB with just a two carbon units shorter aliphatic chain, were able to form stable foam films.¹⁴ Those foam films formed from PSS/ C_{12} TAB mixtures were even more stable than the foam films from corresponding PAMPS/ C_{12} TAB mixtures.¹⁴ Therefore, it is not clear why foam film formation is not possible for PSS/ C_{14} TAB mixtures.

PSS and PAMPS are both flexible polyelectrolytes with an intrinsic persistence length l_p of 1 nm.⁵⁷ The difference between the two is that due to the respective chemical structure PSS is more hydrophobic, while PAMPS is rather hydrophilic. sPSO₂-220 has a rather rigid polyelectrolyte backbone^{123,124} with a persistence length of around 20 nm.¹²⁵ Hence, using the three mixtures it is possible to systematically investigate the influence of polyelectrolyte hydrophobicity and polyelectrolyte backbone rigidity on surface adsorption, surface composition and foam film stability. Another difference between the three polyelectrolytes is their dissociation degree. For PAMPS and PSS the dissociation degree is around 33 %, ^{128,129} while sPSO₂-220 has a higher dissociation degrees of 54 - 61 %. ^{126,127}

The aim of this chapter is to correlate surface adsorption and foaming ability of the three mixtures and elucidate the differences and their respective origins. Therefore, NR measurements are used to investigate the surface composition of PSS/ C_{14} TAB mixtures. Furthermore, the bulk complexation was investigated with zeta potential and TFPB measurements for PSS/ C_{14} TAB mixtures were repeated. For all experiments an especially pure PSS sample was used. An important point was to find the source of the instability of foam films formed with PSS/ C_{14} TAB mixtures and to discuss possible reasons why, in contrast to this work, in literature foam film formation was found to be impossible for PSS/ C_{14} TAB mixtures.¹⁴

7.2 Results

7.2.1 Bulk interaction of PSS and C_{14} TAB

The PSS/ C_{14} TAB mixtures investigated are all transparent to the naked eye. This implies that the complexes present in solution have sufficient charge to retain colloidal stability.

To examine the charge on the PSS/C₁₄TAB complexes, zeta potential measurements were performed. For comparison with former data,^{71,125} the surfactant concentration is fixed at 10⁻⁴ M, while the PSS concentration is varied between 10⁻⁵ and 3 · 10⁻³ (mono)M. The results for mixtures of PSS and C₁₄TAB are shown in Fig. 7.1.

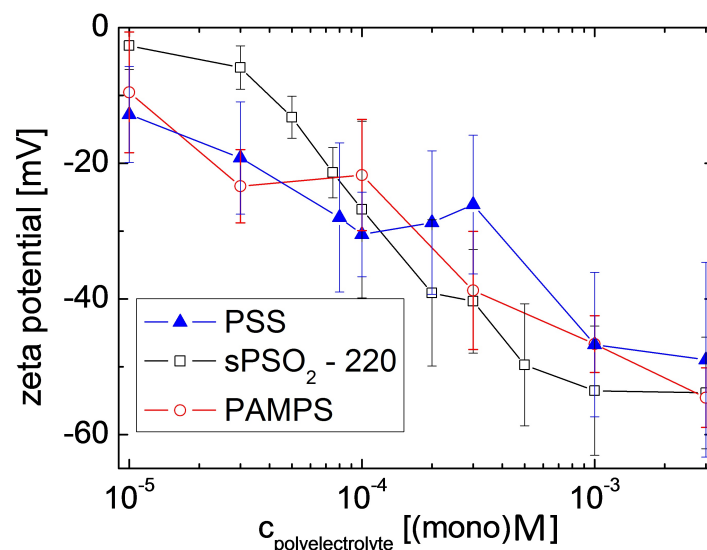


Figure 7.1: Zeta potential of PSS/C₁₄TAB mixtures in dependence of polyelectrolyte concentration. For comparison former measurements of sPSO₂-220/C₁₄TAB¹²⁵ and PAMPS/C₁₄TAB⁷¹ mixtures are added. The C₁₄TAB concentration is fixed at 10⁻⁴ M for all experiments. The error bars correspond to the intrinsic experimental error of the measurement device.

For all mixtures no charge reversal from positive to negative can be observed with increasing bulk polyelectrolyte concentration. Instead, a decrease of the zeta potential is observed with increasing polyelectrolyte concentration, indicating the formation of more and more negatively charged polyelectrolyte/C₁₄TAB complexes in bulk. For PSS/C₁₄TAB mixtures at a PSS concentration range between 2 · 10⁻⁴ and 3 · 10⁻⁴ (mono)M, the zeta potential slightly increases. This is not due to a change of overall ionic strength as also the electrophoretic mobility μ slightly increases in this concentration range (shown in Fig. 11.8 in the appendix). All other polyelectrolyte/surfactant ratios show a decreasing zeta potential with increasing polyelectrolyte concentration. For polyelectrolyte concentrations below the BSMP, sPSO₂-220/C₁₄TAB mixtures show a less negative zeta potential than solutions containing PSS or PAMPS.

7.2.2 Surface composition of PSS/C₁₄TAB mixtures

To reveal the surface composition of PSS/C₁₄TAB mixtures with respect to the PSS concentration, and to examine the origin of the foam film instability, NR measurements were carried out. Firstly, mixtures of PSS with deuterated surfactant (dC₁₄TAB) in air contrast matched water (ACMW) were measured. Here, the specular reflectivity signal is dominated by scattering from the deuterated surfactant present at the interface. Adsorbed PSS also contributes to the reflected signal. Nevertheless, since it is hydrogenous, it has a relatively low scattering length density (SLD) and its contribution is small. The contribution of the solvent to the specular reflection is negligible. Secondly, NR measurements were carried out for mixtures of PSS and air-contrast-matched surfactant (cmC₁₄TAB) in ACMW. This approach exploits the high flux at the natural low incidence angle of the FIGARO reflectometer to separate the weak signal from adsorbed hydrogenous polymer from the background.^{50,52,71} Fig 7.2 a) and 7.2 b) show examples of neutron reflectivity profiles for PSS/dC₁₄TAB mixtures in ACMW for various polyelectrolyte concentrations as well as the corresponding model fits. Fig. 7.2 c) and 7.2 d) show equivalent plots for the PSS/cmC₁₄TAB solutions.

With increasing PSS concentration the reflectivities seem to decrease in both isotopic contrasts, implying that the maximum in surface excess of both components is reached at low or intermediate bulk PSS concentrations. For further analysis, the reflectivity profiles were transformed into the surface excess of each component using the method described in the experimental section 4.3 and in the literature.^{50,52,71}

Fig. 7.3 shows the surface excesses of the two components and the resulting surface excess of charges $\Gamma_{+/-}$ with respect to the bulk PSS concentration. When complete dissociation is assumed $\Gamma_{+/-}$ is proportional to the surface charge and can hence be used as a measure of the surface charges induced by the surface composition. $\Gamma_{+/-}$ is calculated as follows:

$$|\Gamma_{+/-}| = \Gamma_{C_{14}TAB} - \Gamma_{PSS} \quad (7.1)$$

Similar trends are observed for both the polyelectrolyte and the surfactant. Already at the lowest measured bulk PSS concentration, there is an enhanced surface adsorption of C₁₄TAB in the mixture compared with the pure surfactant in absence of polyelectrolyte.⁷¹ In this concentration range adsorbed PSS is also detected. With increasing PSS concentration, the adsorbed amounts of both components at the interface increase slightly with maximum values found at bulk PSS concentrations close to the BSMP. At and beyond the

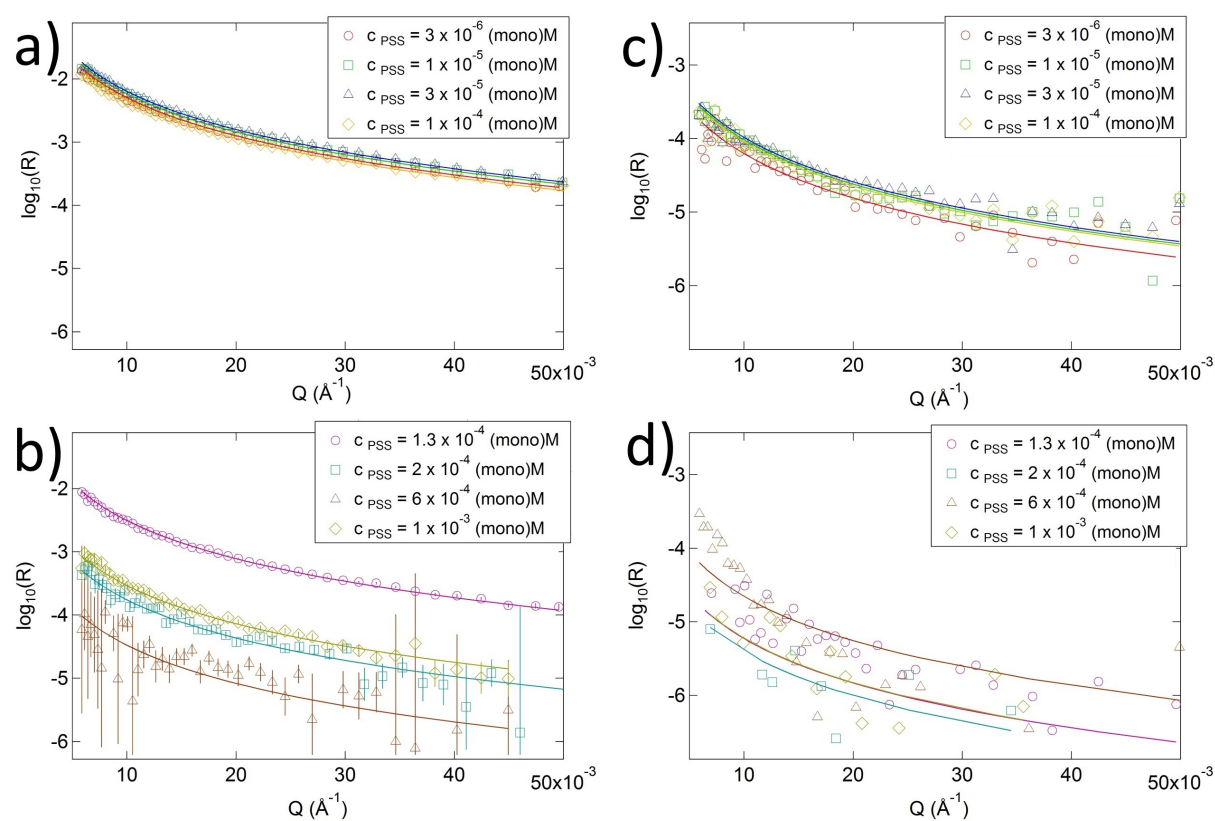


Figure 7.2: Neutron reflectivity profiles for solutions prepared from PSS/dC₁₄TAB, a) and b), or PSS/cmC₁₄TAB, c) and d), in ACMW. The concentration of PSS is varied, while the bulk surfactant concentration is fixed at 10^{-4} M. The solid lines correspond to model fits. For clarity, not all recorded NR profiles are shown. Additional NR profiles can be found in the appendix (Fig. 11.6 and 11.7).

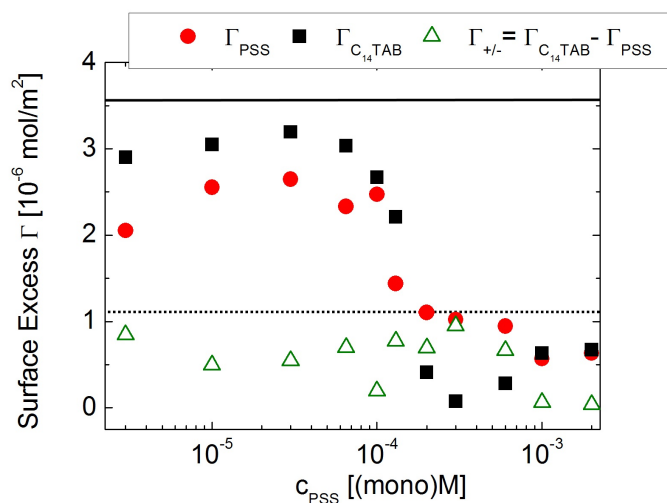


Figure 7.3: Surface excesses Γ derived from NR measurements of PSS and C_{14} TAB in their mixtures in dependence of PSS concentration. For all mixtures the concentration of C_{14} TAB is fixed at 10^{-4} M. The dotted line corresponds to the surface excess of a pure C_{14} TAB solution at a concentration of 10^{-4} M.⁷¹ The solid black line corresponds to the surface excess of a pure C_{14} TAB solution at the cmc ($3.5 \cdot 10^{-3}$ M).¹⁶³ Furthermore, the surface excess $\Gamma_{+/-}$ of charges is shown.

BSMP the surface excess of both components is strongly decreasing. A similar decrease in adsorption beyond the BSMP was also found for PSS/ C_{14} TAB mixtures at higher concentrations of 2.4 mM using ellipsometry.³⁶ For bulk PSS concentrations between $2 \cdot 10^{-4}$ and $6 \cdot 10^{-4}$ (mono)M $\Gamma_{C_{14}TAB}$ is close to 0 mol/m², while Γ_{PSS} stays relatively constant at $1 \cdot 10^{-6}$ mol/m². Beyond bulk PSS concentrations of $1 \cdot 10^{-3}$ (mono)M the surface excess of both components is at a 1:1 ratio at $0.6 - 0.7 \cdot 10^{-6}$ mol/m².

The surface excess, and hence the surface composition, plotted in Fig. 7.3 does not indicate any apparent reasons for foam film instability as both, polyelectrolyte and surfactant, adsorbed at the air/water interface for most of the polyelectrolyte/surfactant ratios. Furthermore, the $\Gamma_{+/-}$ curve implies that the surface is charged for most of the polyelectrolyte/surfactant ratios. Thus, the former TFPB measurements¹⁴ of these mixtures were repeated.

7.2.3 Foam film stability of PSS/ C_{14} TAB mixtures

It should be noted that in the present work and in the former work on PSS/ C_{14} TAB mixtures not the same batch of PSS was used.¹⁴ In the present work very pure PSS of GPC quality with a M_w of 77400 g/mol was used as received. In the former work PSS

with a M_w of 70000 g/mol was used. It was purified in an ultrafiltration cell with a cut-off membrane of 20000 Da .¹⁴

In this work all investigated PSS/C₁₄TAB foam films were found to be homogeneous, while in literature unstable and inhomogeneous PSS/C₁₄TAB foam films were reported.¹⁴ Fig. 7.4 shows some disjoining pressure isotherms of PSS/C₁₄TAB mixtures.

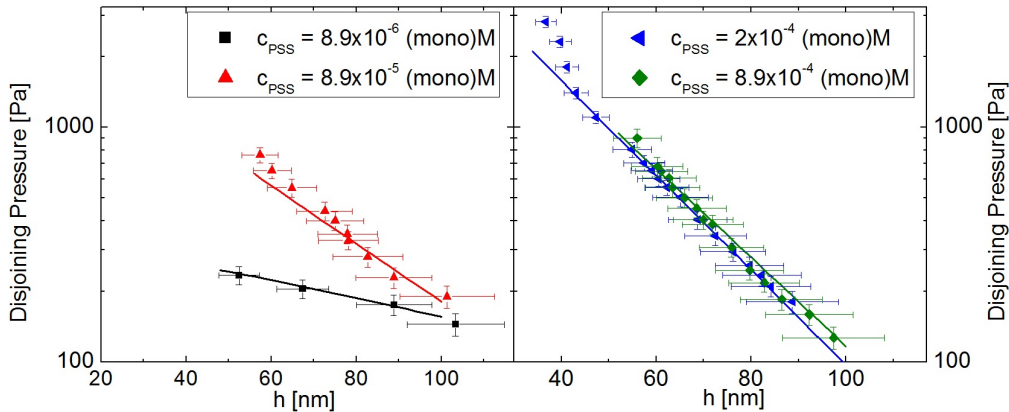


Figure 7.4: Disjoining pressure isotherms of PSS/C₁₄TAB solutions with fixed C₁₄TAB concentration (10^{-4} M) and variable PSS concentration. The solid lines correspond to simulations at constant potential. Isotherms of mixtures with PSS concentrations below and beyond the BSMP are shown separately.

The maximum disjoining pressure Π_{\max} before film rupture can be taken as a measure of foam stability. In Fig. 7.5 Π_{\max} for PSS/C₁₄TAB is shown in dependence on the polyelectrolyte concentration. For comparison measurements for PAMPS/C₁₄TAB and sPSO₂-220/C₁₄TAB mixtures are added.^{15,125}

In comparison to PAMPS/C₁₄TAB and sPSO₂-220/C₁₄TAB mixtures, Π_{\max} of PSS/C₁₄TAB mixtures shows some differences. At first, no point of destabilization close to the BSMP was detected. Secondly, the stability of PSS/C₁₄TAB foam films does not increase continuously with the polyelectrolyte concentration beyond the BSMP. A maximum in foam film stability is reached between $2 \cdot 10^{-4}$ and $2.5 \cdot 10^{-4}$ (mono)M PSS. At this point the foam film stability of PSS/C₁₄TAB mixtures exceeds the foam film stability of pure C₁₄TAB at $1 \cdot 10^{-4}$ M. For higher PSS concentrations the foam film stability is relatively constant at a lower level.

Beyond PSS concentrations of $2 \cdot 10^{-4}$ (mono)M stratification was observed (shown in Fig. 7.6). This stratification process took place for quite thick films, so the step width of this stratification could not be extracted. Stratification and structuring was also previously

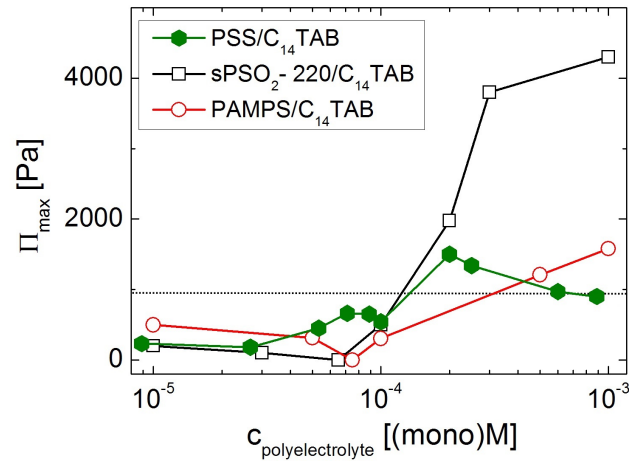


Figure 7.5: The maximum disjoining pressure Π_{max} before film rupture versus polyelectrolyte concentration for PSS/ C_{14} TAB foam films in comparison to sPSO₂-220/ C_{14} TAB¹²⁵ and PAMPS/ C_{14} TAB¹⁵ foam films (data taken from the literature). For all curves the C_{14} TAB concentration is fixed at 10^{-4} M, while the polyelectrolyte concentration is varied. The error bars correspond to the size of the symbols. The dashed line corresponds to the stability of a pure C_{14} TAB film at 10^{-4} M.¹⁵

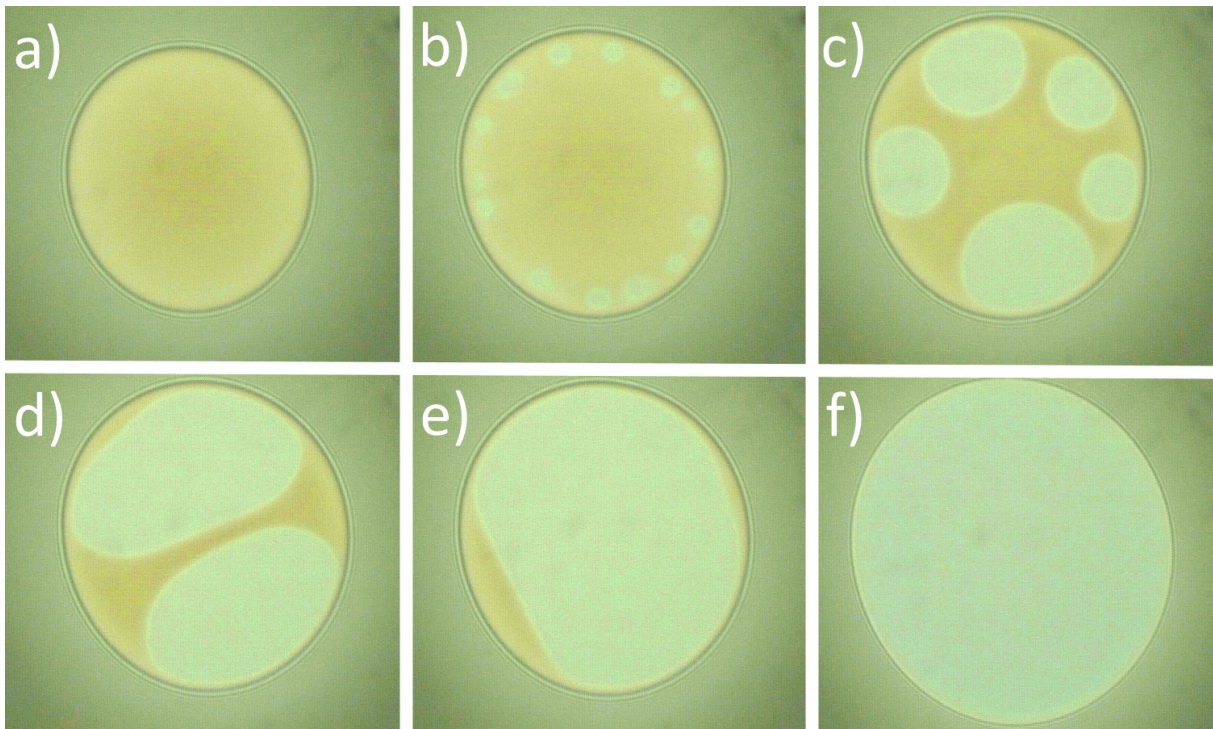


Figure 7.6: Stratification events taking place before the start of a TFPB measurements for PSS/ C_{14} TAB foam films with a PSS concentration of $2 \cdot 10^{-4}$ (mono)M. The notation from a) to f) shows the progress of the stratification. The stratification event is fast and terminated within seconds.

observed with CP-AFM and SAXS for pure PSS of similar length (discussed in chapter 8).¹⁶ In the effective measurement range of the TFPB no stratification event was recorded. Moreover, for none of the other foam films, formed with different polyelectrolytes (PAMPS and sPSO₂-220) and used for comparison, stratification was observed in the investigated concentration range.^{15,125}

From the slope of the disjoining pressure isotherms the Debye length κ^{-1} and ionic strength I_{exp} were extracted (Table 7.1).⁶³ Typically, the evaluation of the slope of an disjoining pressure isotherms (and the following simulation with the nonlinear Poisson-Boltzmann equation) is not possible if stratification occurred. This is due to the fact that the slope of the isotherm changes after the stratification event (as shown in the isotherms in the next chapter Fig. 8.6 a) and Fig. 11.11 and in the literature^{18,33}). However, as shown in Fig. 7.4 disjoining pressure isotherms from PSS/C₁₄TAB mixtures do not seem to be influenced by the stratification event. This is presumably due to the fact that for this system stratification occurs for very thick films and hence the isotherms for thin films are not so much influenced by stratification.

As in chapter 5 the experimentally determined ionic strength I_{exp} is compared to the maximum ionic strength $I_{max\ diss}$ and the complex ionic strength $I_{complex}$ (see Table 7.1). $I_{max\ diss}$ is the ionic strength of the system assuming complete dissociation, while $I_{complex}$ is the ionic strength of the system assuming complete dissociation and 1:1 binding between polyelectrolytes and surfactants. If the experimental ionic strength I_{exp} is smaller than the complex ionic strength $I_{complex}$, dissociation is assumed to be incomplete. If the experimental ionic strength I_{exp} is higher than the complex ionic strength $I_{complex}$, this indicates no 1:1 complexation.

To extract further information from the disjoining pressure isotherms they are simulated with the nonlinear Poisson-Boltzmann equation at constant potential with the PB program version 2.2.1.^{144,145} The results of this simulation are listed in Table 7.1. These results can be compared to former measurements on PAMPS/C₁₄TAB mixtures and sPSO₂-220/C₁₄TAB mixtures (which are shown in chapter 5, Table 5.1.).^{15,125}

For all PSS/C₁₄TAB mixtures I_{exp} is smaller (except for $c_{PSS} = 2 \cdot 10^{-4}$ (mono)M) than $I_{max\ diss}$ and $I_{complex}$, showing that the dissociation was not complete. For $2 \cdot 10^{-4}$ (mono)M PSS I_{exp} is higher than $I_{complex}$, but smaller than $I_{max\ diss}$. This indicates that the dissociation is relatively high for that concentration, but no 1:1 complexation takes place.

The results of the Poisson-Boltzmann simulation for PSS/C₁₄TAB mixtures are significantly different from the results for sPSO₂-220/C₁₄TAB or PAMPS/C₁₄TAB mixtures. For the

| c_{PSS} [(mono)M] | $ \Psi_0 $ [mV] | κ^{-1}_{exp} [nm] | I_{exp} [M] | $I_{\text{max diss}}$ [M] | I_{complex} [M] |
|----------------------------|-----------------|--------------------------|---------------------|---------------------------|--------------------------|
| $8.9 \cdot 10^{-6}$ | 74 | 112.1 | $7.4 \cdot 10^{-6}$ | $1.1 \cdot 10^{-4}$ | $1.0 \cdot 10^{-4}$ |
| $2.7 \cdot 10^{-5}$ | 50 | 65.8 | $2.1 \cdot 10^{-5}$ | $1.3 \cdot 10^{-4}$ | $1.0 \cdot 10^{-4}$ |
| $5.3 \cdot 10^{-5}$ | 48 | 42.9 | $5.1 \cdot 10^{-5}$ | $1.5 \cdot 10^{-4}$ | $1.0 \cdot 10^{-4}$ |
| $7.1 \cdot 10^{-5}$ | 57 | 32.3 | $8.9 \cdot 10^{-5}$ | $1.7 \cdot 10^{-4}$ | $1.0 \cdot 10^{-4}$ |
| $8.9 \cdot 10^{-5}$ | 65 | 32.9 | $8.6 \cdot 10^{-5}$ | $1.9 \cdot 10^{-4}$ | $1.0 \cdot 10^{-4}$ |
| $1 \cdot 10^{-4}$ | 59 | 28.2 | $1.2 \cdot 10^{-4}$ | $2.0 \cdot 10^{-4}$ | $1.0 \cdot 10^{-4}$ |
| $2 \cdot 10^{-4}$ | 74 | 20.4 | $2.2 \cdot 10^{-4}$ | $3.0 \cdot 10^{-4}$ | $2.0 \cdot 10^{-4}$ |
| $2.5 \cdot 10^{-4}$ | 69 | 34.6 | $7.7 \cdot 10^{-5}$ | $3.5 \cdot 10^{-4}$ | $2.5 \cdot 10^{-4}$ |
| $6 \cdot 10^{-4}$ | 55 | 31.6 | $9.3 \cdot 10^{-5}$ | $7.0 \cdot 10^{-4}$ | $6.0 \cdot 10^{-4}$ |
| $8.9 \cdot 10^{-4}$ | 75 | 21.8 | $2.0 \cdot 10^{-4}$ | $9.9 \cdot 10^{-4}$ | $8.9 \cdot 10^{-4}$ |

Table 7.1: Summary of the Poisson-Boltzmann simulation of the disjoining pressure isotherms of PSS/C₁₄TAB films: surface potential Ψ_0 , Debye length κ^{-1} and ionic strength I_{exp} (extracted by an exponential fit to the data). For comparison the maximum ionic strength $I_{\text{max diss}}$ (complete dissociation) and the complex ionic strength I_{complex} (complete dissociation and polyelectrolyte/surfactant complex formation in a 1:1 ratio) are listed. Due to the experimental error of the TFPB an average error of $\pm 10\%$ can be assumed for all parameters. The former results for sPSO₂-220/C₁₄TAB, PAMPS/C₁₄TAB and pure C₁₄TAB are shown in Table 5.1.^{15,125}

latter two mixtures I_{exp} shows a continuous increase with increasing polyelectrolyte concentration. I_{exp} and Ψ_0 are shown in dependence of PSS concentration in Fig. 7.7.

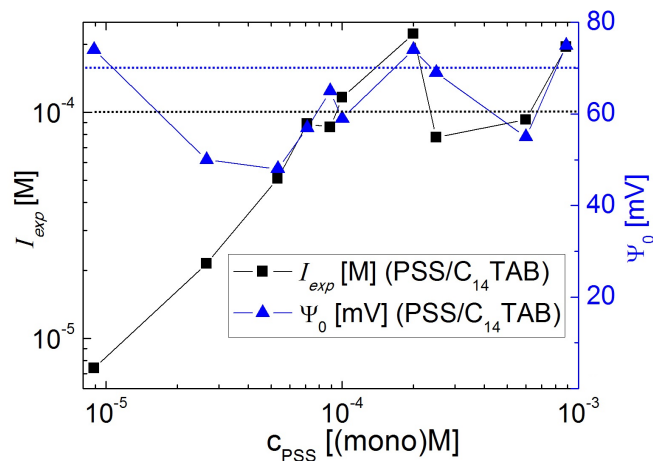


Figure 7.7: The experimentally determined ionic strength I_{exp} and the surface potential Ψ_0 in dependence of PSS concentration for PSS/C₁₄TAB foam films. The C₁₄TAB concentration is fixed at 10^{-4} M. The dotted black line corresponds to I_{exp} of a pure C₁₄TAB film at 10^{-4} M, while the dotted blue line corresponds to Ψ_0 of a pure C₁₄TAB film at 10^{-4} M.¹⁵

For PSS/C₁₄TAB mixtures I_{exp} increases, until a local maximum at $c_{\text{PSS}} = 2 \cdot 10^{-4}$ (mono)M

is reached. Beyond this PSS concentration I_{exp} decreases until $c_{PSS} = 2.5 \cdot 10^{-4}$ (mono)M, while for even higher PSS concentrations it increases again. The surface potential Ψ_0 also shows a different trend for PSS/C₁₄TAB mixtures than for the mixtures containing PAMPS or sPSO₂-220. Typically, for polyelectrolyte surfactant mixtures Ψ_0 decreases with increasing polyelectrolyte concentration until the BSMP is reached. Beyond the BSMP Ψ_0 usually increases again.^{14,37} For PSS/C₁₄TAB mixtures Ψ_0 decreases for low PSS concentrations until a local minimum is reached for $5.3 \cdot 10^{-5}$ (mono)M PSS. Beyond this concentration Ψ_0 increases again until a local maximum is reached for $c_{PSS} = 2 \cdot 10^{-4}$ (mono)M. Beyond this concentration the surface potential decreases until $6 \cdot 10^{-4}$ (mono)M PSS and increases again beyond this concentration. Interestingly, for the concentration of $2 \cdot 10^{-4}$ (mono)M, which shows a local maximum in ionic strength I_{exp} and surface potential Ψ_0 , the highest overall foam film stability was measured.

7.3 Discussion

7.3.1 Origins of the differences between former and current results for PSS/C₁₄TAB mixtures

As already mentioned, it should be noted that in the present work and in the former work on PSS/C₁₄TAB mixtures not the same batch of PSS was used.¹⁴ However, the batches are similar. In the present work the used PSS was very pure and had a M_w of 77400 g/mol. In the former work PSS with a M_w of 70000 g/mol was used. It was purified in an ultrafiltration cell with a cut-off membrane of 20000 Da.¹⁴ It was previously assumed that the ultrafiltration cell was able to remove all small ion impurities and that the 10 % difference in molecular weight has no significant influence on adsorption and foam film properties.¹⁴ Obviously, these assumptions seem to be wrong as the foam film properties found here differ from the properties reported in the literature.¹⁴ One possibility is that the ultrafiltration cell did not completely remove all small ion impurities. That would result in an enhanced screening of the charges and hence in less stable and less homogeneous foam films.^{68,165} Another reason could be the 10 % difference in molecular weight. However, this is unlikely as literature has shown that there is no significant changes in adsorption at the air/water interface⁵⁶ and ordering^{16,83} for such small differences in molecular weight.

Furthermore, in the literature the sample holder was pulled out of the sample solution and left for equilibration for 30 min before the experiment. Some measurements of the adsorption kinetics of PSS/C₁₄TAB mixtures with NR indicated that this period of time

is not sufficient to reach equilibrium. Hence, in this work the equilibration time was increased to 2 h.

7.3.2 Bulk interaction of PSS and C₁₄TAB

For most of the investigated polyelectrolyte/surfactant mixtures ratios with increasing polyelectrolyte concentration a decrease in zeta potential is observed (shown in Fig. 7.1), indicating the formation of more and more negatively charged polyelectrolyte/C₁₄TAB complexes in bulk. The fact that only negative zeta potentials were measured means that for all investigated polyelectrolytes even at the lowest bulk polyelectrolyte concentration measured, the chemical potential of the bulk C₁₄TAB is insufficient to neutralize the bulk complexes.

However, there are two peculiar findings. Firstly, below the BSMP, sPSO₂-220 solutions show a less negative zeta potential than solutions containing PSS or PAMPS. As discussed earlier the dissociation degree of sPSO₂-220 is higher than for PSS or PAMPS.¹²⁴ Hence, the driving force for C₁₄TAB to interact with sPSO₂-220 might be higher, resulting in complexes which are less negatively charged. Secondly, for PSS concentrations from $2 \cdot 10^{-4}$ to $3 \cdot 10^{-4}$ (mono)M, the zeta potential seems to remain constant or even slightly increased. A possible reason for the decrease in negativity of PSS complexes, in this narrow concentration range, could be that surfactant molecules get depleted from the air/water interface and move to the bulk phase. Due to the incorporation of those surfactant molecules into already formed polyelectrolyte/surfactant complexes the zeta potential of the complexes increase. Indeed with NR experiments, shown in Fig. 7.3, a depletion of surfactant molecules for this specific concentration range was detected. No obvious reason could be found why, in this specific concentration range, PSS draws C₁₄TAB from the air/water interface into the bulk. For higher PSS concentration zeta potential (Fig. 7.1: decreasing zeta potential) and NR experiments (Fig. 7.3: increasing surface excess) show that C₁₄TAB is again released from the bulk to the air/water interface. Thus, the reason for preferred bulk complexation of PSS/C₁₄TAB mixtures in the PSS concentration range from $2 \cdot 10^{-4}$ to $3 \cdot 10^{-4}$ (mono)M merits further investigation.

7.3.3 Surface composition of PSS/C₁₄TAB mixtures

For PSS concentrations below the BSMP a substantial amount of PSS and C₁₄TAB adsorbs at the air/water interface (shown in Fig. 7.3). Additional PSS only slightly enhances the

adsorption of both compounds until a maximum close to the BSMP is reached. In this concentration regime $\Gamma_{C_{14}TAB}$ is higher for the mixture than it is for pure C₁₄TAB,⁷¹ indicating a strong synergistic adsorption. As discussed in chapter 2.1.2 the adsorption of surfactant is enhanced in polyelectrolyte/surfactant mixtures due to (a) the decrease in electrostatic repulsion between positively charged surfactant headgroups at the surface and (b) the increase in entropy due to the release of counterions.^{42,43} Furthermore, there is excess C₁₄TAB at the interface indicating a positive surface charge (Fig. 7.3). The increase in surface excess is due to the increasing PSS concentration. The more PSS is in the mixture the more polyelectrolyte/surfactant complexes can form and synergistically adsorb at the surface, leading to an increase of both $\Gamma_{C_{14}TAB}$ and Γ_{PSS} .

Close to the BSMP both $\Gamma_{C_{14}TAB}$ and Γ_{PSS} strongly decrease. In the concentration range $2 \cdot 10^{-4}$ to $6 \cdot 10^{-4}$ (mono)M Γ_{PSS} is higher than $\Gamma_{C_{14}TAB}$. These results are in accordance to zeta potential measurements (Fig. 7.1), which show a decrease of bulk complex negativity at $2 \cdot 10^{-4}$ and $3 \cdot 10^{-4}$ (mono)M, indicating that the positively charged surfactants move from the surface to the bulk. Both results indicate that in this concentration range the complexation in bulk is preferred. One reason for this might be the formation of hydrophilic PSS/C₁₄TAB complexes in bulk as suggested in the literature.^{14,56}

Beyond a concentration of $1 \cdot 10^{-3}$ (mono)M PSS C₁₄TAB adsorbs again at the surface and both surface excesses stay constant at a comparatively low level. C₁₄TAB probably readsorbs at the surface as the total ionic strength increases (due to the increasing PSS concentration). Hence, the surface charges are screened and thus more molecules can adsorb at the surface.⁷¹

Investigations of PSS/C₁₄TAB mixtures were also conducted with NR in the past.⁵⁵ PSS with a M_w of 43000 g/mol was used and its concentration was kept constant at 20 ppm (corresponding roughly to $1 \cdot 10^{-4}$ (mono)M). The concentration of C₁₄TAB was varied from $2 \cdot 10^{-4}$ M to $6 \cdot 10^{-3}$ M. Therefore, the current results can be hardly compared to the results from the literature, as different parameters were varied. Furthermore, in the mentioned article only $\Gamma_{C_{14}TAB}$ was determined and the contribution from the hydrogenous PSS was not subtracted. Hence, $\Gamma_{C_{14}TAB}$ is higher and less precise in the literature,⁵⁵ than in the current work. For C₁₄TAB concentrations from $2 \cdot 10^{-4}$ M to $3.2 \cdot 10^{-3}$ M $\Gamma_{C_{14}TAB}$ was slightly higher in the literature but in the order of the values for $\Gamma_{C_{14}TAB}$ shown here (this work $\Gamma_{C_{14}TAB} \approx 2.6 - 3.2 \cdot 10^{-6}$ mol/m² vs. $\Gamma_{C_{14}TAB} = 2.8 - 3.9 \cdot 10^{-6}$ mol/m²).⁵⁵ For C₁₄TAB concentrations higher than $3.2 \cdot 10^{-3}$ M very thick multilayers of C₁₄TAB were found in the literature ($\Gamma_{C_{14}TAB} = 11 \cdot 10^{-6}$ mol/m²) which were not found in this

work.⁵⁵ As mentioned due to the experimental differences both investigations focus on different polyelectrolyte/surfactant ratios, however for polyelectrolyte/surfactant (and surfactant/polyelectrolyte) ratios close from 0.2 to 1 (and 1 to 0.2) a similar $\Gamma_{C_{14}TAB}$ was found, which is a hint for the similarity of the adsorbed layers.

To conclude, the surface composition of the current experiments indicates a strong adsorption below the BSMP, while beyond it the adsorption is significantly weaker. This is in accordance with former surface tension measurements, which showed low surface tensions below the BSMP and surface tension values close to that of water beyond the BSMP.¹⁴

7.3.4 Foam film stability of PSS/C₁₄TAB mixtures

As already mentioned, former measurements of PSS/C₁₄TAB mixtures did not show any stable foam films over the whole PSS concentration range.¹⁴ This was contributed to a special destabilizing interaction of longer trimethylammonium bromide surfactants and the benzyl ring of PSS,^{14,55,56} leading to hydrophilic complexes which stayed in bulk. However, within this work PSS/C₁₄TAB mixtures were able to form foam films. Nevertheless, the foam films from PSS/C₁₄TAB mixtures showed a significantly lower stability and different trends than foam films of comparable polyelectrolyte/surfactant mixtures (as shown in Fig. 7.5).

As shown in table 7.1 (in comparison to Table 5.1) the PSS/C₁₄TAB mixtures show different trends in I_{exp} and Ψ_0 than mixtures of sPSO₂-220 or PAMPS with C₁₄TAB. The differences are reported in section 7.2.3. The discontinuous behavior of I_{exp} and Ψ_0 for PSS/C₁₄TAB mixtures indicate that a process in bulk takes place, which is not occurring for mixtures of sPSO₂-220 or PAMPS with C₁₄TAB. This process is probably the formation of hydrophilic PSS/C₁₄TAB complexes,^{14,36,56} starting close to the BSMP and being developed the strongest at $2 \cdot 10^{-4}$ (mono)M. This complexation seems to draw PSS and to a stronger degree C₁₄TAB from the surface into the bulk (as seen from NR measurements in Fig. 7.3 and zeta potential measurements in Fig. 7.1). This is in accordance with surface tension and surface elasticity results from the literature which also show a strong depletion beyond the BSMP.¹⁴ Especially the discontinuous trend in I_{exp} shows that the interaction of PSS and C₁₄TAB differs strongly from the interaction of PAMPS or sPSO₂-220 with C₁₄TAB. Beyond a PSS concentration of $5 \cdot 10^{-4}$ (mono)M I_{exp} and Ψ_0 show again a continuous increase with increasing PSS concentration.

The maximum disjoining pressure Π_{max} (shown in Fig. 7.5) also does not show a clear trend. Below the BSMP the foam film stability of PSS/C₁₄TAB mixtures increases with increasing PSS concentration. However, it is still lower than the foam film stability of pure C₁₄TAB at $1 \cdot 10^{-4}$ M. NR measurements reveal a relatively constant layer of intermediate thickness of both polyelectrolyte and surfactant, which is only slightly positively charged (shown in Fig. 7.3). This is in accordance with Ψ_0 values in the same concentration range which are rather low but increase with increasing PSS concentration indicating an increase in repulsion and leading to an increase in foam film stability.

The highest foam film stability was measured in the concentration range from $2 \cdot 10^{-4}$ to $2.5 \cdot 10^{-4}$ (mono)M. NR experiments show that surfactant molecules are depleted from the surface in this concentration range. Zeta potential measurements indicate that those surfactant molecules decrease the negative charges of the polyelectrolyte/surfactant complexes in bulk (shown in Fig. 7.1 and Fig. 7.3). This is in accordance to the maximum in ionic strength I_{exp} and surface potential Ψ_0 measured with TFPB for this concentration range (shown in table 7.1). Thus, in this range the repulsion of charges on the opposing film surfaces is the largest leading to the most stable foam films. However, it is still unclear why PSS adsorbs at the air/water interface when there is hardly any surfactant available for coadsorption.

For PSS concentrations beyond $2.5 \cdot 10^{-4}$ (mono)M the foam film stability is constant and close to the value of pure C₁₄TAB at $1 \cdot 10^{-4}$ M. The surface composition in Fig. 7.3 shows that in this concentration range less C₁₄TAB adsorbs at the surface than for pure C₁₄TAB at $1 \cdot 10^{-4}$ M, which indicates an even lower foam film stability than for pure C₁₄TAB. However, also PSS adsorbs at the surface and the complexes in bulk are highly negative (as shown in Fig. 7.1). Both effects increase the foam film stability, and hence the resulting foam film stability is similar to that of pure C₁₄TAB.

An obvious reason for the relatively low foam film stability of PSS/C₁₄TAB mixtures in comparison to mixtures of sPSO₂-220/PAMPS and C₁₄TAB is the depletion of PSS and C₁₄TAB beyond the BSMP (shown by NR in Fig. 7.3) The depletion might be caused by the formation of hydrophilic PSS/C₁₄TAB complexes in bulk.^{14,36,56} Another possible reason for foam film destabilization for PSS/C₁₄TAB mixtures is the occurrence of stratification events already at very low concentrations of $2 \cdot 10^{-4}$ (mono)M (shown in Fig. 7.6). sPSO₂-220/C₁₄TAB mixtures show stratification only beyond a concentration of $3 \cdot 10^{-3}$ (mono)M (as discussed in chapter 8), while PAMPS/C₁₄TAB mixtures show stratification beyond a concentration of $1 \cdot 10^{-3}$ (mono)M.¹³¹ Stratification is known to influence foam film stability. It was shown that if stratification occurs for films thinner than

100 nm this can stabilize foam films by slowing water drainage.³⁹ It was not yet investigated if and how stratification influences the foam film stability when it occurs for thicker films. Thus, foam films showing stratification have to be carefully compared to films which do not show precipitation with respect to their maximum disjoining pressure Π_{max} .^{8,63} One possible reason why the PSS/C₁₄TAB mixtures show stratification already at such low polyelectrolyte concentration could be the higher amount of complexes in bulk. Fig. 7.8 shows that beyond the BSMP the surface excess for PSS/C₁₄TAB mixtures is much lower than for the other mixtures. As follows, there are more polyelectrolytes and surfactants available for complexation in bulk for PSS/C₁₄TAB mixtures, reducing the inter-chain distance d and thus inducing stratification at lower polyelectrolyte concentrations.

7.3.5 Application of the extended framework for foam film (de)stability of polyelectrolyte/surfactant mixtures

PSS/C₁₄TAB mixtures showed a trend in foam film stability with increasing polyelectrolyte concentration significantly different to other polyelectrolyte/surfactant mixtures (shown in Fig. 7.5). In this section the foam film stability is discussed with respect to the surface composition (which depends on the surface excess shown in Fig. 7.8) and the extended framework developed in chapter 6.

The surface composition of the three polyelectrolytes in mixtures with C₁₄TAB shows some significant differences. While the surface excess of sPSO₂-220/C₁₄TAB mixtures shows a maximum close to the BSMP, for the two other mixtures no maximum can be found. However, all mixtures show a decrease in the surface excess of both polyelectrolyte and surfactant beyond the BSMP. The comparability of the data from PAMPS/C₁₄TAB mixtures is hampered by the limited amount of measured polyelectrolyte concentrations.⁷¹ As there is no data available in the concentration regime **II**, which shows the maximum for sPSO₂-220/C₁₄TAB mixtures, it has to be noticed that PAMPS/C₁₄TAB mixtures might also show a maximum in adsorption. A possible reason why mixtures of sPSO₂-220 with C₁₄TAB show a maximum in adsorption (correlating with multilayer formation as indicated by structural data) in contrast to mixtures containing PSS and PAMPS, could be the difference in polyelectrolyte backbone rigidity. The stiffer backbone of sPSO₂-220 leads to flat adsorption for certain polyelectrolyte/surfactant ratios (as shown by structural data in chapter 6), which might enhance multilayer formation and hence result in a surface excess maximum for polyelectrolyte and surfactant.

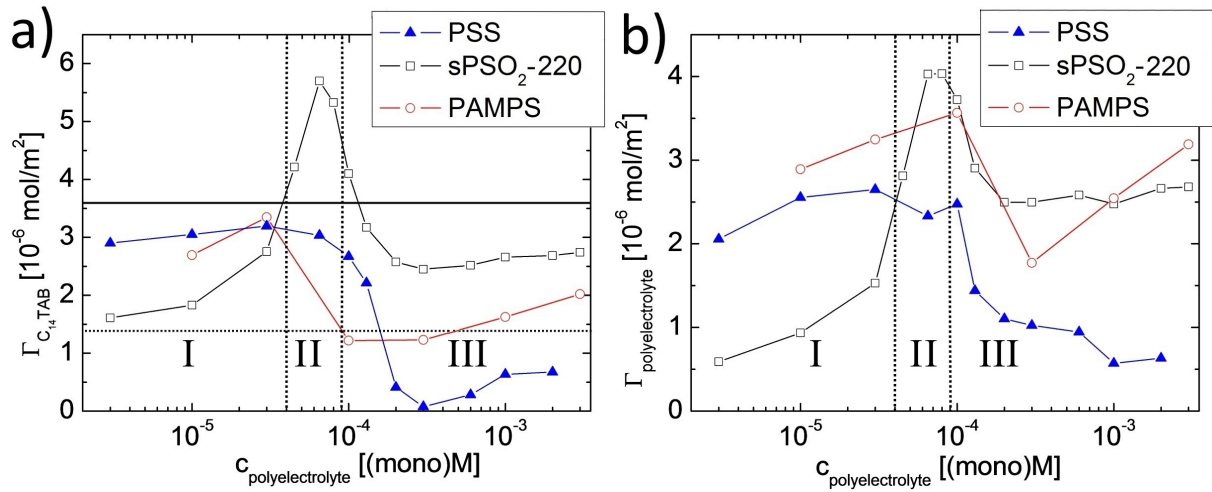


Figure 7.8: a) Comparison of $\Gamma_{C_{14}TAB}$ for different polyelectrolytes in dependence of polyelectrolyte concentration. The dashed black line corresponds to the surface excess of a pure C₁₄TAB solution at a concentration of 10^{-4} M.⁷¹ The solid black line corresponds to the surface excess of a pure C₁₄TAB solution at the cmc ($3.5 \cdot 10^{-3}$ M).¹⁶³ b) Comparison of $\Gamma_{Polyelectrolyte}$ for different polyelectrolytes in dependence of polyelectrolyte concentration. For all mixtures the concentration of C₁₄TAB is fixed at 10^{-4} M. The horizontal dotted lines divide the plots into three concentration regimes, corresponding to the regimes discussed in chapter 6.

For all investigated PAMPS/C₁₄TAB mixtures basic structural investigations indicated a layer of surfactants with a polyelectrolyte layer underneath.⁷¹ No extended multilayer structure was found. However, no complex evaluation of the structure for PAMPS/C₁₄TAB mixtures was conducted, as the evaluation was mostly used to extract the surface excess.⁷¹ Hence it is not clear how thick the adsorbed polyelectrolyte and surfactant layers are and to which degree they are penetrated by solvent. Also for PSS/C₁₄TAB mixtures no structural data for the discussed polyelectrolyte/surfactant ratios was recorded yet. This data would be useful to investigate the exact surface structure and compare it with the other mixtures. It might also help to clarify why PSS adsorbs at the surface (concentration range from $2 \cdot 10^{-4}$ to $6 \cdot 10^{-4}$ (mono)M), even if there is hardly any surfactant available for synergistic adsorption.

The extended framework for polyelectrolyte/surfactant foam films stabilization, presented in chapter 6, can also be applied to PSS/C₁₄TAB and PAMPS/C₁₄TAB mixtures. One assumption of the extended framework is that at polyelectrolyte concentrations beyond the BSMP, 1:1 ratios of polyelectrolyte and surfactant and highly charged polyelectrolyte/surfactant bulk complexes result in especially stable foams. It is shown in Fig. 7.3 and Fig. 7.5 that this is not the case for PSS/C₁₄TAB mixtures, which beyond a concen-

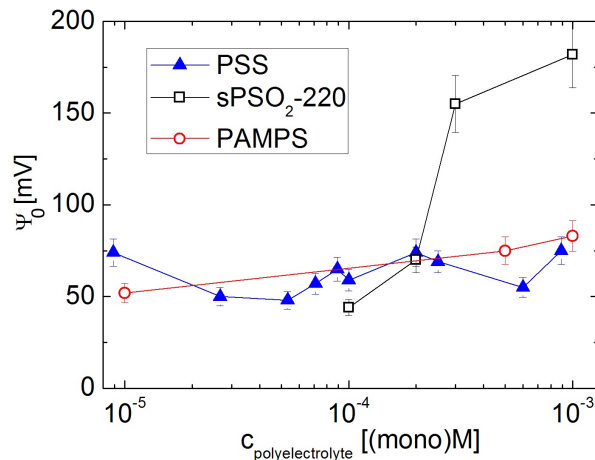


Figure 7.9: The surface potential Ψ_0 of various polyelectrolyte/ C_{14} TAB in dependence of polyelectrolyte concentration. The C_{14} TAB concentration is fixed at 10^{-4} M. The data for sPSO₂-220/ C_{14} TAB mixtures is taken from chapter 5 and for PAMPS/ C_{14} TAB mixtures from the literature.¹⁵

tration of $1 \cdot 10^{-3}$ (mono)M PSS show rather unstable foams for 1:1 ratios. However, there are two essential differences between PSS/ C_{14} TAB and sPSO₂-220/ C_{14} TAB mixtures. Firstly, the adsorbed layer for PSS/ C_{14} TAB mixtures is rather thin, as the absolute surface excess at the 1:1 ratio is only $0.6 - 0.7 \cdot 10^{-6}$ mol/m². The absolute surface excess for sPSO₂-220/ C_{14} TAB mixtures is much higher at $2.5 - 2.8 \cdot 10^{-6}$ mol/m² (as shown in chapter 6). The stronger adsorption of sPSO₂-220/ C_{14} TAB mixtures could lead to higher surface charges (as shown in Fig. 7.9) and hence to more stable foam films. The stronger adsorption also enhances the repulsion between the opposite sublayers as discussed in chapter 6. Secondly, PSS/ C_{14} TAB mixtures show stratification for 1:1 ratios of polyelectrolyte and surfactant. As discussed earlier, stratification can influence the foam film stability and hence makes a quantitative comparison difficult.

For the PSS/ C_{14} TAB mixture the highest foam film stability was found for $2 \cdot 10^{-4}$ (mono)M PSS. The analysis of the surface composition shows that at this concentration rarely any C_{14} TAB adsorbs at the surface, while Γ_{PSS} is approximately $1 \cdot 10^{-6}$ mol/m². The low surface excess of PSS at this concentration indicates a relatively thin polyelectrolyte layer. Hence, it can be assumed that a highly charged monolayer of PSS forms, which stabilizes the foam film through the high amount of negative charges, which are not reduced by positive charges (as rarely any surfactant adsorbed). This is in accordance with the maximum in surface potential for PSS/ C_{14} TAB mixtures shown in Fig. 7.7 and 7.9. Furthermore, for PSS/ C_{14} TAB mixtures no transition from a multilayer to a monolayer

(as for sPSO₂-220/C₁₄TAB mixtures, indicated by the structural data in section 6.3.3) for bulk concentrations around the BSMP was observed. However, a strong decrease of surface excess beyond this ratio was found. This can be contributed to the strong bulk aggregation of the PSS/C₁₄TAB mixture, as discussed earlier.

For PAMPS/C₁₄TAB mixtures the extended framework can be used to rationalize the relative instability of foam films at the BSMP.^{15,71} A large mismatch in polyelectrolyte and surfactant adsorption was found, as Γ_{PAMPS} is quite high at approximately $3.6 \cdot 10^{-6}$ mol/m², while $\Gamma_{\text{C}_{14}\text{TAB}}$ is at $1.2 \cdot 10^{-6}$ mol/m² (see Appendix Fig. 11.9).⁷¹ This mismatch in surface composition indicated a strong negative charge, which should result in a quite stable foam film. The foam film instability found for his PAMPS concentration might be contributed to a strongly disordered structure due to the mismatch in surfactant and polyelectrolyte surface excess adsorbed for this concentration.

For sPSO₂-220/C₁₄TAB mixtures especially stable foam films are found for a surfactant/polyelectrolyte ratio of 1:1, while for mixtures containing C₁₄TAB and PAMPS this ratio was 0.65:1.⁷¹ This difference can be explained by the higher dissociation degree of sPSO₂-220 in comparison to PAMPS, which leads to stronger interaction with the surfactant, and hence to a stronger surfactant adsorption at the surface. Furthermore, the higher rigidity of sPSO₂-220 in comparison to PAMPS leads to less entanglement making the adsorption of more surfactant molecules at the surface possible. This could also explain higher absolute foam film stabilities of sPSO₂-220 in comparison to PAMPS.

Another open question is, if the transition around the BSMP, from a higher surface excess resulting in unstable foam films, to a lower surface excess resulting in stable foam films, is a coincidence or a relevant feature showing the importance of the BSMP? As mentioned the surface composition indicates a similar transition from a strong adsorption (higher surface excess) to a weaker adsorption (lower surface excess) for all polyelectrolytes/C₁₄TAB mixtures. However, for PSS/C₁₄TAB and PAMPS/C₁₄TAB⁷¹ mixtures the transition is shifted to slightly higher polyelectrolyte concentrations. Therefore, it might be concluded that the reason for the earlier transition of sPSO₂-220/C₁₄TAB mixtures below the BSMP, is the higher dissociation degree of sPSO₂-220. This leads to a higher ionic strength, which induces the transition from a higher surface excess to a lower surface excess for lower sPSO₂-220 concentrations. Hence, the reason why for PSS/C₁₄TAB and PAMPS/C₁₄TAB mixtures this transition occurs at higher polyelectrolyte concentration is probably the lower dissociation degree of PAMPS and PSS leading to a lower ion concentration.

In general it could be shown that the foam film stability and surface composition of

polyelectrolyte/surfactant mixtures is depending on a lot of parameters as dissociation degree, polyelectrolyte backbone rigidity or hydrophilic/hydrophobic balance. Despite the differences found in surface composition, it was shown that the extended framework for foam film stabilization developed in chapter 6, also applies to PSS/C₁₄TAB and PAMPS/C₁₄TAB mixtures and that all mixtures show similar trends, e.g. the drop in surface excess around the BSMP. However, structural insight into PSS/C₁₄TAB mixtures (further measurements in D₂O would be needed) and additional polyelectrolyte/surfactant ratios for PAMPS/C₁₄TAB mixtures would further enhance the insight into these complex systems. Moreover, of course the investigation of an additional polyelectrolyte with C₁₄TAB would be useful.

7.4 Conclusion

Possible reasons for the differences in foam film stability between the current and the former work¹⁴ could be that a) in literature the system was not in equilibrium and that b) the originally investigated sample contained small ion impurities. These impurities could have screened the PSS charges and hence decreased repulsive electrostatic interactions, reducing foam film stability.

The dependence of foam film stability on polyelectrolyte concentration found for PSS/C₁₄TAB mixtures differs strongly to that found for sPSO₂-220/C₁₄TAB and PAMPS/C₁₄TAB mixtures. While beyond the BSMP for sPSO₂-220/C₁₄TAB and PAMPS/C₁₄TAB mixtures the foam film stability increases continuously with increasing polyelectrolyte concentration, PSS/C₁₄TAB mixtures show a maximum in foam film stability at $2 \cdot 10^{-4}$ (mono)M and show relatively low constant foam film stabilities afterwards. Furthermore, NR experiments reveal that below the BSMP both PSS and C₁₄TAB adsorb strongly at the air/water interface, while beyond the BSMP the adsorption of both components is much weaker. These findings can be explained by the interaction of the aliphatic chain of the C₁₄TAB and the benzene ring of PSS leading to rather hydrophilic bulk complexes. Hence, both PSS and C₁₄TAB are depleted from the surface, leading to less stable foam films. Furthermore, PSS/C₁₄TAB mixtures show complexation in bulk for comparatively low polyelectrolyte concentrations, leading to stratification which can further influence the foam film stability. Mixtures of PAMPS or sPSO₂-220 with C₁₄TAB show stronger adsorption at the air/water interface, leading to less bulk complexation and thus stratification occurs for much higher polyelectrolyte concentrations.

Chapter 8

Polyelectrolyte backbone rigidity and its influence on structuring in bulk and confinement

Abstract

While in the chapter 5 - 7 the adsorption at the air/water interface and foam film stability were investigated, chapter 8 and 9 focus on the bulk phase. In chapter 5 and 6 it was shown that the polyelectrolyte backbone rigidity has a strong impact on the adsorption at the air/water interface. In this chapter, the influence of polyelectrolyte backbone rigidity on the structuring in aqueous solutions with and without geometrical confinement is determined. The chain structuring of sPSO₂-220 is investigated in confinement with the thin film pressure balance (TFPB) and in bulk with small angle x-ray scattering (SAXS). The current results are compared to findings for the more flexible, but chemically quite similar, polyelectrolyte PSS.¹⁶ The inter-chain distance d is found to be smaller for sPSO₂-220 than for PSS. However, the relative decrease of d with increasing polyelectrolyte concentration is very similar, indicating that sPSO₂-220 forms network-like structures as PSS. The correlation length l_c is found to be smaller and its decrease with increasing polyelectrolyte concentration is significantly steeper for sPSO₂-220 than for PSS. Furthermore, the increase in interaction strength is steeper for sPSO₂-220 than for PSS. In confinement the polymer network of sPSO₂-220 is found to be strongly compressed by 20 - 50 %, in contrast to a compression of only 20 % for PSS.¹⁶

8.1 Introduction

The principles of stratification and structuring of polyelectrolytes in bulk and confinement were introduced in section 2.2.3. The rigidity of the polyelectrolyte backbone is an important factor in the appearance of oscillatory forces/stratification. For typical flexible polyelectrolytes, such as PSS^{16,91} or PAMPS^{84,92,166} with a persistence length l_p of 1 nm, stratification has been observed and extensively investigated. For DNA with a persistence length of 50 nm oscillatory forces were detected neither with a CP-AFM¹⁹ nor with a TFPB¹⁸. Whether stratification occurs or not is assumed to depend on the different rotation times of the polyelectrolyte chains.¹⁸ This parameter is strongly influenced by polyelectrolyte rigidity.¹⁹ TFPB measurements only showed stratification for rigid polyelectrolytes for comparatively high viscosities of the polyelectrolyte solution. Furthermore,

stratification was only observed when the approaching velocity is slow enough. Both findings can be contributed to the fact that the polymer network needs time to adjust so that the network can remain in equilibrium, while it is compressed.¹⁸ However, when stratification occurs the inter-chain distance d seems to be independent of the persistence length.¹⁷ Furthermore, in some work no or only insignificant differences between the characteristic parameters of structuring in confinement vs. bulk were found,^{17,31,32,84,91,92} while in others notable differences (compression up to 20 %) were observed^{16,93,94}.

In this chapter the structuring in bulk and confinement of sPSO₂-220 with an intermediate persistence length l_p of 20 nm was investigated. Furthermore, the viscosity of sPSO₂-220 solutions was determined to investigate the correlation of microscopic (persistence length) and macroscopic properties (viscosity). All current results were compared to earlier findings for PSS.¹⁶ From a chemical point of view PSS and sPSO₂-220 are quite similar, their main differences are the higher dissociation degree and higher persistence length of sPSO₂-220 in comparison to PSS. Therefore, by comparing rigid sPSO₂-220 and flexible PSS further insight into the ordering of polyelectrolytes in dependence of their backbone rigidity could be gained.

8.2 Results

CP-AFM, TFPB and SAXS complement each other in terms of accessible concentration ranges. In CP-AFM measurements a high viscosity can suppress the oscillations and give a significant increase in noise. This is a limiting factor for the quality of oscillatory curves. Especially for concentrations beyond 0.1 (mono)M high viscosities can suppress the oscillations. SAXS can be used to study more concentrated systems, while for lower concentrations (below 0.075 (mono)M) it is not possible to get sufficiently developed peaks with the SAXS system used throughout this study. Using TFPB only information about the inter-chain distance d could be obtained, but these values are especially useful as the measurements can be conducted below the minimum polyelectrolyte concentration of a CP-AFM measurement.

8.2.1 Viscosity measurements

The rheological properties of polyelectrolyte solutions are determined by the configuration of the polyelectrolyte chains relative to each other and are highly dependent on the type

of structuring.¹⁶⁷ The specific viscosity defined as: $(\eta - \eta_s)/\eta_s$ (where η is the measured viscosity and η_s the solvent viscosity) in dependence of polyelectrolyte concentration is shown in Fig. 8.1.

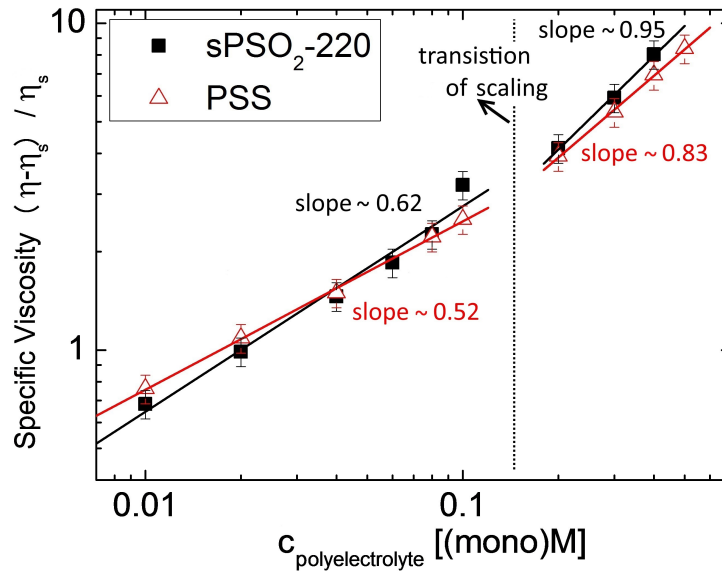


Figure 8.1: Specific viscosity of aqueous sPSO₂-220 solutions in dependence of polyelectrolyte concentration. The solid lines correspond to linear fits in the log scale and the respective slopes are added to the graph. The dotted vertical line separates the two scaling regimes. For comparison the specific viscosity of PSS solutions (extracted from ref. 16) is added.

In the investigated polyelectrolyte concentration range no significant difference in specific viscosity for sPSO₂-220 solutions in comparison to PSS solutions can be seen. Between a polyelectrolyte concentration of 0.1 and 0.2 (mono)M a transition in scaling can be seen for both polyelectrolytes. The increase in viscosity with increasing polyelectrolyte concentration is steeper for sPSO₂-220 ($\eta \propto c^{0.62}$ and $\eta \propto c^{0.95}$), than for PSS ($\eta \propto c^{0.52}$ and $\eta \propto c^{0.83}$) as shown in Fig. 8.1.¹⁶

8.2.2 sPSO₂-220 structuring in bulk

The SAXS spectra for several aqueous sPSO₂-220 solutions are shown in Fig. 8.2 (additional curves are given in the appendix in Fig. 11.10). The data show a maximum in scattering intensity, indicating a near range ordering. With increasing sPSO₂-220 concentration, the maximum scattering intensity I_{max} increases and the position of the peak maximum Q_{max} shifts to higher Q values. From these curves Q_{max} , the full width at half-maximum of the

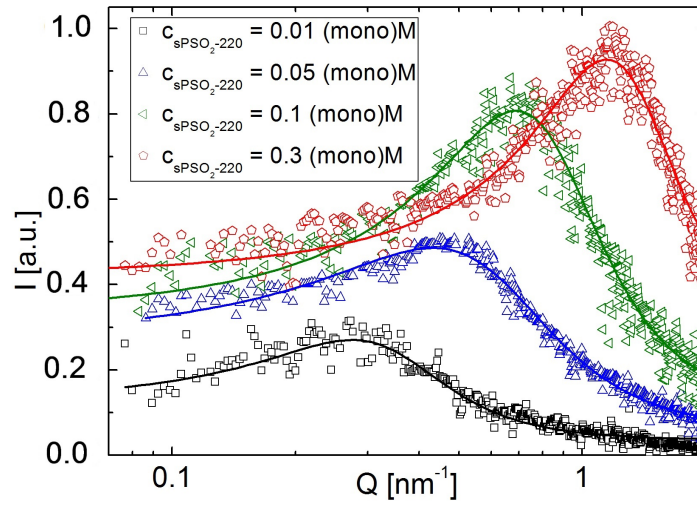


Figure 8.2: SAXS patterns recorded for aqueous sPSO₂-220 solutions. The solid lines represent the Lorentz fits of the curves. For better visibility not all of the recorded curves are shown. The remaining curves can be found in Fig. 11.10 in the appendix.

peak ΔQ and I_{max} were extracted with a Lorentzian fit as described in the literature.^{84,91} The error of the extracted parameters is $\pm 10\%$.

Inter-chain distance d

The inter-chain distance d calculated with $d = 2\pi/Q_{max}$ is plotted versus the concentration of sPSO₂-220 and PSS in Fig. 8.3.

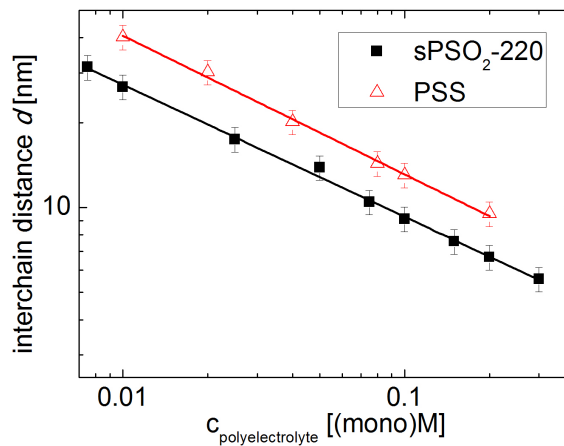


Figure 8.3: Concentration dependence of the inter-chain distance d of sPSO₂-220 solutions extracted from SAXS data. For comparison data for PSS solutions are added (taken from ref. 16). The symbols represent the measured data, while the solid lines correspond to an exponential fit with the slope $d \propto c^{-0.47}$ for sPSO₂-220 and $d \propto c^{-0.49}$ for PSS.

With increasing polyelectrolyte concentration the inter-chain distance d decreases with a dependence of $d \propto c^{-0.47}$ for sPSO₂-220. This decay is close to the decay of $d \propto c^{-0.49}$ for more flexible PSS with a similar molecular weight of 75600 g/mol.¹⁶ It is shown in Fig. 8.3 that at similar concentrations sPSO₂-220 chains are closer together (smaller d) than PSS chains.

Correlation length l_c

The inverse width of the SAXS peak $2/\Delta Q$, which corresponds to the correlation length,^{84,91} is shown in dependence of sPSO₂-220 and PSS concentration in Fig. 8.4. The correlation length l_c gives information about the counter-ion distribution around the chains and the range of chain ordering.

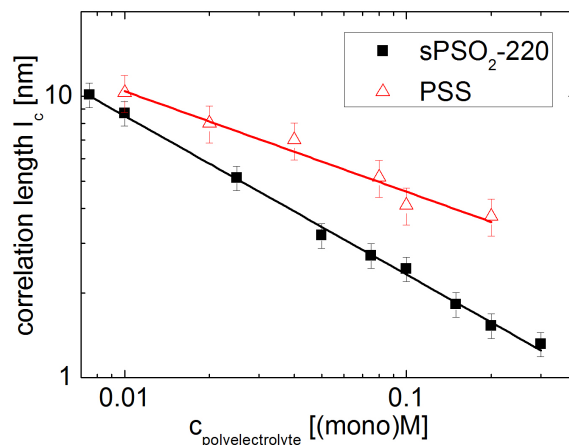


Figure 8.4: Concentration dependence of the correlation length l_c of sPSO₂-220 solutions extracted from SAXS data. For comparison data for PSS solutions are added (taken from ref. 16). The symbols represent the measured data, while the lines corresponds to an exponential fit with the slope $l_c \propto c^{-0.56}$ for sPSO₂-220 and $l_c \propto c^{-0.33}$ for PSS.

With increasing polyelectrolyte concentration l_c of both sPSO₂-220 and PSS decreases. Fig. 8.4 shows that l_c is smaller for sPSO₂-220 than for PSS. Furthermore, the slope of l_c with increasing polyelectrolyte concentration is much steeper for sPSO₂-220 ($l_c \propto c^{-0.56}$) than for PSS ($l_c \propto c^{-0.33}$).

Interaction strength

The maximum scattering intensity I_{max} , which is a measure of inter-chain repulsion, is shown in dependence of sPSO₂-220 and PSS concentration in Fig. 8.5.

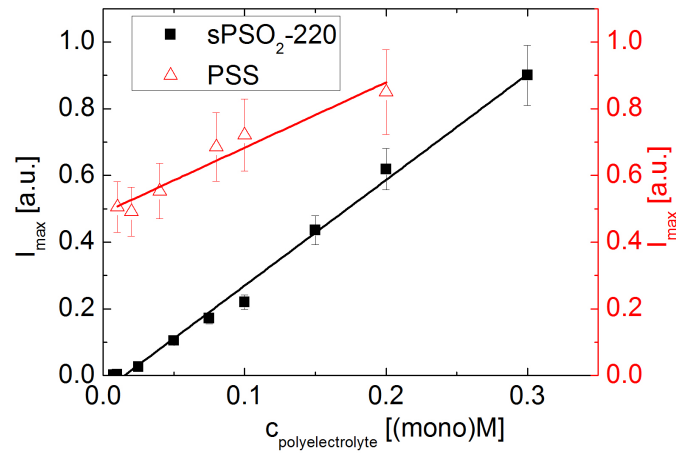


Figure 8.5: Concentration dependence of the maximum scattering intensity I_{max} of sPSO₂-220 solutions extracted from SAXS data. For comparison data for PSS solutions are added (taken from ref. 16). The symbols represent the measured data, while the lines corresponds to a linear fit.

With increasing polyelectrolyte concentration, I_{max} of both polyelectrolytes, sPSO₂-220 and PSS, increases linearly. The slope for sPSO₂-220 is steeper as for PSS. Due to the fact that the available data from PSS are in arbitrary units no absolute I_{max} values can be compared.

8.2.3 sPSO₂-220 structuring in confinement

While for the SAXS measurements pure sPSO₂-220 solutions were investigated, for the TFPB measurements a surfactant has to be added in order to obtain stable foam films. Hence, for every TFPB experiment C₁₄TAB was added, so that the resulting solutions had a constant concentration of 10^{-4} M C₁₄TAB. Disjoining pressure isotherms were recorded and the inter-chain distance d in confinement (corresponding to the step width) was extracted. In Fig. 8.6 a) a disjoining pressure isotherm featuring stratification is shown. Fig. 8.6 b) shows the d at different concentrations of polyelectrolyte.

The inter-chain distance d decreases with increasing sPSO₂-220 concentration with a slope of $d \propto c^{-0.49}$. This is close to the expected slope of $l_c \propto c^{-0.5}$ for network-like structures.⁸³

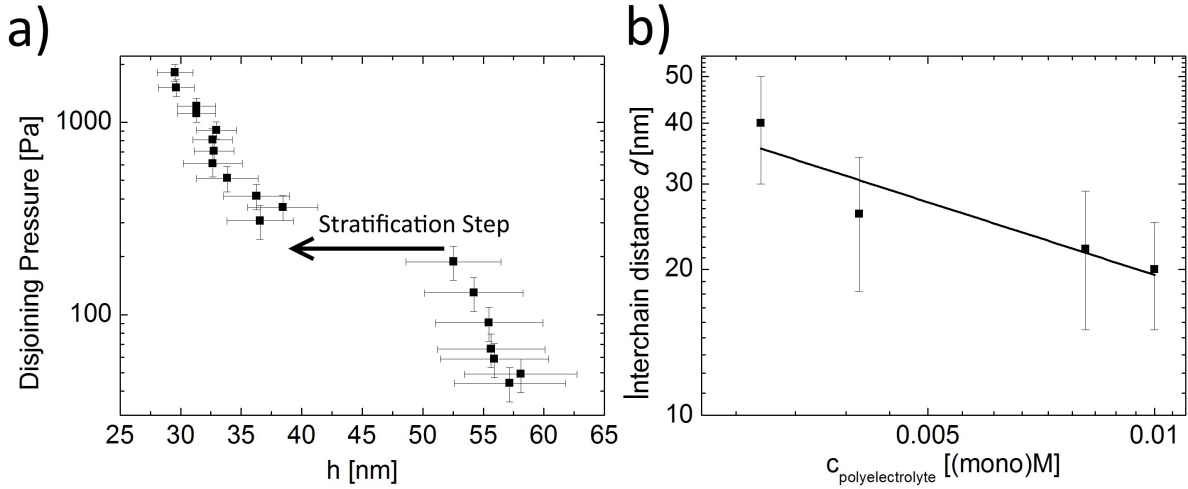


Figure 8.6: a) Disjoining pressure isotherms of a sPSO₂-220/C₁₄TAB solutions with a C₁₄TAB concentration of 10⁻⁴ M and a sPSO₂-220 concentration of 0.01 (mono)M. The arrow indicates the stratification step. For clarity, not all recorded disjoining pressure isotherms are shown. Additional disjoining pressure isotherms can be found in the appendix (Fig. 11.11). b) Concentration dependence of the inter-chain distance d (corresponding to the stratification step width) extracted from TFPB data. The symbols represent the measured data, while the lines corresponds to an exponential fit with the slope $d \propto c^{-0.49}$.

8.3 Discussion

8.3.1 sPSO₂-220 structuring in bulk

Specific Viscosity $(\eta - \eta_s)/\eta_s$

In the investigated concentration range the specific viscosities of sPSO₂-220 and PSS are very close (shown in Fig. 8.1). Thus, the viscosity can not be the origin of the differences in bulk structuring observed for the two polyelectrolyte solutions. For sPSO₂-220 and PSS solutions with polyelectrolyte concentrations below 0.1 (mono)M, the dependence of the viscosity is close to the expected one of $\eta \propto c^{0.5}$ from the literature for the semidilute-unentangled state.^{83,168} However, for polyelectrolyte concentrations beyond 0.1 (mono)M, this dependence becomes significantly higher, suggesting a state between semidilute-unentangled ($\eta \propto c^{0.5}$) and semidilute-unentangled ($\eta \propto c^{1.5}$) structuring.^{83,168} Such a scaling of viscosity with polyelectrolyte concentration between $\eta \propto c^{0.5}$ and $\eta \propto c^{1.5}$ in this regime was observed previously, but to the authors knowledge not yet theoretically explained.^{16,167,168} One possible explanation could be that the transition in scaling between the unentangled- and entangled-semidilute regimes is not a sharp transition but a fluent transition.¹⁶

Inter-chain distance d

Fig. 8.3 shows that for both polyelectrolytes, sPSO₂-220 and PSS, the inter-chain distance d decreases with concentration with a similar dependence of $d \propto c^{-0.47}$ and $d \propto c^{-0.49}$, respectively. That values are close to the value of $d \propto c^{-0.5}$ expected for network-like structures.^{26,83} Furthermore, at similar polyelectrolyte concentrations sPSO₂-220 chains have a smaller d than PSS chains. In the literature it has been shown that, for the same absolute monomer concentration, shorter chains are closer to each other.¹⁶ Here, sPSO₂-220 has a slightly higher molecular weight ($M_w \approx 100000$ g/mol) than PSS ($M_w \approx 75600$ g/mol). Thus, the difference in M_w does not explain the smaller d observed for sPSO₂-220 solutions. Furthermore, sPSO₂-220 has a higher dissociation degree than PSS (54 - 61 % vs. 33 - 38 %),^{127,128} hence one could assume that for sPSO₂-220 the inter-chain repulsion is stronger and in return d is larger. Both facts would indicate the opposite of the observed behaviour.

However, the dissociation degree also leads to a higher ionic strength for sPSO₂-220, which leads to stronger screening of the repulsive charges. For a co-polymer with different degree of charges it was observed that the co-polymers with higher charge fractions were closer to each other.⁸⁴ Hence, larger screening due to higher ionic strength could be a reason for a smaller d for sPSO₂-220 in comparison to PSS. Furthermore, the longer persistence length l_p of sPSO₂-220 in comparison to PSS (20 nm vs. 1 nm)^{17,125} could be the origin of the smaller d . The higher rigidity allows the sPSO₂-220 chains to orientate parallel to each other. That is energetically favorable due to entropic reasons (minimization of the excluded volume).¹⁶⁹ Due to this parallel orientation d is smaller for sPSO₂-220 than for PSS. Moreover, the lower stiffness of PSS could lead a more coiled conformation of PSS or to a pearl-necklace-like polyelectrolyte chain conformation.²⁶ This model describes the formation of blobs of polyelectrolyte chains (peals) connected by uncoiled parts (necklace). This conformation would reduce the effective polyelectrolyte concentration and hence lead to larger distances than for polyelectrolyte chains, which are not in the pearl-necklace chain conformation.²⁶ Due to the higher persistence length coiling or a pearl-necklace conformation is unlikely for sPSO₂-220. However, for PSS the inter-chain distance decreases with $d \propto c^{-0.49}$, which indicates strongly a mesh-like structure and no pearl-necklace structure. Furthermore, for high polyelectrolyte concentrations, which result in chains very close to each other (nm range), van der Waals attractions may start to contribute. van der Waals attractions are larger between parallel chains than for perpendicular or random arrangements of chains, which might further reduce d for higher concentrations sPSO₂-220 in comparison to PSS.¹⁷⁰

and was observed for a co-polymer with different degree of charges in the literature.⁸⁴

Correlation length l_c

With increasing polyelectrolyte concentration the correlation length l_c of both sPSO₂-220 and PSS decreases, which is a result of the increasing counterion concentration. An higher ion concentration leads to an increase in screening, which leads to smaller l_c . This correlation of l_c with polyelectrolyte concentration was also observed in the literature for other systems.^{16,84,91} l_c is smaller and its slope is steeper for sPSO₂-220 than for PSS ($l_c \propto c^{-0.56}$ vs. $l_c \propto c^{-0.33}$). As for d the difference in molecular weight between sPSO₂-220 and PSS does not explain the smaller l_c of sPSO₂-220, as it was shown that longer chains typically have higher l_c .¹⁶ Instead the difference in l_c is probably a result of the difference in dissociation degree, which leads to a larger counterion concentration around the chains for sPSO₂-220 solutions, which leads to larger screening.^{127,128} The similar effect, that higher degree of charges result in smaller l_c , was also observed in the literature for a co-polymer with different degree of charges.⁸⁴ However, it is not clear why the slope of the sPSO₂-220 solution is steeper as the slope of the PSS solution. The mentioned publication shows in general the same slope for all degree of charges.⁸⁴ An explanation could be that with increasing polyelectrolyte concentration the larger dissociation degree of sPSO₂-220 leads to a stronger increase in absolute ionic strength, which screen the repulsive charges to a stronger degree.

Interaction strength

The increase of I_{max} and hence the increase of interaction strength is due to the increasing total charge in the system. The interaction strength between polyelectrolyte chains can be contributed to the competition of electrostatic repulsion between the charges on the chains and the counteracting screening of the counterions. If the electrostatic repulsion dominates the interactions between the chains, as it is the case for highly charged polyelectrolytes as sPSO₂-220 or PSS, this leads to stronger repulsions for higher polyelectrolyte concentrations. The observation of increasing of I_{max} with increasing polyelectrolyte concentration is in accordance with findings in the literature for other polyelectrolytes.^{16,32,84,91} No absolute values can be compared, however the slope for sPSO₂-220 is steeper than for PSS. This might be a result of the higher dissociation degree of sPSO₂-220, which leads to a higher total charge.^{125,127}

8.3.2 Comparison of structuring in bulk and in confinement

To distinguish between the d in bulk and confinement, d_{SAXS} represents the bulk inter-chain distance while d_{TFPB} represents the inter-chain distance in confinement. They are compared to each other in Fig. 8.7.

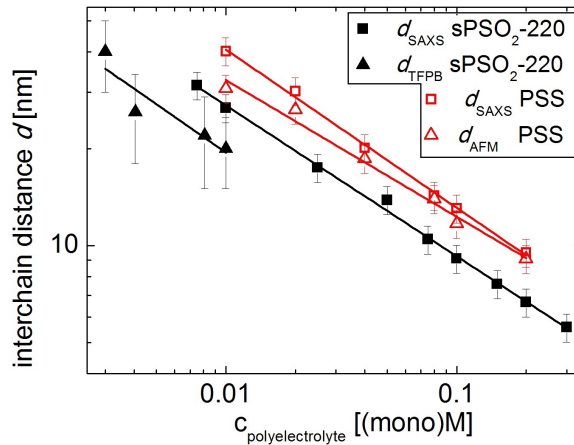


Figure 8.7: The inter-chain distance d_{SAXS} extracted from SAXS data (bulk: squares) and d_{TFPB} extracted from TFPB data (confinement: triangles) in dependence of sPSO₂-220 concentration. The symbols represent the measured data, while the lines corresponds to an exponential fit with the slope $d \propto c^{-0.47}$ in bulk and $d \propto c^{-0.49}$ in confinement. For comparison also data for PSS from the literature is shown.¹⁶ The inter-chain distance d_{AFM} in confinement was extracted with a CP-AFM. For PSS the lines corresponds to an exponential fit with the slope $d \propto c^{-0.48}$ in bulk and $d \propto c^{-0.44}$ in confinement.¹⁶

For sPSO₂-220 the overlap in the concentration range of the two measurement techniques is small. However, the data can be extrapolated to lower/higher concentration and hence be compared. It is shown in Fig. 8.7 that for sPSO₂-220 the inter-chain distance d is 20 - 50 % smaller in confinement than in bulk. A similar compressing influence of confinement was also found in the literature, where measurements with a CP-AFM found the d for PSS to be 20 % smaller in confinement than in bulk.¹⁶

The larger differences between d_{TFPB} with confinement and d_{SAXS} without confinement found for sPSO₂-220, with PSS as comparison, could have different origins. At first the higher rigidity of sPSO₂-220 could lead to a better packing, and hence a smaller inter-chain distance than for PSS, as discussed earlier in this chapter. Secondly, the source could be the different instruments used for the experiments. Using TFPB (sPSO₂-220 experiments) a surfactant has to be added to form stable foam films, otherwise a measurement would not be possible, while in CP-AFM (PSS experiments)¹⁶ the pure polyelectrolyte solution

is investigated. The surfactants of course induce counterions, screening charges and thus could bring the sPSO₂-220 chains closer to each other. Furthermore, the experimental error of a TFPB instrument is higher than for CP-AFM. For further investigations CP-AFM measurements could be useful to broaden the investigated concentration range and additional parameters could be extracted to further elaborate the differences between bulk and confinement. To the authors knowledge, in the literature stratification with rigid polyelectrolytes (DNA and xanthan) was only observed when the viscosity was large. Hence, it was assumed that the polymer network needs time to adjust to be able to show stratification.¹⁸ However, in the investigated polyelectrolyte concentration range in this work no significant difference in viscosity of sPSO₂-220 and PSS solutions was measured. Thus, as stratification was visible, either the former statement is not applicable to sPSO₂-220, or sPSO₂-220 is not rigid enough so that the adjustment time was smaller (with a persistence length l_p of 50 and 150 nm, DNA and xanthan are significantly more rigid).

As already mentioned, in an earlier work no difference in d between the flexible polyelectrolyte PSS and the rigid polyelectrolyte xanthan was found with TFPB measurements.¹⁷ This is in contradiction to the results found here. However, in the mentioned work, PSS/C₁₂TAB mixtures were somewhat arbitrarily compared to xanthan/plantaren (a non-ionic surfactant) mixtures. The molecular weight of both polyelectrolytes was significantly different (M_w [PSS] \approx 70000 g/mol M_w [xanthan] \approx 10⁷ g/mol). The polyelectrolyte concentrations were varied, while the surfactant concentrations were kept constant (at different values, which were different fractions of their respective cmc). Therefore, it is not clear if the fact that no difference in d between PSS and xanthan was detected is due to the difference in persistence length or due to the chemical differences between PSS and xanthan, large differences in their M_w or the differences in the used surfactants. In the present work PSS and sPSO₂-220 are compared, which are chemically similar and have a similar molecular weight (M_w [sPSO₂-220] \approx 100000 g/mol and M_w [PSS] \approx 75600 g/mol). As already mentioned the only differences are the higher dissociation degree and higher persistence length of sPSO₂-220 in comparison to PSS. Furthermore, the same surfactant and the same surfactant concentration was used in the present comparison. Hence, it can be assumed that the present comparison of sPSO₂-220 and PSS is less influenced by external factors than the former comparison of PSS and xanthan in the literature.¹⁷

8.4 Conclusion

The structuring of sPSO₂-220 solutions was studied in a wide concentration range in bulk with SAXS and viscosity measurements and in a confined geometry with TFPB. The results were compared to the more flexible polyelectrolyte PSS with a similar molecular weight.¹⁶ For sPSO₂-220 solutions stratification was detected with the TFPB. The specific viscosity of sPSO₂-220 solutions was quite similar to the specific viscosity of PSS solutions, hence differences in their bulk/confinement structuring must have another reason.¹⁶

The inter-chain distance d decreases with a similar slope of $d \propto c^{-0.47}$ for sPSO₂-220 and $d \propto c^{-0.49}$ for PSS which indicates a network-like structure for both.⁸³ However, for similar concentrations sPSO₂-220 solutions have a smaller d than PSS solutions. This can be explained by the higher rigidity of sPSO₂-220, which leads to a preferred parallel orientation reducing the inter-chain distance. Furthermore, the higher rigidity also leads to less coiling and the higher dissociation degree leads to larger ionic strength and thus stronger screening. Both effects would further reduce the inter-chain distance d . The correlation length l_c is smaller and its slope is significantly steeper for sPSO₂-220 than for PSS ($l_c \propto c^{-0.56}$ vs. $l_c \propto c^{-0.33}$). This is a result of the higher dissociation degree of sPSO₂-220, which leads to a larger ionic strength as for PSS and hence reduces l_c stronger. The increase in interaction strength is steeper for sPSO₂-220 than for PSS, which also corresponds to the higher dissociation degree of sPSO₂-220.

The comparison of sPSO₂-220 structuring in bulk (SAXS) and confinement (TFPB) shows that d is 20 - 50 % smaller in confinement. This value is quite high as for PSS a compression of only 20 % was found.¹⁶ Up to now it is not clear whether this is due to measurement limitations or whether this is a relevant physical finding (e.g. a consequence of a more effective parallel ordering). CP-AFM experiments could be helpful to get further information on the compressing influence of confinement.

Chapter 9

Two-Dimensional aggregation and semi-dilute ordering in cellulose nanocrystals*

Abstract

In this chapter, carboxymethylated CNC (CNC-COOH) were examined using SANS, TEM, AFM and DLS to elucidate the CNC aggregation behavior on the microscale and the ordering of CNC aggregates into liquid crystal like arrangements on the mesoscale. The results from CNC-COOH were compared to the standard system of sulfuric acid hydrolyzed CNC (CNC-SO₃H). By using a well-characterized system of single carboxymethylated CNFs as starting material for the CNC hydrolysis similar cross sectional dimensions for CNC-COOH and CNC-SO₃H (a width to height ratio of 8) were found while CNC-COOH has a factor of 2 larger length. Furthermore, an unexpected lateral organization of the CNC into 2D aggregates was discovered. The aggregates were stable in dispersion and resisted drying when adsorbed to surfaces. With increasing concentration the 2D aggregates further showed a liquid crystal like ordering and dilution of the 2D aggregates demonstrated that this ordering was reversible. Both systems were found to show bulk structuring at concentrations in the lower range of the semi-dilute regime. This indicates the onset of a liquid crystalline arrangement at concentrations below those where bulk-ordering features such as birefringence or tactoids can be observed using polarized optical microscopy. The data presented here demonstrates that specific structuring occurs between single CNC particles, and the observation that the formed 2D aggregates order in liquid crystal like phases indicates that the 2D aggregation may be an intermediate structure in the formation of the CNC chiral nematic phase.

9.1 Introduction

Cellulose nanocrystals (CNC) are rod-like particles, which are soluble in aqueous solutions due to the repulsive interactions of charged groups at the surface. As follows, CNCs possess both similar and differing properties to the polyelectrolytes investigated in the previous chapters of this thesis. A difference is that CNCs are rod-like particles consisting of many ordered cellulose macromolecules while polyelectrolytes are single chain molecules,

*Similar content was presented in M. Uhlig, A. Fall, S. Wellert, M. Lehmann, S. Prévost, L. Wågberg, R. von Klitzing and G. Nyström *Langmuir*, **2016**, *32*, 442 - 450

ordering or aggregating only under certain circumstances (high concentrations or salt addition, respectively). A similarity is that both are stabilized in aqueous solutions by the repulsive interactions of their charged groups. Hence, CNCs can be understood as rigid rod-like aggregates of polyelectrolytes and thus this chapter enhances the investigation of rigid polyelectrolytes from the previous one. In this chapter the focus is on investigating the shape and structural properties of CNC which are a result of the type and strength of CNC charges.

Different techniques, such as atomic force microscopy (AFM)^{107,112}, transmission electron microscopy (TEM)^{108,110,113} and small angle scattering (SAS)^{106,107,111,171–173} have been used to characterize the size parameters of CNC. Small angle scattering with neutrons (SANS) showed that CNC has a rectangular cross-sectional shape^{107,171,173} and that, depending on the cellulose source, size parameters can differ significantly^{106,107}. Small angle scattering with X-Rays (SAXS) showed that also carboxylated cellulose nanofibrils (CNF) can have a rectangular cross section¹⁷². These studies are mainly focused on the properties of the single cellulose particle. Structural studies of the interaction between particles and aggregation behavior exist^{106,173,174} but are more rare. To conclude, studies investigating the influence of preparation route on both the shape and structural properties of CNCs are missing.

The aim of this chapter is to analyze the structural properties and aggregation behavior of carboxymethylated cellulose nanocrystals (CNC-COOH) and compare it to sulfuric acid hydrolyzed cellulose nanocrystals (CNC-SO₃H). To get an complete picture of the systems several complementary techniques as small angle neutron scattering (SANS), transmission electron microscopy (TEM), atomic force microscopy (AFM) and dynamic light scattering (DLS) were used.

9.2 Results

9.2.1 TEM analysis of CNC

For both CNC-COOH and CNC-SO₃H, TEM images were recorded (Fig. 9.1), where the rod-like shape of both types of CNCs is clearly visible.

CNC-COOH crystals are longer and show kinks while CNC-SO₃H crystals are shorter and kinks were not found for this sample. For both types of CNC, aggregates of nanocrystals can be seen. The TEM images were used to extract the length of the nanocrystals. For

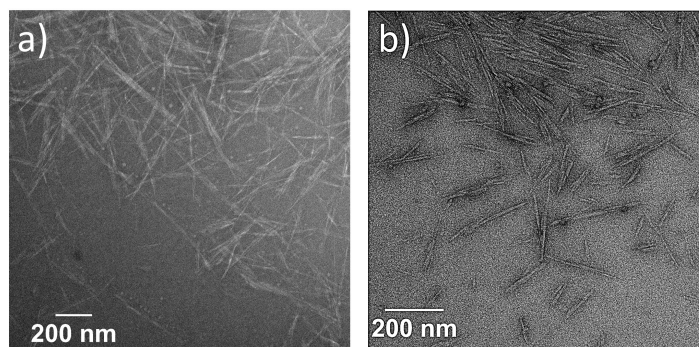


Figure 9.1: TEM images of a) CNC-COOH and b) CNC-SO₃H. This data was recorded by Maren Lehmann (experimental details are given in ref. 133).

the length evaluation 250 single crystals of each type were evaluated. The resulting length distribution are shown in Fig. 9.2.

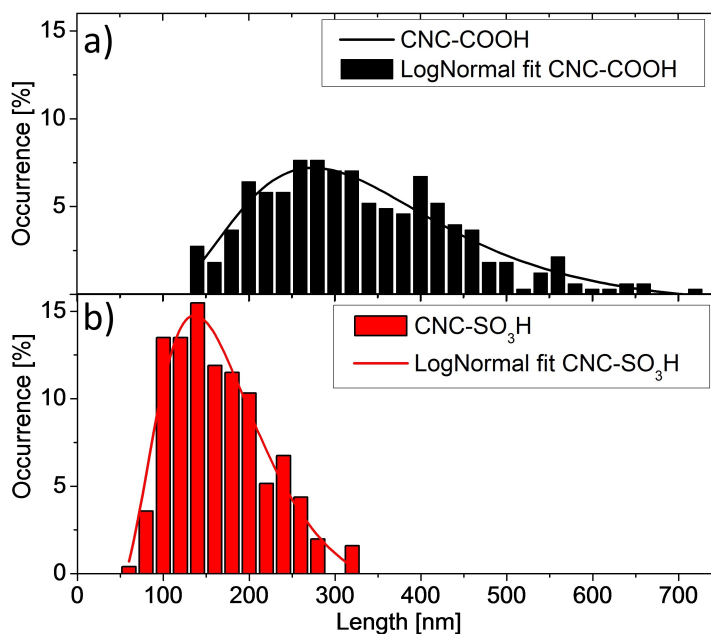


Figure 9.2: Distribution of crystal lengths extracted from TEM images for a) CNC-COOH and b) CNC-SO₃H.

The Log-normal distribution was used to describe the polydispersity of the system. Here μ is the location parameter and σ is the scale parameter.

$$f(x) = \frac{1}{(\sqrt{2\pi}\sigma x)} e^{\frac{(-\ln(x)-\mu^2)}{(2\sigma^2)}} \quad (9.1)$$

Furthermore, the following equation was used for the extraction of the mean value.

$$x_{mean} = e^{\mu + \frac{\sigma^2}{2}} \quad (9.2)$$

By fitting the extracted length data to the Log-normal distribution function in eq. 9.1 the following fit parameters were found: for CNC-COOH $\mu = 5.705$ and $\sigma = 0.42$ and for CNC-SO₃H $\mu = 5.003$ and $\sigma = 0.426$ corresponding to average lengths of 328 nm for CNC-COOH and 163 nm for CNC-SO₃H.

9.2.2 SANS from CNC

SANS was used to get ensemble average structural information about the individual crystal morphology (from semi-dilute dispersions) as well as their arrangements in liquid crystal assemblies (from concentrated dispersions). SANS was performed for the CNC-COOH samples in the concentration range 1 - 30 g/L and for CNC-SO₃H samples in the concentration range 2 - 46 g/L. A two-step fitting process was used to analyze the scattering data. At first the data were fitted for high Q values ($Q \geq 0.7 \text{ nm}^{-1}$) with the long cylinder model:¹⁷⁵

$$F(Q, R, L) = (\delta\eta R^2 L)^2 \frac{2}{QL} \cdot \left\{ Si_{\frac{\pi}{2}}(QL) \Lambda_1^2(QR) - \frac{\omega(2QR)}{QL} - \frac{\sin(QL)}{(QL)^2} \right\} \quad (9.3)$$

with

$$Si_{\frac{\pi}{2}} = \left(Si(x) + \frac{\cos x}{x} + \frac{\sin x}{x^2} \right) \xrightarrow{x \rightarrow \infty} \frac{\pi}{2} \quad (9.4)$$

and

$$\omega(x) = \frac{8}{x^2} (3J_2(X) + J_0(x) - 1) \quad (9.5)$$

where $J_n(X)$ is the cylindrical Bessel functions of order n . R is the radius of the rod, L the length of the rod, δ the difference between scattering length density (SLD) of the solvent and CNC and Q the scattering vector. This model is applicable, as the length of the cylinder is more than twice the radius of the cylinder ($L \geq 2R$). The extracted length from the TEM analysis was used in the calculations, given that the maximum observable dimension in these SANS data, limited by the lowest Q value, is around 200 nm

(ca. $2 \Pi/Q_{min}$).⁹⁰ Thus, at least the CNC-COOH length would not be extractable. For both CNC-COOH and CNC-SO₃H a SLD of $1.96 \cdot 10^{10} \text{ cm}^{-2}$ was used. This SLD was calculated with the SLD calculator of the SASfit software¹⁵⁰ using the chemical structure of cellulose (C₁₂H₂₀O₁₀) and the density 1.676 g/cm³.⁹⁶ The residual volume fraction of light water was determined by comparing the incoherent backgrounds of samples to those of D₂O/H₂O mixtures with known composition. The resulting solvent SLD was calculated accordingly. The fitting resulted in a radius R of 1.3 nm for CNC-COOH and 1.6 nm for CNC-SO₃H. To describe the size distributions the Log-normal distribution function (eq. 9.1) was used again. For CNC-COOH $\mu = 0.15$ and $\sigma = 0.51$ and for CNC-SO₃H $\mu = 0.44$ and $\sigma = 0.22$ were found. The resulting size distributions are shown in Fig. 9.3.

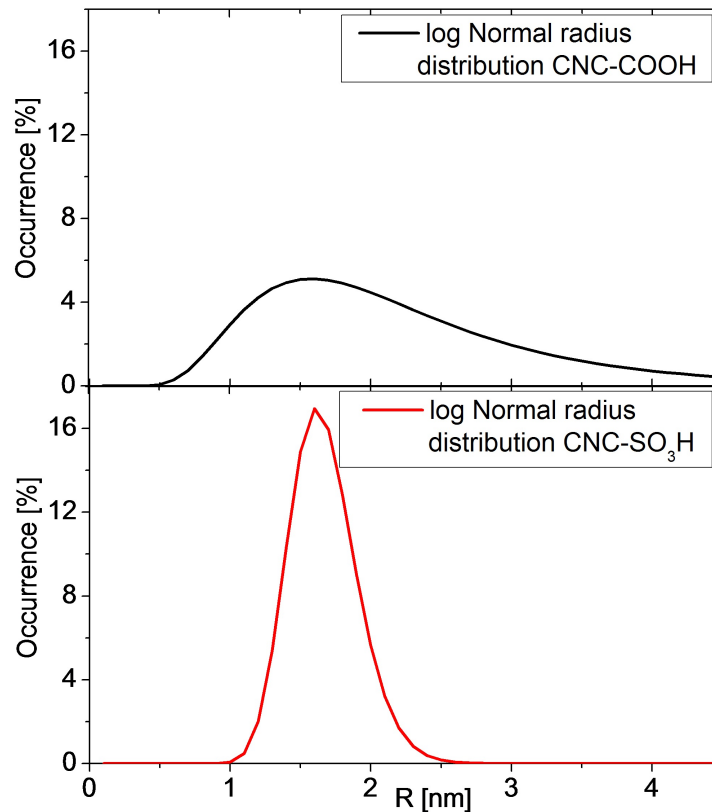


Figure 9.3: Distribution of crystal radii extracted from SANS curves for a) CNC-COOH and b) CNC-SO₃H.

For CNC-COOH the size distribution of the radius is broader than for CNC-SO₃H. Moreover, this model was used to investigate the aggregation behavior of the nanocrystals. As mentioned, in the TEM images, aggregation of single nanocrystals to larger fractal structures was observed (Fig. 9.1) for both nanocrystals types. As follows, for high Q values the structure factor of fractal aggregates was added¹⁵⁰, making it possible to extract the dimension of the aggregates. Here, a value of 2 would correspond to 2D-aggregation

and a value of 3 would correspond to 3D-aggregation. The fitting resulted in a dimension of 2.05 for CNC-COOH and 2.1 for CNC-SO₃H (mainly 2D aggregation), which is also in accordance with the observations from the TEM images.

To get a deeper insight into the shape of both CNC-COOH and CNC-SO₃H, for low and intermediate Q the parallelepiped model was used.¹⁷⁶ High Q values were not included in the fit, as due to the polydispersity the model fails to describe this range. Earlier reports have shown the applicability of the model for CNCs.^{173,177,178}

$$F(Q) = \left[\frac{\sin(Q_x a/2)}{Q_x a/2} \right] \left[\frac{\sin(Q_y b/2)}{Q_y b/2} \right] \left[\frac{\sin(Q_z c/2)}{Q_z c/2} \right] \quad (9.6)$$

The parallelepiped model uses the following parameters: the height a , the width b and the length c . Again, the extracted length from TEM was used and as a starting parameter for the aggregate height a , $2R$ from the first model was used. In this analysis, the fitted value b corresponds not to the width of a single crystal, but the width of a crystal aggregate. In Fig. 9.4 the scattering data and corresponding fits for CNC-COOH and CNC-SO₃H at different CNC concentrations are shown. For enhanced clarity, not all recorded SANS curves are shown, additional curves for CNC-COOH can be found in the appendix (Fig. 11.12). In Table 9.1 the results from the fits are listed.

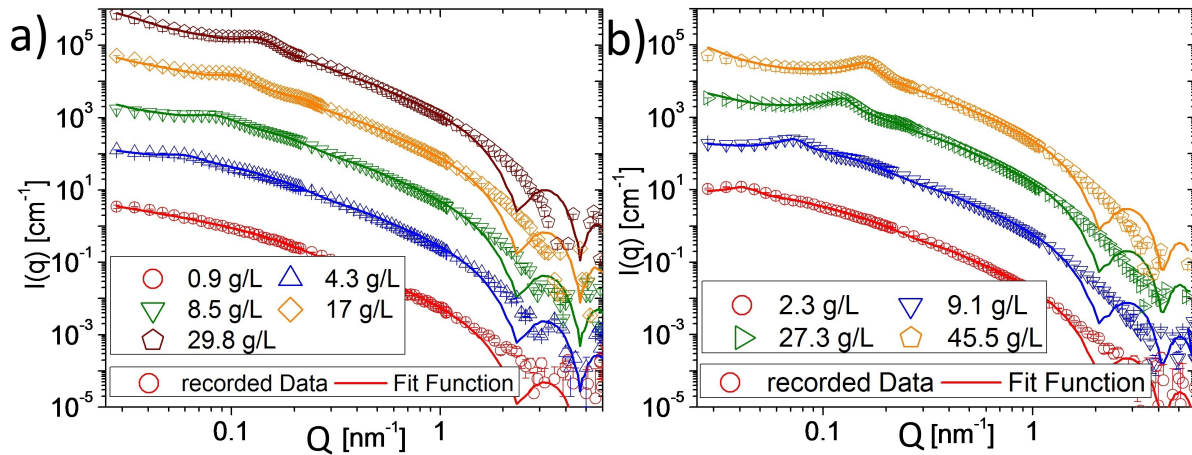


Figure 9.4: SANS curves recorded for a) CNC-COOH and b) CNC-SO₃H. For better visibility the curves are incrementally shifted by a factor of ten. The lowest concentration curve is in absolute scale.

As predicted the fits describe the recorded data very well for low and intermediate Q values, while for high Q values the fit to the data is poor.

| Nanocrystal type | aggregate height a | aggregate width b | length c | $[b/a]$ aggregation number |
|-----------------------|----------------------|---------------------|------------|----------------------------|
| CNC-COOH | 2.7 nm | 21.7 nm | 328 nm | 8 |
| CNC-SO ₃ H | 3 nm | 24.4 nm | 163 nm | 8 |

Table 9.1: Extracted size parameters from the fits (length c from TEM).

9.2.3 AFM analysis of CNC

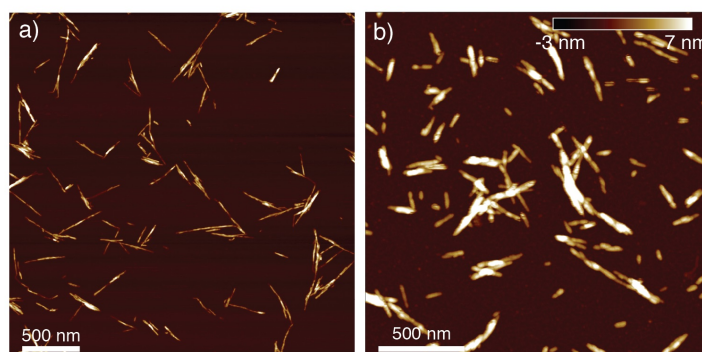


Figure 9.5: AFM images of a) CNC-COOH and b) CNC-SO₃H. This data was recorded by Jozef Adamcik and Sebastian Schön (experimental details are given in ref. 133).

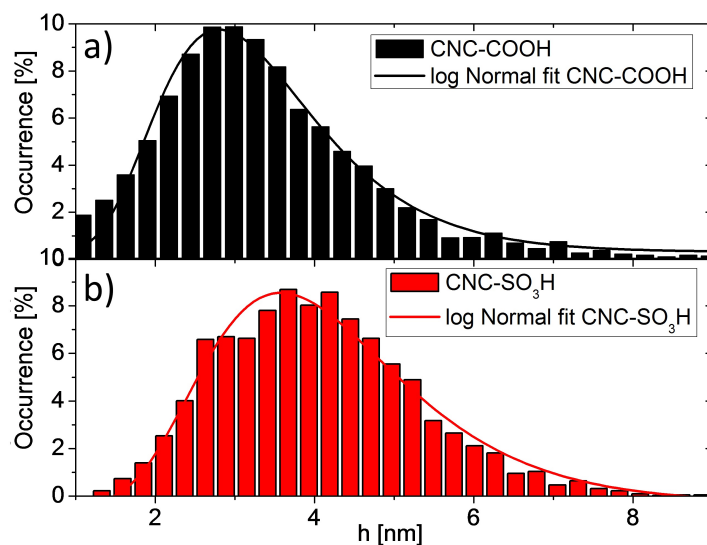


Figure 9.6: AFM height distributions from individual CNCs of a) CNC-COOH b) CNC-SO₃H fitted with a log-normal distribution function. From the fit an average CNC height of 3.2 nm was found for CNC-COOH and 4.0 nm for CNC-SO₃H.

To investigate the 2D aggregates found in TEM and SANS further, AFM was performed (Fig. 9.5). In the obtained images, individual CNC as well as CNC aggregates were found. Based on image analysis¹⁷⁹ of 300 individual CNCs, the CNC height distributions of CNC-COOH and CNC-SO₃H were extracted (Fig. 9.6), where all height coordinates (points)

along the analyzed CNCs have been plotted. Similarly as for the length distributions, the height data can be well described using a log-normal distribution function. For CNC-COOH $\mu = 1.1$ and $\sigma = 0.35$ and for CNC-SO₃H $\mu = 1.33$ and $\sigma = 0.34$ was found. This gives an average CNC height of 3.2 nm for CNC-COOH and 4.0 nm for CNC-SO₃H. These values are in good agreement with the aggregate thicknesses obtained in the SANS analysis. In the AFM data, CNC aggregates as well as clusters of CNC aggregates are also visible (shown in the appendix in Fig. 11.15). Height profiles across these aggregates reveal a flat conformation of the CNC in the aggregates. However, since the presence of artifacts related to AFM tip broadening¹⁸⁰ cannot be ruled out, the exact lateral dimensions of these aggregates was not quantified using AFM data.

9.2.4 Interactions between CNC aggregates

For samples with a higher concentration a peak in the scattering data was visible (Fig. 9.4). For fully randomly oriented anisotropic CNC aggregates (as in the dilute scattering described above) no peak would be expected, since the peak results from a high probability of a given distance d (equation 9.7) between the scatterers.

$$d = \frac{2\pi}{Q_{max}} \quad (9.7)$$

As the CNC aggregate concentration is increased, the aggregates start to interact and a peak is developed at the scattering vector Q_{max} , corresponding to the most probable inter-aggregate distance d . The sharper this peak is, the better defined is the order between the aggregates and very sharp peaks are indicative of liquid-crystal-like ordering. So far, there is no model to describe the structure contribution of long rigid rods. Thus, the modified Caillé model¹⁵⁰ was used to describe the structure contribution at higher concentrations (for the fits in Fig. 9.4). The modified Caillé model is normally used to describe disorder due to fluctuations in multilamellar structures. Thus, it can be only used to qualitatively extend the fit to include the structure contribution. No quantitative information could be extracted from this contribution to the fit. Therefore, the peak was evaluated by dividing the recorded curve (equation 9.8) by the form factor (up-scaled from lower concentrated curves which do not show a structure contribution).

$$S(Q) = \frac{I(Q)}{F(Q)} \quad (9.8)$$

Thus, only the structure factor remained (shown in appendix Fig. 11.16 for CNC-COOH and Fig. 11.17 for CNC-SO₃H), which was evaluated with a Lorentzian fit (equation 9.9).⁸⁴

$$I(Q) = \frac{I_l}{(Q - Q_{max})^2 + (\Delta Q/2)^2} + I_0 \quad (9.9)$$

Here I_0 is the incoherent background, I_l is the incident beam intensity, Q_{max} is the peak position, and ΔQ is the full width at half-maximum of the peak. An example for such a Lorentz fit is shown in Fig. 9.7.

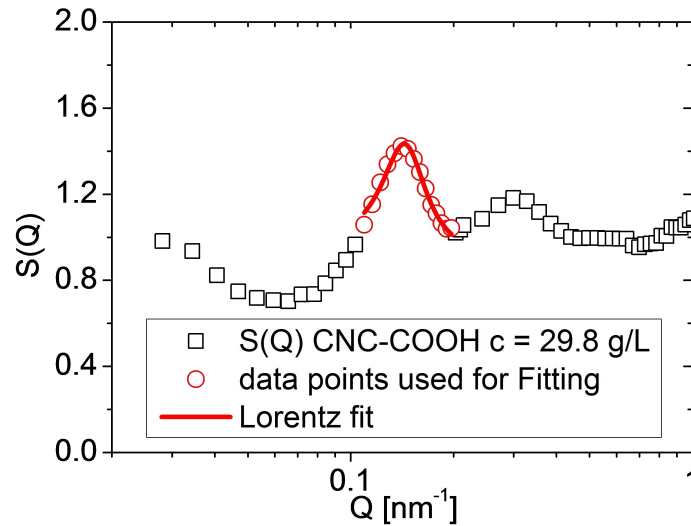


Figure 9.7: An Example of the Lorentz fit to extract Q_{max} .

Fig. 9.8 shows the evolution of the inter-aggregate distance (calculated with equation 9.7) as a function of increasing CNC aggregate concentration and aggregate number density.

CNC-SO₃H already shows structuring for low concentrations (above 2 g/L) while CNC-COOH starts to show structuring at slightly higher concentrations (above 4 g/L), shown in Fig. 9.4 and Fig. 9.8 a). The intermediate distance between aggregates is smaller for CNC-COOH than for CNC-SO₃H. For higher concentrations the intermediate distance become more similar. Rescaling the concentrations to aggregate number densities (Fig. 9.8 b)) shifts the CNC-COOH data points relative to the CNC-SO₃H data and demonstrates that the onset of structuring occur at the same aggregate number density for both samples. At the same time, the difference in inter-aggregate distance becomes larger at similar aggregate number densities. The plotted inter-aggregate distances versus aggregate number density satisfies a power law ($d \propto n^\alpha$) with exponential decay factors $\alpha = -0.37$ (CNC-COOH)

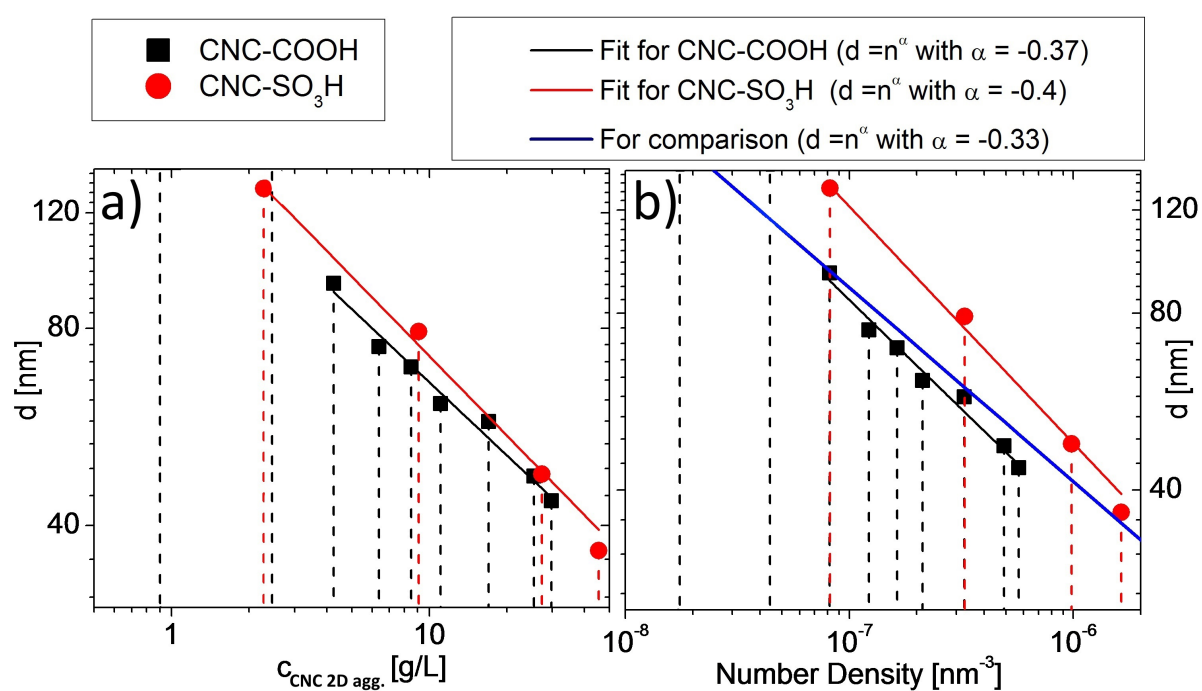


Figure 9.8: Inter-aggregate distance d extracted from Q_{max} of the structure peaks plotted as a function of a) aggregate concentration and b) aggregate number density. The solid lines are fits to the data. The dotted lines represent all measured concentrations, thus concentrations which did not show a structure contribution could be identified.

and $\alpha = -0.4$ (CNC-SO₃H). For comparison a line corresponding to $\alpha = -1/3$ as expected from space filling arguments (calculated in appendix section 11 and discussed in section 2.2.3 and 9.3.2) has been added.

9.2.5 DLS analysis of CNC

As a complement to the SANS measurements, dynamic light scattering was performed for the CNC-COOH samples in the concentration range 5 - 23 g/L. Fig. 9.9 shows the relative hydrodynamic diameter D_h extracted from the measurements through the translational diffusion coefficient, D_t , (which is in turn obtained from the scattering autocorrelation function) using the Stoke-Einstein equation assuming, for simplicity, a spherical CNC aggregate shape:

$$D_h = \frac{k_B \cdot T}{3\pi \cdot \eta \cdot D_t} \quad (9.10)$$

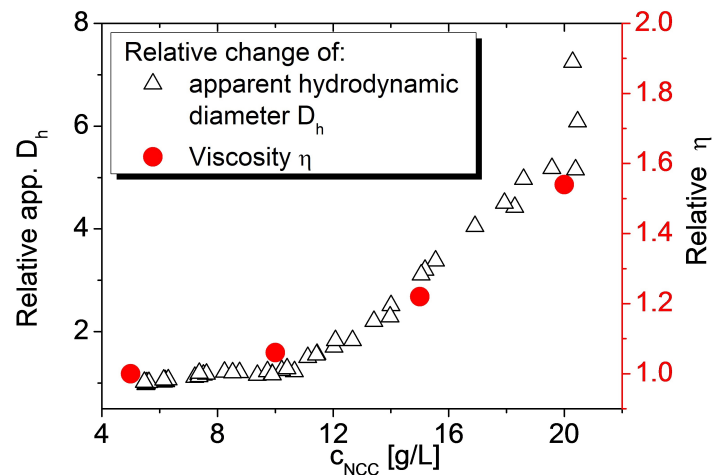


Figure 9.9: Relative change in apparent hydrodynamic diameter D_h and viscosity η as a function of concentration obtained from DLS measurements of CNC-COOH. This data was recorded by Andreas Fall (experimental details are given in ref. 133).

It can be seen that the apparent hydrodynamic diameter is relatively unchanged until a concentration of 10 g/L, where it starts to increase. As a control experiment, the viscosity of the CNC-COOH dispersion was also measured and the result was plotted as relative values in Fig. 9.9. These results show a small increase of the dispersion viscosity. As the CNC aggregate concentration is increased to 20 g/L, the relative viscosity increases by a factor of 1.54 compared to the viscosity at 5 g/L.

9.3 Discussion

9.3.1 Shape of CNC aggregates

Only minor differences in the CNC-COOH and CNC-SO₃H cross sections (shown in Table 9.1) are noticeable. The CNC-COOH nanocrystals are slightly thinner and their size distribution is broader compared to CNC-SO₃H. The two types, however, strongly differ in nanocrystal length (as shown in Fig. 9.1 and 9.2). The observed differences could possibly be traced back to the different cellulose sources used for the CNCs or the less aggressive reaction conditions used for CNC-COOH preparation compared to CNC-SO₃H preparation.^{109,181} While the chiral nematic ordering of the shorter CNC-SO₃H crystals can be used for photonic materials⁹⁸, the resulting increase in aspect ratio for CNC-COOH may be desirable for applications in biocomposites^{182,183}. The CNC-COOH height and length parameters extracted in this study are comparable to earlier reported values, using similar reaction conditions and measured by AFM.¹¹²

Carboxylated CNC and sulfuric acid hydrolyzed CNC were also recently compared with a focus on the resulting properties in nanopaper.¹⁸³ Here, an average length/diameter of 200.7/5.8 nm was found for carboxylated CNC and 163.0/15.6 nm for sulfuric acid hydrolyzed CNC. The longer length of carboxylated CNC was also observed in in this work (shown in Table 9.1). However, here quite similar cross sections for both CNC types (2.7 · 21.7 nm for CNC-COOH vs. 3 · 24.4 nm for CNC-SO₃H, shown in Table 9.1) and a smaller width distribution for CNC-SO₃H than for CNC-COOH (shown in Fig. 9.2) were observed. While this presents a relative comparison between the two systems, it is important to note that in general for CNCs the absolute size parameters are hardly comparable for different cellulose sources, reaction conditions and measurement techniques.¹⁸⁴ With TEM, or low-resolution AFM images, aggregates of CNCs can also easily be mistaken for single CNCs.

Here, lateral CNC aggregation based on both sample averaging scattering data (CNCs in dispersion) and AFM analysis (CNCs adsorbed to a surface) was observed. The formed aggregates are flat and do not possess a detectable twist, as might be expected based on the observation of a right-handed twist of individual cellulose fibrils.¹¹⁸ From the AFM images it is clear that there is furthermore a tendency for the CNC aggregates to arrange laterally when adsorbed on a surface (as shown in Fig. 11.15 in the appendix). To minimize the risk that drying effects influence the lateral organization, the CNCs were electrostatically immobilized on the surface (APTES-modified mica). The lateral

arrangement indicates that the surface properties of the sides of the individual CNCs could be different. Cellulose has a crystal structure where the polymer chains are oriented in a flat planar organization along the particles long direction.⁹⁶ This suggests that the hydroxyl groups, which are all oriented parallel to the crystalline cellulose planes, can create two sides that are more polar than the two sides of the particle that are oriented perpendicular to the crystalline planes.^{185,186} Thus, it is possible, that the less polar sides of two neighboring particles orient towards each other, thereby exposing more of their hydrophilic sides to the surrounding water and minimizing their free energy.

SAXS of CNF and SANS of CNC have shown that the width of the cellulose nanoparticles can be ~ 4 times larger than their height.^{172,173} This should be compared to the factor ~ 8 larger width to height of the 2D CNC aggregates in the present study. Aggregation of single nanocrystals into larger aggregates has also been previously observed.^{106,173} Two ways to reduce CNC aggregation can be to use more strongly charged cellulose or to use longer ultra sonication times, but this also has been shown to damage the nanocrystals.¹⁰⁸

In the case of CNC-COOH, the synthesis was started from a well characterized system of carboxymethylated cellulose nanofibrils (CNF-COOH)¹⁸⁷, with a mean height of 2.5 nm in good agreement to the height parameter of the CNC-COOH aggregates (shown in Table 9.1 and appendix: AFM image (Fig. 11.13) and crystal height distribution (Fig. 11.14) of this material) as well as previously reported values reported height values of 3.5 - 4 nm.^{174,188}

The known nanometer structure of the CNF-COOH starting material offers, unlike the CNC-SO₃H synthesis where the source material is several micrometers in all dimensions, a direct link between the structure of the source material and the final CNC-COOH structure. As a first approximation the interaction between the individual CNCs can be described, using the DLVO theory,^{189,190} as the sum of a repulsive electrostatic potential and an attractive van der Waals potential. During the HCl hydrolysis, the pH is drastically lowered eliminating the electrostatic repulsion between the fibrils. Without the electrostatic repulsion the fibrils are forced to close proximity by van der Waals attraction. Simultaneously, the acid hydrolyses the fibrils and thereby decreases their length. Since the van der Waals attraction is larger for parallel than for perpendicular arrangements of rods,^{169,170} a lateral particle aggregation is energetically favorable. Following hydrolysis, the pH is again increased and the CNCs have regained their surface charge. Most likely, the mechanical energy (sonication) that is subsequently used to liberate the CNCs is not sufficient to fully separate the aggregates into free CNCs, and rather aggregates of CNCs are dispersed.

This explanation model could, combined with the previously mentioned crystal structural argument, offer a qualitative understanding of the observed lateral aggregation behavior.

9.3.2 Interactions between CNC aggregates

At the lowest CNC concentrations the SANS data reveals no structuring in the samples and the scattering is only based on the form factor of the CNC aggregates. As the CNC concentration increases, however, both CNC samples show structure peaks indicating an ordering (shown in Fig. 9.4). For CNC-SO₃H structure formation starts at a lower crystal mass concentration. Furthermore, for CNC-COOH the distances at similar concentrations are smaller (Fig. 9.8). At the onset of ordering the CNC aggregates are at average distances of ~ 90 nm (CNC-COOH) and ~ 130 nm (CNC-SO₃H) from each other.

Based on the total ionic concentration, estimated from the counterion concentrations, (1.4 - 11 mM for CNC-COOH and 0.7 - 14 mM for CNC-SO₃H at low and high aggregate concentration respectively) it can be noticed that both crystals are at distances farther away than their Debye lengths ($\kappa^{-1} \sim 3 - 8$ nm for CNC-COOH and $\kappa^{-1} \sim 3 - 12$ nm for CNC-SO₃H, calculation details in appendix section 11). Here, the electrostatic interaction between the CNC aggregates might not be primarily controlling this structuring, and instead steric arguments can be used to explain the observed differences in inter-aggregate distances. Both 2D aggregate types are in the semi-dilute concentration range, i.e. above the overlap concentration, and at average distances shorter than their length (shown in appendix section 11 for calculation details). They will therefore have a steric influence on their surrounding aggregates and there will be an entropic driving force favoring a parallel orientation of the aggregates (minimizing the excluded volume). Based on the larger aggregate size of CNC-COOH, compared to CNC-SO₃H, and by taking into account the concentration differences at the onset of ordering, a smaller average inter-aggregate distance could therefore be expected. This corresponds well to the experimental observations. The effect is even more pronounced when the aggregate concentration is re-scaled to CNC aggregate number densities (Fig. 9.8 b)). From the larger aspect ratio, of CNC-COOH compared to CNC-SO₃H, one would actually also expect the onset of structuring to occur at a lower CNC aggregate concentration for the CNC-COOH. This is not observed in the experiments. A possible reason could be the larger polydispersity observed for the CNC-COOH crystals (Fig. 9.2 and 9.3). A larger polydispersity decreases the driving force which assembles the CNC into ordered structures.¹⁹¹ The inter-CNC aggregate distances

reported here at higher CNC concentrations (Fig. 9.8, above 20 g/L) are also in good agreement with those previously reported for similar CNC concentrations.¹⁷⁸

So far previous reports in literature have only shown weak¹¹¹ or no structuring^{171,173} at CNC concentrations in the range 7.8 - 13.7 g/L. While a direct comparison to previous experimental studies is difficult because of the many experimental differences, the results presented here may be the first report of structure formation in the low range of the semi-dilute regime for cellulose nanocrystals.

The power law decay in inter-aggregate distance is slightly steeper for CNC-SO₃H ($\alpha = -0.4$) than for CNC-COOH ($\alpha = -0.37$). In general a scaling of $-1/3$ is characteristic for particles using simple space filling arguments in three dimensions (shown in detail in the appendix section 11). A deviation from this slope would indicate a clustering of the aggregates. For instance a slope of $-1/2$ is characteristic for entangled polyelectrolyte systems.^{16,26} Both scalings are close to the theoretical value (Fig. 9.8) indicating that mainly space filling packing of aggregates and not clustering takes place.

Finally, DLS was used to monitor the relative aggregate size, based on the apparent hydrodynamic diameter D_h , as a function of increasing CNC aggregate concentration for the CNC-COOH system (Fig. 9.9). From these measurements, it was concluded that the aggregate size remain relatively unchanged in the concentration range 5 - 10 g/L. This suggests that the observed early structuring is a bulk structuring of the aggregates and not a result of the arrangement of the aggregates into clusters. Above 10 g/L D_h increases, indicating formation of clusters of the aggregates. The rheology of CNC-COOH was investigated, as a control experiment, and verified that the observed increase in D_h was not an effect of an increase in viscosity. The measurement showed only a factor 1.54 increase in viscosity compared to a 5 - 8 times observed increase in D_h . This supports the conclusion that a relative increase in aggregate cluster size is observed for concentrations above 10 g/L. The concentration range of the onset of cluster formation from DLS also corresponds well to the more pronounced structure peak observed in the SANS data for similar concentrations (Fig. 9.4, 8.5 g/L curve).

The interpretation of a clustering of 2D aggregates is in apparent contrast to the observed scaling behavior of Fig. 9.8. One possible explanation for this could be that the clusters observed in the DLS are not tightly bound clusters, but small liquid crystal domains of 2D aggregates. This would seem plausible since 10 g/L is close to the concentration range where liquid crystalline tactoids are routinely observed.^{110,111,116,171,178} Dilution of the concentrated samples showed (shown in appendix section 11) that the original apparent

hydrodynamic diameter could be recovered indicating that the formation of clusters is reversible. This supports the interpretation of a bulk structuring of the 2D aggregates at low concentrations and above 10 g/L small liquid crystal like domains are formed that grow with size for increasing concentration. The liquid crystal domains are also reversible which would not be expected for tightly bound clusters. This explanation is in agreement with the previously discussed scaling behavior.

9.4 Conclusion

SANS was used in combination with DLS, TEM and AFM to probe the structural properties of, carboxymethylated and sulfuric acid hydrolyzed, cellulose nanocrystals and their organization into ordered phases. The experiments showed a tendency of the CNCs to aggregate into 2D-stacks. The SANS data could be well described by a parallelepiped model (with the addition of the modified Caillé model to qualitatively describe the structure contribution). From this analysis a similar cross-section of the 2D aggregates was found for both CNC systems with a width to height aggregation number of 8. The length of the CNC-COOH aggregates was a factor 2 longer than those of the CNC-SO₃H. Using SANS an ordering of both types of aggregates in the low range of the semidilute concentration regime was detected. This is interpreted as an early stage of liquid crystalline ordering at concentrations below those where macroscopic liquid crystalline CNC phases are observed. The inter-aggregate spacing extracted from the SANS data followed a power law of the number density of aggregates with exponents -0.37 and -0.4 for CNC-COOH and CNC-SO₃H respectively. These exponents indicate that the packing of aggregates occurs mainly through space filling rather than tightly bound clustering. For the CNC-COOH aggregates, DLS revealed an increase in the apparent hydrodynamic diameter above a threshold concentration of 10 g/L. This increase in hydrodynamic diameter was reversible and indicates the development of small liquid crystal domains of 2D aggregates.

Chapter 10

Summary and outlook

Most naturally occurring polyelectrolytes are rigid polyelectrolytes, representing a large group of compounds, which are suitable for application in eco-friendly and renewable materials. However, flexible polyelectrolytes as PSS are typically used as polyelectrolyte model systems, but not all findings can be easily transferred to more rigid polyelectrolytes. Hence, the investigation of the rigid polyelectrolyte sPSO₂-220, which is apart from backbone rigidity and dissociation degree very similar to flexible PSS, enables the identification of the effect of polyelectrolyte backbone rigidity on polyelectrolyte properties. Further understanding of rigid polyelectrolytes could enhance their applicability in a wide range of products. This thesis contains separate studies on the following issues:

- The influence of polyelectrolyte backbone rigidity on polyelectrolyte properties *at interfaces*: adsorption behavior, surface composition and foam film stability of several oppositely charged polyelectrolyte/surfactant mixtures;
- The influence of polyelectrolyte backbone rigidity on polyelectrolyte properties *in bulk*: structuring in bulk and confinement for polyelectrolytes and structuring in bulk of rigid rod-like cellulose nanocrystals.

In the first part of this thesis (chapter 5, 6 and 7) the influence of polyelectrolyte rigidity on the adsorption and foam film stability of polyelectrolyte/surfactant mixtures at the air/water interface was investigated. In chapter 5 mixtures of the rigid polyelectrolyte sPSO₂-220 and the surfactant C₁₄TAB were investigated by surface tension, surface elasticity and foam film stability measurements. sPSO₂-220/C₁₄TAB mixtures showed a much higher surface activity and foam film stability than mixtures containing more flexible polyelectrolytes as PAMPS or PSS. In this chapter the role of polyelectrolyte backbone rigidity in the formation of foam films and stabilization of polyelectrolyte/surfactant mixtures was clarified.

In chapter 6 the composition and structure of sPSO₂-220/C₁₄TAB mixtures adsorbed at the air/water interface was investigated with neutron reflectometry (NR). The findings were used to explain the remarkable foam film stability of sPSO₂-220/C₁₄TAB mixtures in comparison to more flexible polyelectrolytes/surfactant mixtures. It was shown that both sPSO₂-220 and C₁₄TAB adsorbed strongly at the air/water interface. This is in accordance with the low surface tension and high foam film stability observed for sPSO₂-220/C₁₄TAB mixtures in chapter 5. Furthermore, the formerly used framework, explaining

foam film stability solely by repulsion of surface charges, was unable to explain the results for certain polyelectrolyte/surfactant ratios. Around the BSMP the surface composition indicated a maximum in adsorption and surface charge, while no stable foam films were found. However, for higher sPSO₂-220 concentrations the surface composition indicated less adsorbed polyelectrolyte/surfactant complexes and surface charge neutrality, while very stable foam films were found. Thus, an enhanced foam film stability framework was developed, taking also the structure of the adsorbed layer(s) into account. It was concluded that around the BSMP the foam film is especially unstable due to a multilayer structure, which might result in an attraction of the foam film surfaces. For higher polyelectrolyte concentrations the foam film is especially stable as a thick and coiled polyelectrolyte layer forms, which might induce further repulsion between the foam film surfaces.

In chapter 7, similar to chapter 6, the relation between surface composition and foam film stability was investigated, but for the more flexible polyelectrolyte PSS in mixtures with C₁₄TAB. The stability of foam films formed by PSS/C₁₄TAB mixtures significantly differed from foam films formed by mixtures of sPSO₂-220 or PAMPS with C₁₄TAB. The latter showed a minimum in foam film stability close to the BSMP and increasing foam film stability with polyelectrolyte concentration beyond the BSMP. PSS/C₁₄TAB showed a relatively constant foam film stability and maximum foam film stability briefly beyond the BSMP. A depletion of surfactant and polyelectrolyte beyond the BSMP was shown by surface compositional analysis with NR. This depletion can be contributed to preferred bulk complexation of this mixture for higher PSS concentrations. Moreover, this chapter discussed foam film stability, surface composition and the enhanced framework for foam film stability (from chapter 6) for mixtures of three polyelectrolytes (sPSO₂-220, PSS and PAMPS) with C₁₄TAB. The enhanced framework was able to resolve mismatches between experimental results and the former framework of foam film stability for flexible polyelectrolyte/surfactant mixtures. Finally, former measurements found that PSS/C₁₄TAB mixtures were unable to form stable foam films. As foam film formation was found to be possible in the present work, possible reasons for the observed deviations to the former findings were discussed.

In the second part of the thesis (chapter 8 and 9) the influence of polyelectrolyte rigidity on bulk ordering was investigated. In chapter 8 the influence of polyelectrolyte backbone rigidity on structuring in bulk and confinement was investigated by comparing the rigid sPSO₂-220 and the flexible PSS. Network like structures in bulk and confinement, as for PSS, were found for sPSO₂-220. The characteristic bulk lengths were shorter for sPSO₂-220 than for PSS due to the higher dissociation degree, leading to a higher ionic strength

and increased screening. In confinement stratification was detected for sPSO₂-220, which led to a relatively high compression of the network of 20 - 50 %, while flexible PSS only showed a compression of 20 %.

The final chapter 9 focused on the shape and structuring of cellulose nanocrystal (CNC) nanoparticles. SANS, TEM, AFM and DLS was used to elucidate the CNC aggregation behavior on the microscale and the ordering of CNC aggregates into liquid crystal like arrangements on the mesoscale. A lateral organization of the CNC particles into 2D aggregates was observed. With increasing concentration the 2D aggregates showed a liquid crystal like ordering. The decay of inter-aggregate distance d ($d \propto c^{-0.37}$ and $d \propto c^{-0.40}$) was close but not equal to the decay found for spherical particles ($d \propto c^{-0.33}$). This indicates that the inter-aggregate distance for anisotropic particles decreases with a proportionality factor between spherical particles and elongated polyelectrolytes ($d \propto c^{-0.5}$). In summary this chapter demonstrated that (1) specific structuring occurs between single CNC particles, and (2) the 2D aggregation may be an intermediate state in the formation of the CNC chiral nematic phase.

This thesis solved some open questions on the properties of rigid polyelectrolytes. However, new questions for further exploration developed. In the following section, some possible directions for future research will be presented.

At first, to continue the investigation of PSS/C₁₄TAB mixtures shown in chapter 7, small angle neutron scattering (SANS) would be useful to investigate PSS/C₁₄TAB complexes in bulk. Thereby, it could be clarified why bulk complexation seems to be favored for certain polyelectrolyte/surfactant ratios for this particular mixture. Moreover, to clarify the influence of the aliphatic chain length of the surfactant for different PSS/C_{1X}TAB mixtures, measurements in bulk (SANS, zeta potential) and at the air/water interface (NR, TFPB) would be helpful.

Secondly, CP-AFM measurements would be helpful to further investigate the influence of confinement on sPSO₂-220 structuring discussed in chapter 8. Moreover, polyelectrolytes with a wider range of persistence lengths l_p could be investigated to further clarify the influence of rigidity on structuring. For example the influence of confinement on DNA structuring would be interesting. DNA has a persistence length of 50 nm¹⁸ and for longer DNA chains no structuring in bulk or in confinement was observed¹⁹. However, for shorter chains structuring was observed in bulk¹⁹²⁻¹⁹⁴ and hence might also be possible in confinement. Moreover, the surface adsorption, surface composition and the correlation to

foam film stability in a DNA/surfactant mixture was, despite some studies,^{18,195} not yet fully elucidated.

Furthermore, while the structuring of spherical nanoparticles in bulk and confinement was extensively investigated, e.g. for silica nanoparticles,⁷⁸⁻⁸⁰ no such study was performed with anisotropic nanoparticles as rod-like shaped CNCs or sheet-like shaped niobate nanoparticles. Both show an ordering in bulk (shown in chapter 9 and ref. 178 and ref. 196), which indicates that there is also ordering in confinement. As mentioned for CNCs the inter-aggregate distance decreased with an unexpected proportionality factor. The investigation of the influence of the shape of nanoparticles on the proportionality factor would merit further investigation. Furthermore, the influence of anisotropic shape on the ordering in confinement would be a interesting field of research.

As mentioned, CNC is a very promising material for a lot of applications, consequently also the surface adsorption, surface composition and foam film stability of CNCs together with oppositely or likely charged surfactants would be of high interest. Some studies already showed that CNCs interact synergistically with surfactants,^{197,198} but information on the resulting surface compositions and foam film stabilities are still missing.

Chapters 5 - 7 showed that the type of polyelectrolyte is decisive for the surface composition of polyelectrolyte/surfactant mixtures. It would be interesting to understand how these different mixtures would react on screening of their charges, e.g. through the addition of low molecular weight salt. So far the influence of salt on foam film stability was mainly investigated for single surfactant systems.^{68,165} Hence, the correlation of surface composition and foam film stability for different polyelectrolyte/surfactant mixtures with different amounts of salt would be a novel and promising field of research.

Chapter 11

Appendix

Appendix to chapter 6

Additional NR profiles for sPSO₂-220/C₁₄TAB mixtures

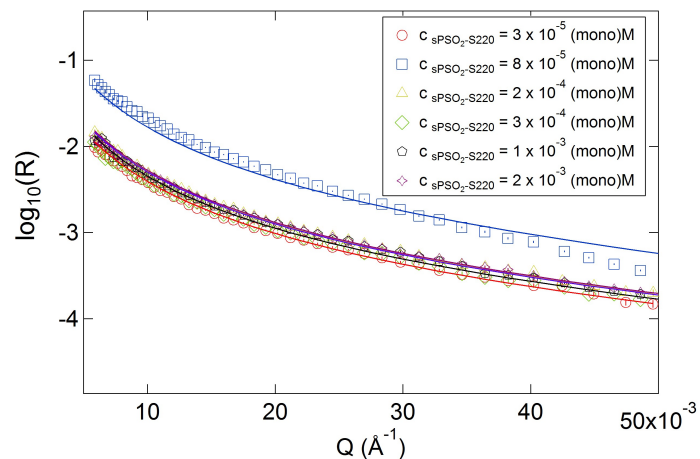


Figure 11.1: Additional NR profiles recorded for sPSO₂-220/dC₁₄TAB/ACMW solutions. The bulk surfactant concentration is fixed at 10^{-4} M, while the sPSO₂-220 concentration is varied. The solid lines correspond to model fits.

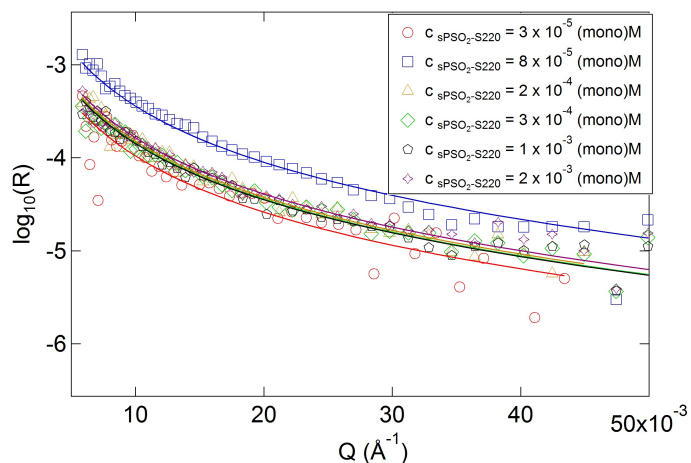


Figure 11.2: Additional NR profiles recorded for sPSO₂-220/cmC₁₄TAB/ACMW solutions. The bulk surfactant concentration is fixed at 10^{-4} M, while the sPSO₂-220 concentration is varied. The solid lines correspond to model fits.

Additional NR profiles for sPSO₂-220/C₁₄TAB mixtures

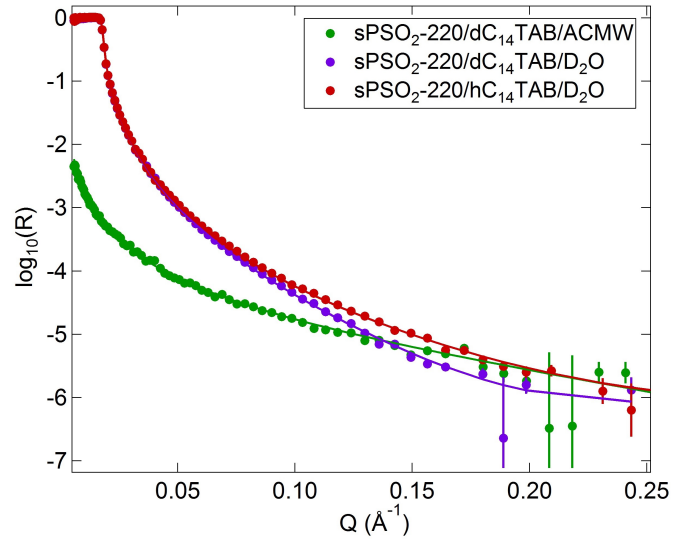


Figure 11.3: Neutron reflectivity profiles for sPSO₂-220/C₁₄TAB mixtures measured at 3 isotopic contrasts. The sPSO₂-220 concentration is $1 \cdot 10^{-5}$ (mono)M and the C₁₄TAB concentration is 10^{-4} M. This concentration corresponds to regime **I** in Fig. 6.5. The solid lines correspond to model fits.

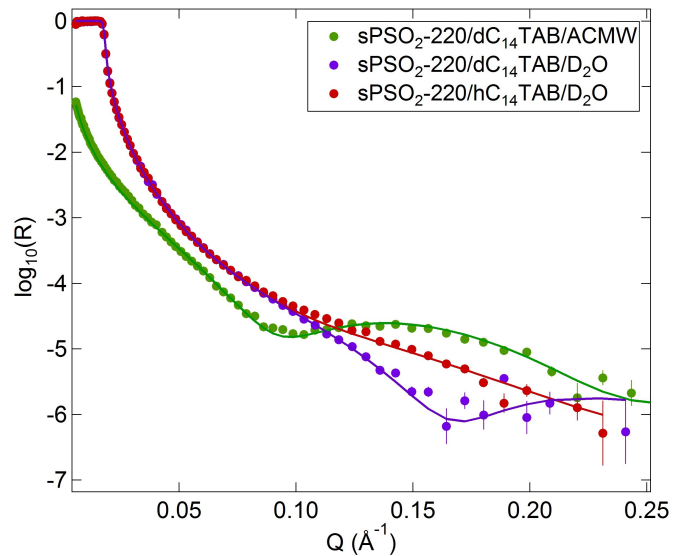


Figure 11.4: Neutron reflectivity profiles for sPSO₂-220/C₁₄TAB mixtures measured at 3 isotopic contrasts. The sPSO₂-220 concentration is $8 \cdot 10^{-5}$ (mono)M and the C₁₄TAB concentration is 10^{-4} M. This concentration corresponds to regime **II** in Fig. 6.5. The solid lines correspond to model fits.

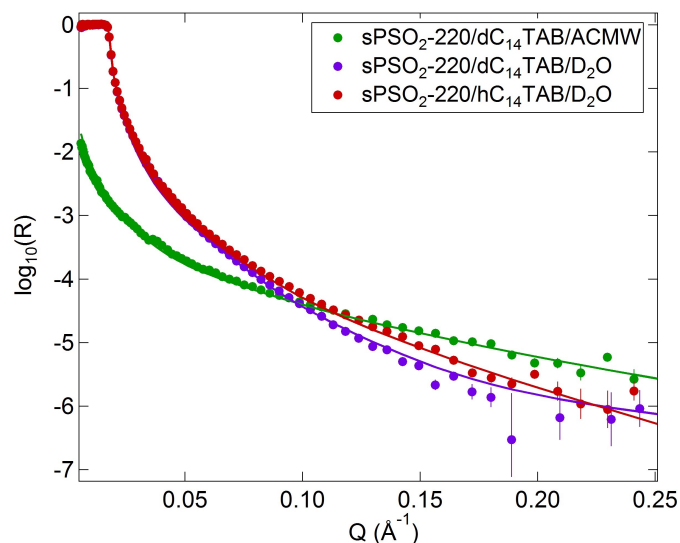


Figure 11.5: Neutron reflectivity profiles for sPSO₂-220/C₁₄TAB mixtures measured at 3 isotopic contrasts. The sPSO₂-220 concentration is $3 \cdot 10^{-3}$ (mono)M and the C₁₄TAB concentration is 10^{-4} M. This concentration corresponds to regime **III** in Fig. 6.5. The solid lines correspond to model fits.

Appendix to chapter 7

Additional NR profiles for PSS/C₁₄TAB mixtures

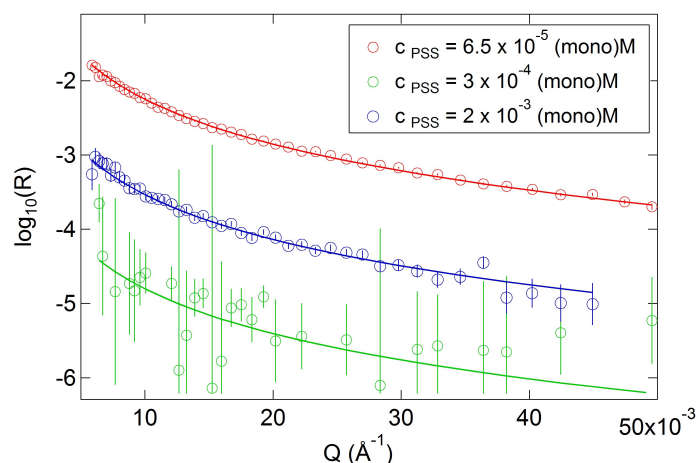


Figure 11.6: Additional NR profiles recorded for PSS/dC₁₄TAB/ACMW solutions. The bulk surfactant concentration is fixed at 10^{-4} M, while the PSS concentration is varied. The solid lines correspond to model fits.

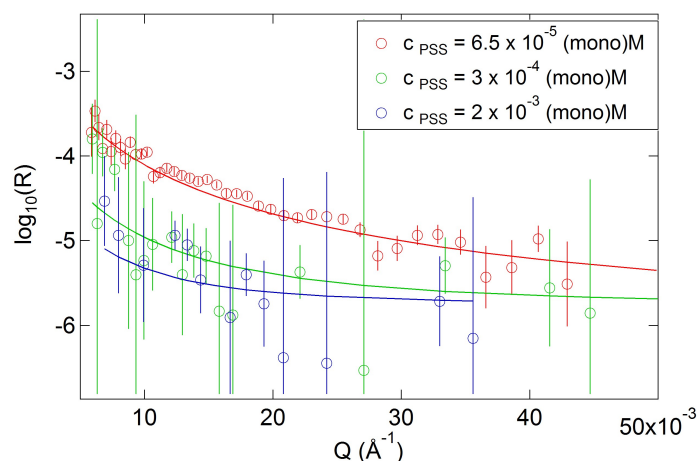


Figure 11.7: Additional NR profiles recorded for PSS/cmC₁₄TAB/ACMW solutions. The bulk surfactant concentration is fixed at 10⁻⁴ M, while the PSS concentration is varied. The solid lines correspond to model fits.

Electrophoretic mobility μ for PSS/C₁₄TAB mixtures

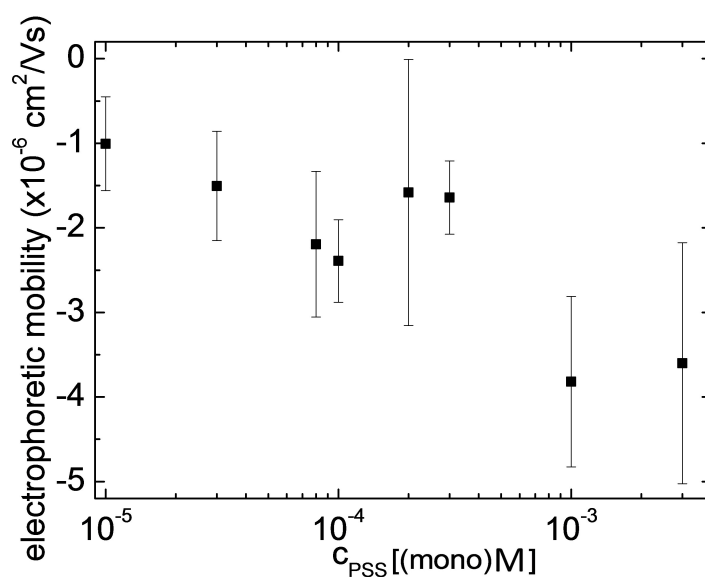


Figure 11.8: The electrophoretic mobility μ for PSS/C₁₄TAB mixtures. The C₁₄TAB concentration is fixed at 10⁻⁴ M, while the PSS concentration is varied. As the zeta potential data in Fig. 7.1, this data shows an increase in electrophoretic mobility μ for PSS concentrations of 2 · 10⁻⁴ and 3 · 10⁻⁴ (mono)M. This shows that for these PSS concentrations the PSS/C₁₄TAB complexes are definitely less negatively charged than for other PSS concentrations.

Surface composition of PAMPS/ C_{14} TAB mixtures for comparison

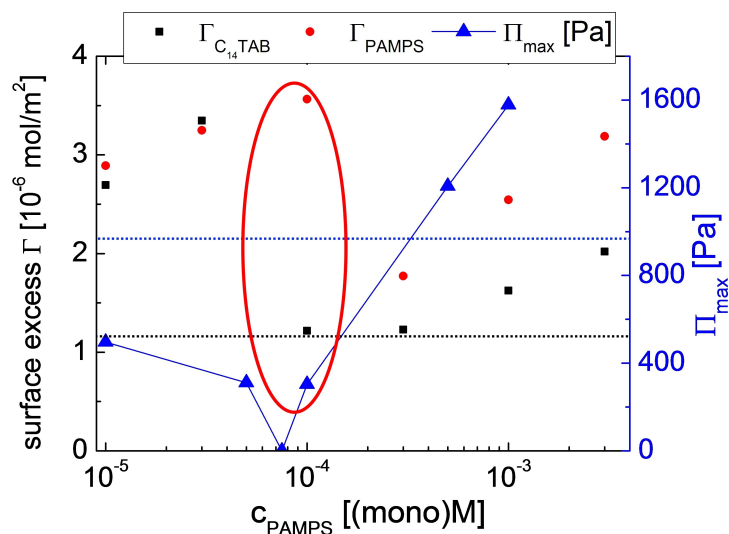


Figure 11.9: The surface excess ratio $\Gamma_{C_{14}\text{TAB}}$, Γ_{PAMPS} and maximum foam film stability of PAMPS/ C_{14} TAB mixtures are shown in dependence of PAMPS concentration.^{15,71} The black dotted line corresponds to the surface excess of a pure C_{14} TAB solution at a concentration of 10^{-4} M, while the blue dotted line corresponds to the stability of the pure C_{14} TAB film at 10^{-4} M. The regime which could not be explained by the formerly used model is marked with the red circle.

Appendix to chapter 8

Additional SAXS curves for aqueous sPSO₂-220 solutions

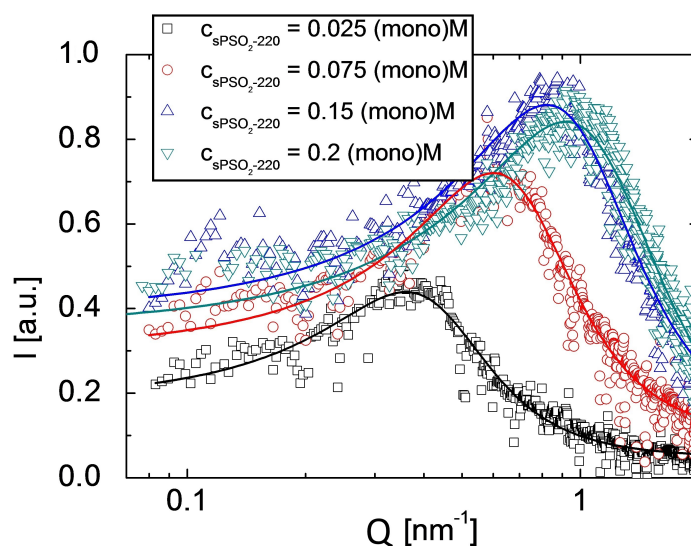


Figure 11.10: Additional SAXS curves recorded for aqueous sPSO₂-220 solutions. The solid lines represent the Lorentz fits of the curves.

Additional disjoining pressure isotherms of sPSO₂-220/C₁₄TAB mixtures

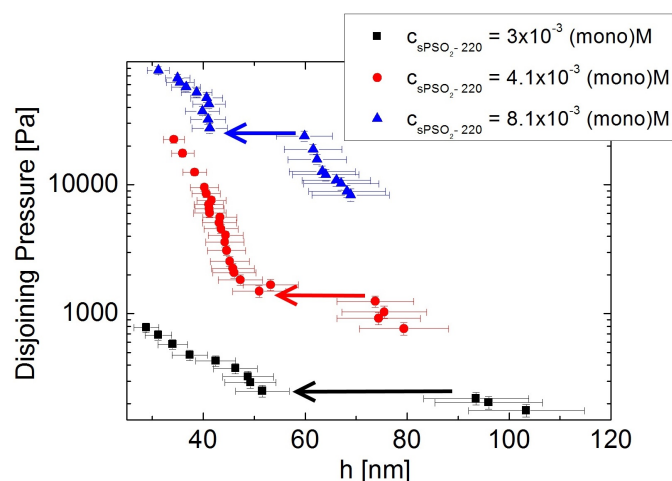


Figure 11.11: Additional disjoining pressure isotherms of sPSO₂-220/C₁₄TAB mixtures with fixed C₁₄TAB concentration of 10⁻⁴ M and varied sPSO₂-220 concentration. The arrows indicates the stratification steps. For better visibility the isotherms are incrementally shifted by a factor of ten. The isotherm with the lowest sPSO₂-220 concentration is in absolute scale.

Appendix to Chapter 9

Additional SANS curves for CNC-COOH

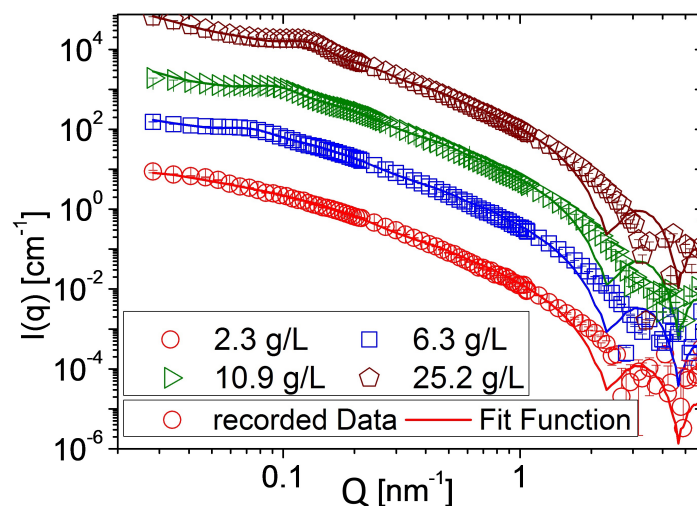


Figure 11.12: Additional SANS curves recorded for CNC-COOH and fitted with the parallelepiped model. For better visibility curves are incrementally shifted by a factor of ten. The lowest concentration curve is in absolute scale.

Additional AFM images

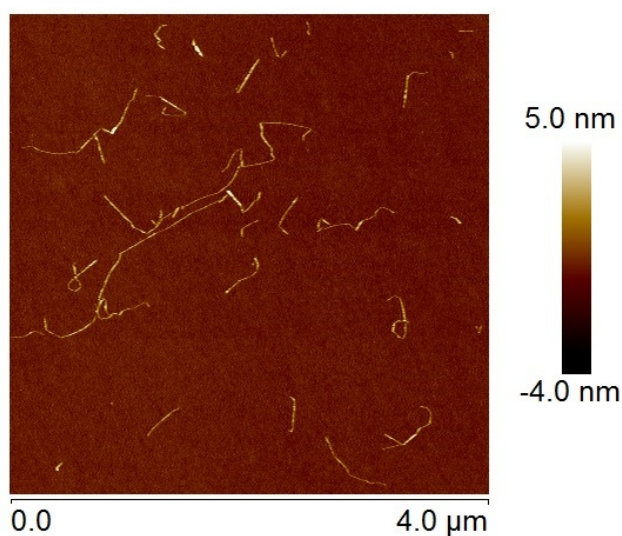


Figure 11.13: CNF-COOH, starting material for CNC-COOH preparation, showing its fibrillar shape. This data was recorded by Andreas Fall (experimental details are given in ref. 133).

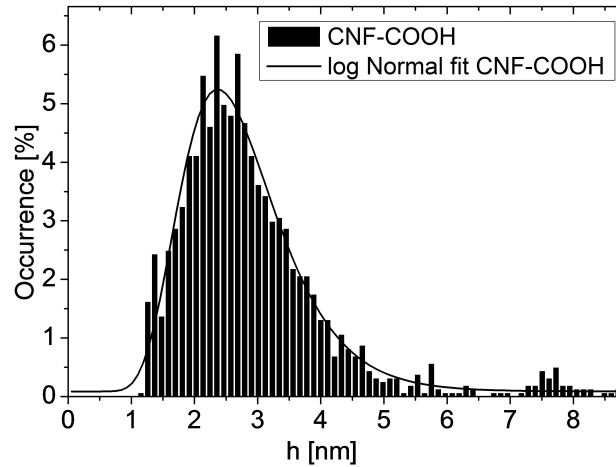


Figure 11.14: AFM height distributions from individual particles of CNF-COOH fitted with a log-normal distribution function (equation 9.1). From the fit an average particle height of 2.5 nm was found.

A log-normal distribution function (equation 9.1) was used to describe the AFM data. For CNF-COOH $\sigma = 0.33$ and $\mu = 0.86$ was found. This gives an average particle height of 2.5 nm for CNF-COOH. The inset of Fig. 11.15 shows height profiles across three clusters of CNC-COOH aggregates.

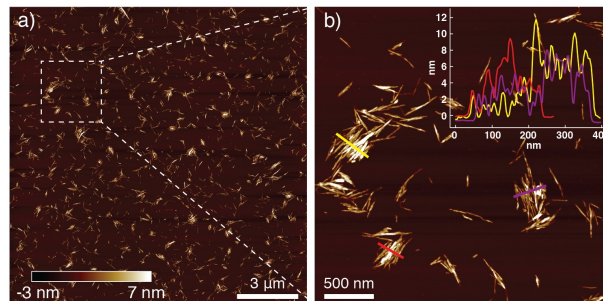


Figure 11.15: AFM image of CNC-COOH showing single crystal aggregates. The inset of panel b) shows the height distribution across 3 clusters of crystal aggregates. This data was recorded by Andreas Fall (experimental details are given in ref. 133).

Structure peak $S(Q)$ evaluation

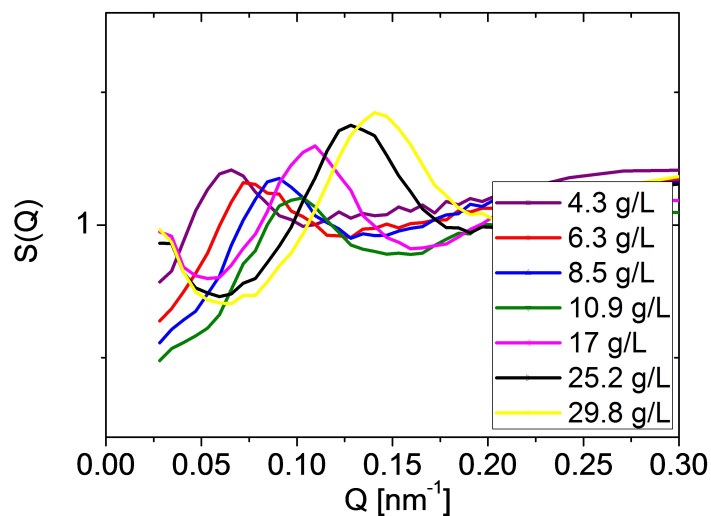


Figure 11.16: $S(Q)$ for CNC-COOH.

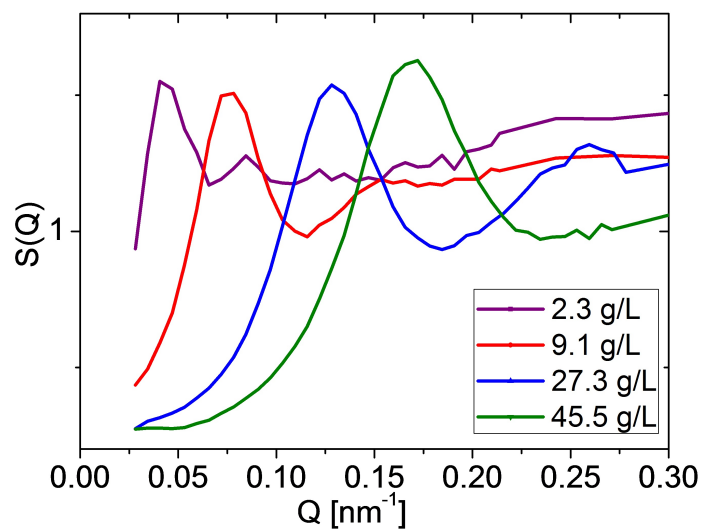


Figure 11.17: $S(Q)$ for CNC-SO₃H.

Aggregate interactions and packing

The ionic strengths I , of the aggregate dispersions were estimated from the total number of available counterions as given by the product of the charge density (in mol/g) and the aggregate concentration (in g/L). For example, the CNC-COOH sample at 10.9 g/L has an estimated ionic strength of $0.36 \text{ mmol/g} \cdot 10.9 \text{ g/L} = 3.9 \text{ mmol/L}$. To estimate the overlap aggregate volume fraction, the following expression was used: $\Phi_{OL} = (h/L)^2 = a^{-2}$ where

h is the height of the aggregate, L is the length of the aggregate and a is the aggregate aspect ratio. From the aggregate dimensions the overlap concentration for CNC-COOH and CNC-SO₃H can be estimated to 0.1 g/L and 0.5 g/L respectively. If the aggregates are distributed uniformly in space, the average distance between the aggregates can be estimated from the aggregate number density, n , as: $d=n^{-1/3}$. This gives the scaling exponent -1/3 for space filling of aggregates used as comparison in Fig. 9.8.

The Debye length was calculated using equation 11.1, where the ionic strength, I , has been estimated from the concentration of counter ions in the samples.

$$\frac{1}{\kappa} = \sqrt{\frac{\epsilon_r \epsilon_0 k T}{2 N_A e^2 I}} \quad (11.1)$$

Here ϵ_r is the dielectric constant, ϵ_0 the permittivity of free space, k the Boltzmann constant, T the temperature in Kelvin, N_A the Avogadro number and e the elementary charge.

Table 11.1 shows the CNC-COOH cluster size, in the form of the hydrodynamic diameter D_h extracted from DLS, during increasing CNC aggregate concentration followed by dilution. The results show the reversibility of the CNC-COOH cluster formation.

| | $Z_{avg} (D_h)$ | c (g/L) | remark |
|-----------------------|-----------------|-----------|---------------------|
| original sample | 102 | 0.1 | |
| after upconcentration | 886 | 35 | |
| after dilution | 174 | 0.1 | no stirring |
| after dilution | 136 | 0.1 | stirring over night |

Table 11.1: Hydrodynamic diameter D_h extracted from DLS data for CNC-COOH for varying CNC aggregate concentrations before and after dilution.

Acknowledgements

At first, I would like to thank my supervisor Prof. Dr. Regine von Klitzing for giving me the opportunity to work in her research group. Her helpful suggestions, encouragement, warm support and kind caring, made this thesis possible. I appreciate her contribution of time, ideas and funding throughout the years.

Secondly, my thanks go to Dr. habil Cécile Monteux for her willingness to be my second supervisor.

Thirdly, I would like to thank Dr. Klaus-Dieter Kreuer for providing the sPSO₂-220 sample.

Furthermore, my thanks go to Dr. Reinhard Miller for the opportunity to do the surface elasticity measurements in his group. I would also like to thank Sabine Siegmund, who introduced me to the PAT1, helped me to solve various technical problems and created a very comfortable atmosphere.

I would like to thank Dr. Richard Campbell for his assistance with the FIGARO experiments, data evaluation and scientific discussions.

I would like to thank my swedish colleagues Dr. Gustav Nyström and Dr. Andreas Fall for the enjoyable work on the publication about cellulose nanocrystals and Dr. Sylvain Prévost for his help with the SANS data evaluation.

Moreover, I want to thank all the members of the von Klitzing group, the CTA's and the secretaries for the friendly atmosphere in and around the lab and for their help with various problems. Furthermore, I want to thank Tine Bundesmann, who was of great help to me.

Special thanks go to Marieke for our relaxed lunch breaks, exhausting times in the gym and her extensive scientific help. Also Adrian, Olli, Jens and Michi were amazing colleagues, which whom hanging out eased the hard work.

Also my friends without a natural science background were of great help. They helped me to calm down, encouraged me to do some practical research on common foams, with the main focus on the influence of cosurfactants, or even let me totally forget about my research from time to time.

A very big thanks goes to my family, which supported me the whole time with a huge amount of knowledge (scientific and non-scientific), time and generosity.

Freddy Schenk and Dicki Chocobo were of great help in calming me down throughout the whole thesis.

Finally, I want to thank my gorgeous girlfriend Sarah, who gave my tons of reasons to stay on track and did an excellent job in cheering me up when science made my grumpy. She is a keeper.

The financial support from the Deutsche Forschungsgemeinschaft within the framework of SPP "Kolloid- und Verfahrenstechnik" 1273 Kl-1165/10 is kindly acknowledged.

Bibliography

- [1] Rodríguez Patino, J. M.; Carrera Sánchez, C.; Rodríguez Niño, M. R. *Adv. Colloid Interface Sci.* **2008**, *140*, 95–113.
- [2] Langevin, D. *ChemPhysChem* **2008**, *9*, 510–522.
- [3] Lindman, B.; Antunes, F.; Aidarova, S.; Miguel, M.; Nylander, T. *Colloid Journal* **2014**, *76*, 585–594.
- [4] Bureiko, A.; Trybala, A.; Kovalchuk, N.; Starov, V. *Adv. Colloid Interface Sci.* **2014**, *222*, 670–677.
- [5] Budhathoki, M.; Barnee, S. H. R.; Shiau, B.-J.; Harwell, J. H. *Colloids Surface A* **2016**, *498*, 66–73.
- [6] Üzüüm, C.; Kristen, N.; von Klitzing, R. *Curr. Opin. Colloid Interface Sci.* **2010**, *15*, 303–314.
- [7] Bain, C. D.; Claesson, P. M.; Langevin, D.; Meszaros, R.; Nylander, T.; Stubenrauch, C.; Titmuss, S.; v. Klitzing, R. *Adv. Colloid Interface Sci.* **2010**, *155*, 32–49.
- [8] Fauser, H.; v. Klitzing, R. *Soft Matter* **2014**, *10*, 6903–6916.
- [9] Brunet, A.; Tardin, C.; Salomé, L.; Rousseau, P.; Destainville, N.; Manghi, M. *Macromolecules* **2015**, *48*, 3641–3652.
- [10] Venkatesan, J.; Bhatnagar, I.; Manivasagan, P.; Kang, K.-H.; Kim, S.-K. *Int. J. Biol. Macromol.* **2015**, *72*, 269–281.
- [11] Petri, D. F. S. *J. Appl. Polym. Sci.* **2015**, *132*, 42035.
- [12] Klemm, D.; Kramer, F.; Moritz, S.; Lindström, T.; Ankerfors, M.; Gray, D.; Dorris, A. *Angew. Chem. Int. Edit.* **2011**, *50*, 5438–5466.
- [13] Zeng, J.-B.; He, Y.-S.; Li, S.-L.; Wang, Y.-Z. *Biomacromolecules* **2012**, *13*, 1–11.
- [14] Kristen, N.; Vüllings, A.; Laschewsky, A.; Miller, R.; v. Klitzing, R. *Langmuir* **2010**, *26*, 9321–9327.
- [15] Kristen, N.; Simulescu, V.; Vüllings, A.; Laschewsky, A.; Miller, R.; v. Klitzing, R. *J. Phys. Chem. B* **2009**, *113*, 7986–7990.
- [16] Üzüüm, C.; Christau, S.; von Klitzing, R. *Macromolecules* **2011**, *44*, 7782–7791.
- [17] v. Klitzing, R.; Espert, A.; Colin, A.; Langevin, D. *Colloids Surface A* **2001**, *176*, 109–116.
- [18] Kleinschmidt, F.; Stubenrauch, C.; Delacotte, J.; von Klitzing, R.; Langevin, D. *J. Phys. Chem. B* **2009**, *113*, 3972–3980.
- [19] Üzüüm, C. The Effects of Confinement on Structure and Rheology of Thin Liquid and Adsorbed Polyelectrolyte Films. Ph.D. thesis, TU Berlin, 2011.

- [20] Cantat, I.; Cohen-Addad, S.; Elias, F.; Graner, F.; Höhler, R.; Pitois, O. *Foams: Structure and Dynamics*; Oxford University Press, 2013.
- [21] Dörfler, H.-D. *Grenzflächen und kolloid-disperse Systeme*; Springer, 2002.
- [22] Taylor, D.; Thomas, R.; Penfold, J. *Adv. Colloid Interface Sci.* **2007**, *132*, 69–110.
- [23] Thomas, R. K. *Annu. Rev. Phys. Chem.* **2004**, *55*, 391–426.
- [24] Kundu, S.; Langevin, D.; Lee, L.-T. *Langmuir* **2008**, *24*, 12347–12353.
- [25] Radeva, T., Ed. *Physical Chemistry of Polyelectrolytes*; Marcel Decker Inc., 2001.
- [26] Dobrynin, A. V.; Rubinstein, M. *Prog. Polym. Sci.* **2005**, *30*, 1049–1118.
- [27] Goddard, E. D. *J. Colloid Interf. Sci.* **2002**, *256*, 228–235.
- [28] Kristen, N.; v. Klitzing, R. *Soft Matter* **2010**, *6*, 849–861.
- [29] Venzmer, J. *Chemie in Unserer Zeit* **2008**, *42*, 72–79.
- [30] Argillier, J. F.; Zeilinger, S.; Roche, P. *Oil Gas Sci. Technol.* **2009**, *64*, 597–605.
- [31] Theodoly, O.; Tan, J.; Ober, R.; Williams, C.; Bergeron, V. *Langmuir* **2001**, *17*, 4910–4918.
- [32] v. Klitzing, R.; Kolarić, B.; Jaeger, W.; Brandt, A. *Phys. Chem. Chem. Phys.* **2002**, *4*, 1907–1914.
- [33] Kolarić, B.; Jaeger, W.; Hedicke, G.; v. Klitzing, R. *J. Phys. Chem. B* **2003**, *107*, 8152–8157.
- [34] Wu, Y.; Chen, J.; Fang, Y.; Zhu, M. *J. Colloid Interf. Sci.* **2016**, *479*, 34–42.
- [35] Monteux, C.; Williams, C. E.; Meunier, J.; Anthony, O.; Bergeron, V. *Langmuir* **2004**, *20*, 57–63.
- [36] Monteux, C.; Llauro, M. F.; Baigl, D.; Williams, C. E.; Anthony, O.; Bergeron, V. *Langmuir* **2004**, *20*, 5367–5374.
- [37] Kristen-Hochrein, N.; Laschewsky, A.; Miller, R.; v. Klitzing, R. *J. Phys. Chem. B* **2011**, *115*, 14475–14483.
- [38] Campbell, R. A.; Tummino, A.; Noskov, B.; Varga, I. *Soft Matter* **2016**, *12*, 5304–5312.
- [39] Folmer, B. M.; Kronberg, B. *Langmuir* **2000**, *16*, 5987–5992.
- [40] v. Klitzing, R. *Adv. Colloid Interface Sci.* **2005**, *114-115*, 253–66.
- [41] Petkova, R.; Tcholakova, S.; Denkov, N. *Colloids Surface A* **2013**, *438*, 174–185.
- [42] Asnacios, A.; Langevin, D.; Argillier, J.-F. *Macromolecules* **1996**, *29*, 7412–7417.

- [43] Asnacios, A.; Espert, A.; Colin, A.; Langevin, D. *Phys. Rev. Lett.* **1997**, *78*, 4974–4977.
- [44] Ritacco, H.; Kurlat, D.; Langevin, D. *J. Phys. Chem. B* **2003**, *107*, 9146–9158.
- [45] Ritacco, H.; Busch, J. *Langmuir* **2004**, *20*, 3648–3656.
- [46] Noskov, B. A.; Loglio, G.; Miller, R. *J. Phys. Chem. B* **2004**, *108*, 18615–18622.
- [47] Campbell, R. A.; Ash, P. A.; Bain, C. D. *Langmuir* **2007**, *23*, 3242–3253.
- [48] Campbell, R. A.; Angus-Smyth, A.; Yanez Arteta, M.; Tonigold, K.; Nylander, T.; Varga, I. *J. Phys. Chem. Lett.* **2010**, *1*, 3021–3026.
- [49] Bahramian, A.; Thomas, R. K.; Penfold, J. *J. Phys. Chem. B* **2014**, *118*, 2769–2783.
- [50] Ábrahám, Á.; Kardos, A.; Mezei, A.; Campbell, R. A.; Varga, I. *Langmuir* **2014**, *30*, 4970–4979.
- [51] Bell, C. G.; Breward, C. J. W.; Howell, P. D.; Penfold, J.; Thomas, R. K. *Langmuir* **2007**, *23*, 6042–6052.
- [52] Ábraham, Á.; Campbell, R. A.; Varga, I. *Langmuir* **2013**, *29*, 11554–11559.
- [53] Monteux, C.; Fuller, G. G.; Bergeron, V. *Journal of Physical Chemistry B* **2004**, *108*, 16473–16482.
- [54] Trabelsi, S.; Langevin, D. *Langmuir* **2007**, *23*, 1248–1252.
- [55] Taylor, D. J. F.; Thomas, R. K.; Li, P. X.; Penfold, J. *Langmuir* **2003**, *19*, 3712–3719.
- [56] Monteux, C.; Llauro, M. F.; Baigl, D.; Williams, C. E.; Anthony, O.; Bergeron, V. *Langmuir* **2004**, *20*, 5358–5366.
- [57] Stubenrauch, C.; Albouy, P.-A.; v. Klitzing, R.; Langevin, D. *Langmuir* **2000**, *16*, 3206–3213.
- [58] Bergeron, V. *Langmuir* **1997**, *7463*, 3474–3482.
- [59] van der Net, A.; Gryson, A.; Ranft, M.; Elias, F.; Stubenrauch, C.; Drenckhan, W. *Colloids Surface A* **2009**, *346*, 5–10.
- [60] Rio, E.; Drenckhan, W.; Salonen, A.; Langevin, D. *Adv. Colloid Interface Sci.* **2014**, *205*, 74–86.
- [61] Fameau, A.-L.; Carl, A.; Saint-Jalmes, A.; von Klitzing, R. *ChemPhysChem* **2015**, *16*, 66–75.
- [62] Exerowa, D.; Kruglyakov, M. *Foam and Foam Films-Theory, Experiment, Application*; Elsevier: Amsterdam, 1998.

- [63] Stubenrauch, C.; von Klitzing, R. *J. Phys. Condens. Matter* **2003**, *1197*, R1197–R1232.
- [64] v. Klitzing, R.; Thormann, E.; Nylander, T.; Langevin, D.; Stubenrauch, C. *Adv. Colloid Interface Sci.* **2010**, *155*, 19–31.
- [65] Schulze-Schlarmann, J.; Buchavzov, N.; Stubenrauch, C. *Soft Matter* **2006**, *2*, 584–594.
- [66] Stubenrauch, C.; Schlarmann, J.; Strey, R. *Phys. Chem. Chem. Phys.* **2002**, *4*, 4504–4513.
- [67] Karraker, K. A.; Radke, C. J. *Adv. Colloid Interface Sci.* **2002**, *96*, 231–264.
- [68] Schelero, N.; v. Klitzing, R. *Curr. Opin. Colloid Interface Sci.* **2015**, *20*, 124–129.
- [69] Stubenrauch, C.; Fainerman, V. B.; Aksenenko, E. V.; Miller, R. *J. Phys. Chem. B* **2005**, *109*, 1505–1509.
- [70] Noskov, B. A. *Curr. Opin. Colloid Interface Sci.* **2010**, *15*, 229–236.
- [71] Fauser, H.; v. Klitzing, R.; Campbell, R. A. *J. Phys. Chem. B* **2015**, *119*, 348–358.
- [72] Kristen-Hochrein, N.; Schelero, N.; v. Klitzing, R. *Colloids Surface A* **2011**, *382*, 165–173.
- [73] Fauser, H.; Uhlig, M.; Miller, R.; v. Klitzing, R. *J. Phys. Chem. B* **2015**, *119*, 12877–12886.
- [74] Bergeron, V.; Claesson, P. M. *Adv. Colloid Interface Sci.* **2002**, *96*, 1–20.
- [75] Beltrán, C. M.; Langevin, D. *Phys. Rev. Lett.* **2005**, *94*, 1–4.
- [76] Toca-Herrera, J.; von Klitzing, R. *Macromolecules* **2002**, *35*, 2861–2864.
- [77] Bergeron, V.; Langevin, D.; ; Asnacios, A. *Langmuir* **1996**, *12*, 1550–1556.
- [78] Klapp, S. H. L.; Grandner, S.; Zeng, Y.; von Klitzing, R. *J. Phys. Condens. Matter* **2008**, *20*, 494232.
- [79] Zeng, Y. Structuring of colloidal dispersions in slit-pore confinement. Ph.D. thesis, TU Berlin, 2011.
- [80] Zeng, Y.; Schön, S.; v. Klitzing, R. *J. Colloid Interf. Sci.* **2015**, *449*, 522–529.
- [81] v. Klitzing, R.; Kolarić, B. *Tenside, Surfactants, Deterg* **2002**, *39*, 247–253.
- [82] v. Klitzing, R.; Kolarić, B. *Prog. Colloid Polym. Sci.* **2003**, *122*, 122–129.
- [83] Dobrynin, A. V.; Colby, R. H.; Rubinstein, M. *Macromolecules* **1995**, *28*, 1859–1871.
- [84] Qu, D.; Pedersen, J. S.; Garnier, S.; Laschewsky, A.; Möhwald, H.; von Klitzing, R. *Macromolecules* **2006**, *39*, 7364–7371.

- [85] Kolarić, B.; Jaeger, W.; v. Klitzing, R. *J. Phys. Chem. B* **2000**, *104*, 5096–5101.
- [86] Beltrán, C. M.; Guillot, S.; Langevin, D. *Macromolecules* **2003**, *36*, 8506–8512.
- [87] Heinig, P.; Beltrán, C. M.; Langevin, D. *Phys. Rev. E* **2006**, *73*, 1–8.
- [88] Butt, H. J.; Cappella, B.; Kappl, M. *Surf. Sci. Rep.* **2005**, *59*, 1–152.
- [89] Delacotte, J.; Rio, E.; Restagno, F.; Uzüm, C.; von Klitzing, R.; Langevin, D. *Langmuir* **2010**, *26*, 7819–7823.
- [90] Glatter, O.; Kratky, O. *Small Angle X-ray Scattering*; 1982.
- [91] Qu, D.; Baigl, D.; Williams, C. E.; Mohwald, H.; Fery, A. *Macromolecules* **2003**, *36*, 6878–6883.
- [92] Üzüm, C.; Makuska, R.; von Klitzing, R. *Macromolecules* **2012**, *45*, 3168–3176.
- [93] Yang, S.; Tan, H.; Yan, D.; Nies, E.; Shi, A. C. *Phys. Rev. E* **2007**, *75*, 061803.
- [94] Kim, S. C.; Suh, S. H.; Seong, B. S. *J. Chem. Phys.* **2007**, *127*, 114903.
- [95] Berglund, L. A.; Peijs, T. *MRS Bulletin* **2010**, *35*, 201–207.
- [96] Nishiyama, Y.; Langan, P.; Chanzy, H. *J. Am. Chem. Soc.* **2002**, *124*, 9074–9082.
- [97] Saito, T.; Uematsu, T.; Kimura, S.; Enomae, T.; Isogai, A. *Soft Matter* **2011**, *7*, 8804–8809.
- [98] Kelly, J. A.; Manchee, C. P. K.; Cheng, S.; Ahn, J. M.; Shopsowitz, K. E.; Hamad, W. Y.; MacLachlan, M. J. *J. Mater. Chem. C* **2014**, *2*, 5093–5097.
- [99] Siró, I.; Plackett, D. *Cellulose* **2010**, *17*, 459–494.
- [100] Habibi, Y.; Lucia, L. A.; Rojas, O. J. *Chem. Rev.* **2010**, *110*, 3479–500.
- [101] Moon, R. J.; Martini, A.; Nairn, J.; Simonsen, J.; Youngblood, J. *Chem. Soc. Rev.* **2011**, *40*, 3941–3994.
- [102] Mihindukulasuriya, S.; Lim, L.-T. *Trends in Food Science & Technology* **2014**, *40*, 149–167.
- [103] Ahmadzadeh, S.; Nasirpour, A.; Keramat, J.; Hamdami, N.; Behzad, T.; Desobry, S. *Colloids Surface A* **2015**, *468*, 201–210.
- [104] Plackett, D. V.; Letchford, K.; Jackson, J. K.; Burt, H. M.; Jackson, J.; Burt, H. *Nord. Pulp. Pap. Res. J.* **2014**, *29*, 105–118.
- [105] Jorfi, M.; Foster, E. J. *J. Appl. Polym. Sci.* **2015**, *132*, 41719.
- [106] Elazzouzi-Hafraoui, S.; Nishiyama, Y.; Putaux, J.-L.; Heux, L.; Dubreuil, F.; Rochas, C. *Biomacromolecules* **2008**, *9*, 57–65.

- [107] Khandelwal, M.; Windle, A. H. *Carbohydr. Polym.* **2014**, *106*, 128–131.
- [108] Dong, X.; Revol, J.; Gray, D. *Cellulose* **1998**, *2*, 19–32.
- [109] Habibi, Y.; Chanzy, H.; Vignon, M. R. *Cellulose* **2006**, *13*, 679–687.
- [110] Revol, J. F.; Bradford, H.; Giasson, J.; Marchessault, R. H.; Gray, D. G. *Int. J. Biol. Macromol.* **1992**, *14*, 170–172.
- [111] Orts, W.; Godbout, L.; Marchessault, R. H.; Revol, J. F. *Macromolecules* **1998**, *31*, 5717–5725.
- [112] Salajková, M.; Berglund, L. A.; Zhou, Q. *J. Mater. Chem.* **2012**, *22*, 19798–19805.
- [113] Araki, J.; Kuga, S. *Langmuir* **2001**, *17*, 4493–4496.
- [114] Lagerwall, S. T. *Adv. Colloid Interface Sci.* **2014**, *208C*, 1–9.
- [115] Nyström, G.; Fall, A. B.; Carlsson, L.; Wågberg, L. *Cellulose* **2014**, *21*, 1591–1599.
- [116] Park, J. H.; Noh, J.; Schütz, C.; Salazar-Alvarez, G.; Scalia, G.; Bergström, L.; Lagerwall, J. P. F. *ChemPhysChem* **2014**, *15*, 1477–1484.
- [117] Munier, P.; Gordeyeva, K.; Bergström, L.; Fall, A. B. *Biomacromolecules* **2016**, *17*, 1875–1881.
- [118] Usov, I.; Nyström, G.; Adamcik, J.; Handschin, S.; Schütz, C.; Fall, A.; Bergström, L.; Mezzenga, R. *Nature Communications* **2015**, *6*, 7564.
- [119] Schuster, M.; de Araujo, C. C.; Atanasov, V.; Andersen, H. T.; Kreuer, K.-D.; Maier, J. *Macromolecules* **2009**, *42*, 3129–3137.
- [120] Schuster, M.; Kreuer, K.-D.; Andersen, H. T.; Maier, J. *Macromolecules* **2007**, *40*, 598–607.
- [121] de Araujo, C. C.; Kreuer, K.-D.; Schuster, M.; Portale, G.; Mendil-Jakani, H.; Gebel, G.; Maier, J. *Phys. Chem. Chem. Phys.* **2009**, *11*, 3305–3312.
- [122] Kreuer, K.-D.; Portale, G. *Adv. Funct. Mater.* **2013**, *23*, 5390–5397.
- [123] Wang, C.; Paddison, S. J. *J. Phys. Chem. A* **2012**, *117*, 650–660.
- [124] Wang, C.; Paddison, S. J. *Soft Matter* **2014**, *10*, 819–830.
- [125] Uhlig, M.; Miller, R.; von Klitzing, R. *Phys. Chem. Chem. Phys.* **2016**, *18*, 18414–18423.
- [126] Smiatek, J.; Wohlfarth, A.; Holm, C. *New J. Phys.* **2014**, *16*, 025001.
- [127] Wohlfarth, A.; Smiatek, J.; Kreuer, K.-D.; Takamuku, S.; Jannasch, P.; Maier, J. *Macromolecules* **2015**, *48*, 1134–1143.
- [128] Manning, G. S. *Annu. Rev. Phys. Chem.* **1972**, *23*, 117–140.

- [129] Gospodinova, N.; Tomšík, E.; Omelchenko, O. *European Polymer Journal* **2016**, *74*, 130–135.
- [130] Taylor, D. J. F.; Thomas, R. K.; Hines, J. D.; Humphreys, K.; Penfold, J. *Langmuir* **2002**, *18*, 9783–9791.
- [131] Kristen, N. Interactions in thin liquid films : Oppositely charged polyelectrolyte / surfactant mixtures. Ph.D. thesis, TU Berlin, 2010.
- [132] Fauser, H. Surface adsorption of oppositely charged surfactant and surfactant-polyelectrolyte mixtures and the relation to foam film formation and stability. Ph.D. thesis, TU Berlin, 2016.
- [133] Uhlig, M.; Fall, A.; Wellert, S.; Lehmann, M.; Prévost, S.; Wågberg, L.; von Klitzing, R.; Nyström, G. *Langmuir* **2016**, *32*, 442–450.
- [134] Beck-Candanedo, S.; Roman, M.; Gray, D. *Biomacromolecules* **2005**, *6*, 1048–1054.
- [135] Butt, H.-J.; Graf, K.; Kappl, M. *Physics and Chemistry of Interfaces*; Wiley-VCH, Weinheim, 2003.
- [136] Krustev, R.; Müller, H.-J. *Langmuir* **1999**, *15*, 2134–2141.
- [137] Loglio, G.; Tesei, U.; Cini, R. *J. Colloid Interf. Sci.* **1979**, *71*, 316–320.
- [138] Loglio, G.; Pandolfini, P.; Miller, R.; Ravera, F.; Ferrari, M.; Liggieri, L. *Novel Methods to Study Interfacial Layers*; Elsevier: Amsterdam, 2001.
- [139] Rotenberg, Y.; Boruvka, L.; Neumann, A. *J. Colloid Interf. Sci.* **1983**, *93*, 169–183.
- [140] Boucher, E.; Evans, M.; Jones, T. *Adv. Colloid Interfac.* **1987**, *27*, 43–79.
- [141] Leser, M.; Acquistapace, S.; Cagna, A.; Makievski, A.; Miller, R. *Colloids Surface A* **2005**, *261*, 25–28.
- [142] Mysels, K. J.; Jones, M. N. *Discuss. Faraday Soc.* **1966**, *42*, 42–50.
- [143] Sheludko, A. *Adv. Colloid Surf. Sci.* **1967**, *1*, 391–464.
- [144] Linse, P. PB Version 2.2; 2009. See also www.fkem1.lu.se/sm.
- [145] Gutsche, C.; Keyser, U.; Kegler, K.; Kremer, F.; Linse, P. *Phys. Rev. E* **2007**, *76*, 1–7.
- [146] Campbell, R. A.; Wacklin, H.; Sutton, I.; Cubitt, R.; Fragneto, G. *Eur. Phys. J. Plus* **2011**, *126*, 107.
- [147] Nelson, A. *J. Appl. Crystallogr.* **2006**, *39*, 273–276.
- [148] Keiderling, U.; Wiedenmann, A. *Physica B* **1995**, *213-214*, 895–897.
- [149] Keiderling, U. *Appl. Phys. A* **2002**, *74*, s1455–s1457.

- [150] Kohlbrecher, J.; Bressler, I. <http://sasfit.ingobressler.net/>.
- [151] Delgado, A. V.; González-Caballero, F.; Hunter, R. J.; Koopal, L. K.; Lyklema, J. *Pure Appl. Chem.* **2005**, *77*, 1753–1805.
- [152] Smoluchowski, M. In *Handbuch der Electricität und des Magnetismus*; Graetz, L., Ed.; J. A. Barth, 1921; p 366.
- [153] Chiappisi, L.; Prévost, S.; Grillo, I.; Gradzielski, M. *Langmuir* **2014**, *30*, 1778–1787.
- [154] Itakura, M.; Shimada, K.; Matsuyama, S.; Saito, T.; Kinugasa, S. *J. Appl. Polym. Sci.* **2006**, *99*, 1953–1959.
- [155] Gettinger, C. L.; Heeger, A. J.; Drake, J. M.; Pine, D. J. *J. Chem. Phys.* **1994**, *101*, 1673–1678.
- [156] Kratky, O.; Porod, G. *Rec. Trav. Chim. Pays-Bas* **1949**, *68*, 1106–1122.
- [157] Nierlich, M.; Boue, F.; Lapp, A.; Oberthür, R. *Colloid & Polymer Sci.* **1985**, *263*, 955–964.
- [158] Reed, W. F.; Ghosh, S.; Medjahdi, G.; Francois, J. *Macromolecules* **1991**, *24*, 6189–6198.
- [159] Trefalt, G.; Behrens, S. H.; Borkovec, M. *Langmuir* **2016**, *32*, 380–400.
- [160] Popa, I.; Sinha, P.; Finessi, M.; Maroni, P.; Papastavrou, G.; Borkovec, M. *Phys. Rev. Lett.* **2010**, *104*, 228301.
- [161] Popa, I.; Papastavrou, G.; Borkovec, M. *Phys. Chem. Chem. Phys.* **2010**, *12*, 4863–4871.
- [162] Penfold, J.; Thomas, R. K. *Phys. Chem. Chem. Phys.* **2013**, *15*, 7017–7027.
- [163] Simister, E. A.; Thomas, R. K.; Penfold, J. *J. Phys. Chem.* **1992**, *96*, 1373–1382.
- [164] Taylor, D. J. F.; Thomas, R. K.; Penfold, J. *Langmuir* **2002**, *18*, 4748–4757.
- [165] Schelero, N.; Hedicke, G.; Linse, P.; v. Klitzing, R. *J. Phys. Chem. B* **2010**, *114*, 15523–15529.
- [166] Qu, D.; Brotons, G.; Bosio, V.; Fery, A.; Salditt, T.; Langevin, D.; von Klitzing, R. *Colloids Surface A* **2007**, *303*, 97–109.
- [167] Boris, D. C.; Colby, R. H. *Macromolecules* **1998**, *31*, 5746–5755.
- [168] Colby, R. H. *Rheol. Acta.* **2010**, *49*, 425–442.
- [169] Israelachvili, J. N. *Intermolecular and Surface Forces*, 3rd ed.; 2011.
- [170] Maeda, H.; Maeda, Y. *Langmuir* **2015**, *31*, 7251–7263.
- [171] Terech, P.; Chazeau, L.; Cavaille, J. Y. *Macromolecules* **1999**, *32*, 1872–1875.

- [172] Su, Y.; Burger, C.; Hsiao, B. S.; Chu, B. *J. Appl. Crystallogr.* **2014**, *47*, 788–798.
- [173] Cherhal, F.; Cathala, B.; Capron, I. *Nord. Pulp. Pap. Res. J.* **2015**, *30*, 126–131.
- [174] Fall, A. B.; Lindström, S. B.; Sundman, O.; Ödberg, L.; Wågberg, L. *Langmuir* **2011**, *27*, 11332–11338.
- [175] Porod, G. *Acta Physica Austriaca* **1948**, *2*, 255–292.
- [176] Guinier, A. *X-ray Diffraction in Crystals, Imperfect Crystals, and Amorphous Bodies*; 1963; p 378.
- [177] Bonini, C.; Heux, L.; Cavaillé, J.; Lindner, P. *Langmuir* **2002**, *18*, 3311–3314.
- [178] Schütz, C.; Agthe, M.; Fall, A. B.; Gordeyeva, K.; Guccini, V.; Salajková, M.; Plivelic, T. S.; Lagerwall, J. P. F.; Salazar-Alvarez, G.; Bergström, L. *Langmuir* **2015**, *31*, 6507–6513.
- [179] Usov, I.; Mezzenga, R. *Macromolecules* **2015**, *48*, 1269–1280.
- [180] Wilson, D. L.; Kump, K. S.; Eppell, S. J.; Marchant, R. E. *Langmuir* **1995**, *11*, 265–272.
- [181] Ren, S.; Sun, X.; Lei, T.; Wu, Q. *Journal of Nanomaterials* **2014**, *2014*, ID 582913.
- [182] Yu, H. Y.; Qin, Z. Y.; Liu, L.; Yang, X. G.; Zhou, Y.; Yao, J. M. *Compos. Sci. Technol.* **2013**, *87*, 22–28.
- [183] Sun, X.; Wu, Q.; Ren, S.; Lei, T. *Cellulose* **2015**, *22*, 1123–1133.
- [184] Jonoobi, M.; Oladi, R.; Davoudpour, Y.; Oksman, K.; Dufresne, A.; Hamzeh, Y.; Davoodi, R. *Cellulose* **2015**, *22*, 935–969.
- [185] Jarvis, M. *Nature* **2003**, *426*, 611–612.
- [186] Li, Q.; Renneckar, S. *Biomacromolecules* **2011**, *12*, 650–659.
- [187] Wågberg, L.; Decher, G.; Norgren, M.; Lindström, T.; Ankerfors, M.; Axnäs, K. *Langmuir* **2008**, *24*, 784–795.
- [188] Fall, A. B.; Lindström, S. B.; Sprakel, J.; Wågberg, L. *Soft Matter* **2013**, *9*, 1852–1863.
- [189] Derjaguin, B.; Landau, L. *Acta Physicochim. URSS* **1941**, *14*, 633–662.
- [190] Verwey, E. J. W.; Overbeek, J. T. G. *Theory of the Stability of Lyophobic Colloids*; Elsevier Publishing Co., 1948.
- [191] Odijk, T. *Macromolecules* **1986**, *19*, 2313–2329.
- [192] Castelletto, V.; Itri, R.; Amaral, L. Q.; Spada, G. P. *Macromolecules* **1995**, *28*, 8395–8400.

-
- [193] Qiu, X.; Kwok, L.; Park, H.; Lamb, J.; Andresen, K.; Pollack, L. *Phys. Rev. Lett.* **2006**, *96*, 1–4.
- [194] Pollack, L. *Ann. Rev. Biophys.* **2011**, *40*, 225–242.
- [195] Zhang, G.; He, F.; Zou, X.; Gong, J.; Zhang, H. *J. Phys. Chem. Solids* **2008**, *69*, 1471–1474.
- [196] Yamaguchi, D.; Miyamoto, N.; Fujita, T.; Nakato, T.; Koizumi, S.; Ohta, N.; Yagi, N.; Hashimoto, T. *Phys. Rev. E* **2012**, *85*, 011403.
- [197] Dhar, N.; Au, D.; Berry, R.; Tam, K. *Colloids Surface A* **2012**, *415*, 310–319.
- [198] Brinatti, C.; Huang, J.; Berry, R. M.; Tam, M. K.; Loh, W. *Langmuir* **2016**, *32*, 689–698.